
POLITECNICO DI MILANO
Facoltà di Ingegneria Civile, Ambientale e Territoriale
Corso di Laurea Magistrale in Ingegneria Civile



CONCRETE MODELING IN HOT CONDITIONS:
CRACKING BEHAVIOR AND MATERIAL STIFFNESS DECAY

SUPERVISORS:

PROF. ROBERTO FELICETTI
DR. FRANCESCO LO MONTE

CANDIDATE: XUEJING WANG
STUDENT NUMBER: 816694

July 27th, 2016

Outlines

Concrete Modeling in Hot Conditions:.....	0
Cracking Behavior and Material Stiffness Decay.....	0
Outlines.....	1
List of figures.....	5
Abstract.....	12
Sommario.....	13
Acknowledgement.....	14
1. Introduction.....	15
1.1 Fire Engineering.....	15
1.2 Source and Mechanism of Fire.....	18
1.2.1 Source of Fire.....	18
1.2.2 Mechanism of Fire.....	18
1.3 Fire Scenario.....	19
1.3.1 Buildings.....	20
1.3.2 Offshore Structures and Petrochemical Plants.....	20
1.3.3 Tunnels.....	21
1.3.4 Bridges.....	23
1.3.5 Nuclear Power Plants.....	24
2. Concrete Behavior at High Temperature.....	26
2.1 Temperature Effects on the Chemical Composition.....	27
2.2 Porosity.....	29
2.3 Density.....	31
2.4 Vapor Diffusivity.....	32
2.5 Thermal Properties.....	33
2.5.1 Thermal Conductivity.....	33
2.5.2 Thermal Diffusivity.....	35
2.5.3 Specific Heat.....	36

2.5.4 Thermal Expansion	37
2.6 Mechanical Properties	40
2.6.1 Compressive Strength	42
2.6.2 Tensile Strength	44
2.6.3 Poisson Ratio	46
2.6.4 Elastic modulus.....	47
2.6.5 Fracture Energy.....	49
2.7 High-Performance Concrete	49
3. Concrete Spalling at High Temperature.....	52
3.1 Factors Influence Spalling	53
3.2 Pore Pressure Spalling	55
3.3 Thermal Stress Spalling	56
3.4 Thermal Cracking Spalling.....	56
4. Thermal Problem	58
4.1 Heat Transfer Mechanisms	58
4.1.1 Conduction.....	58
4.1.2 Convection.....	62
4.1.3 Radiation.....	63
4.2 General Numerical Modelling	63
4.2.1 General Equations according to Fourier Law	63
4.2.2 Initial and Boundary Conditions in Fire Design.....	64
5. Benchmark in Crack Behavior Study	66
5.1 Numerical Simulation in Commercial Software.....	66
5.2 Heat transfer analysis in ABAQUS	67
5.2.1 Geometry	67
5.2.2 Thermal Effects.....	68
5.2.3 Thermal Profile	69
5.3 Mechanical Analysis in ABAQUS.....	70
5.3.1 Mechanical Properties	71

5.3.2 Boundary Conditions	78
5.3.3 Mesh and Element	80
5.4 Benchmark result	80
6. An algorithm for Cracking Behavior Study	83
6.1 Algorithm Principle	83
6.2 Software Developed by MATLAB	85
6.2.1 Data resource	85
6.2.2 Functions.....	86
6.2.3 Main script: Software-A	87
6.3 Result and Comparison.....	88
6.3.1 Compressive Condition	88
6.3.2 Tensile Condition.....	89
7. A Discussion of Fracture Energy Implementation	95
7.1 Fracture Energy.....	95
7.2 Cracking Criterion Implementation	97
7.2.1 Displacement Implementation	97
7.2.2 Fracture Energy Implementation in MATLAB.....	98
7.2.3 Characteristic Length.....	99
7.3 Result and Conclusion	101
7.3.1 Result	101
7.3.2 Conclusions.....	104
8. Material Stiffness Decay.....	106
8.1 Algorithm Principle	106
8.1.1 Theoretical fundamental	106
8.1.2 Least square method	109
8.2 Function Development and Modification	110
8.2.1 Functions.....	110
8.2.2 Accuracy of the function.....	112
8.3 Software Development	116

8.3.1 Normalized Distance η_G	116
8.3.2 Algorithm Sensitivity.....	119
8.4 Software Improvement	120
8.4.1 Algorithm modification.....	120
8.4.2 Software Modification	121
8.5 Experimental Data Implementation	121
8.5.1 Experimental Data	121
8.5.2 Evaluation of Stiffness Decay.....	124
9. Conclusion	127
Reference	130

List of figures

Fig.2. 1 Microstructure of concrete (A ƒcin and Neville, 1993)	28
Fig.2. 2: Concrete thermometer (after Khoury, 2000).	28
Fig.2. 3: Concrete pore size distribution at different temperatures (after Noumowe, 1995).	29
Fig.2. 4: Plots of weight loss (a) and total porosity (b) in concrete (Noumowe, 1995).	29
Fig.2. 5: (a) The total porosity at different temperatures (Gawin et al., 1999); and (b) Portland cement paste porosity as a function of the temperature (Harmathy, 1970).	30
Fig.2. 6 (a) True density, Bulk density and porosity of cement paste versus temperature; and (b) density of concretes with different coarse aggregates (Harmathy, 1970).	32
Fig.2. 7 Vapor diffusivity in dry air as a function of temperature and pressure, according to Equation(2.3), $x = p_{g0} / p_g$	32
Fig.2. 8 (a) Thermal conductivity of initially-saturated concrete according to Blundell et al. (1976), and (b) of different types of concrete according to Harmathy and Allen (1973), as a function of the temperature.	33
Fig.2. 9 (a) Thermal conductivity as a function of the density and moisture content; and (b) thermal conductivity as a function of the temperature, (Shin et al., 2002).	34
Fig.2. 10 Specific heat of various concretes according to (a) Bazant and Kaplan (1996), and of (b) a Korean nuclear power plant concrete (Shin et al., 2002). .	35
Fig.2. 11 Thermal diffusivity of limestone (a) and siliceous (b) concretes (Schneider, 1982).	36
Fig.2. 12 Thermal diffusivity of normal and lightweight concretes, as a function of the temperature (Harmathy and Allen, 1973).	36
Fig.2. 13 The specific heat (a) of various concretes according to Bazant and	

Kaplan (1996), and (b) of a Korean nuclear power plant concrete (Shin et al., 2002).....	37
Fig.2. 14 The thermal strain (a) of Portland cement paste and(b) of different aggregates, as a function of the temperature (Bazant and Kaplan, 1996).....	38
Fig.2. 15(a)Portland cement, mortar, and concrete according to Cruz and Gillen (1980), and (b) Portland cement concretes subjected to different load levels according to Sullivan et al. (1982), as a function of the temperature.	39
Fig.2. 16LITS - of concrete during heating under compressive loads (Khoury, 2000).	41
Fig.2. 17Temperature effect on the stress-strain curves of concrete.....	43
Fig.2. 18Residual compressive strength as a function of temperature according to (a) EN1994-1-2 (2004) and (b) ACI 216-1.07 (2007).....	43
Fig.2. 19The residual compressive strength oftwo HPC and two UHPC: (a) actual value; (b) values normalized with respect to the virgin strength (Khoury, 2000).	44
Fig.2. 20(a) The normalized tensile strength according to EN1992-1-2 (2004) in hot conditions, and(b) of High-Strength Concrete and Normal-Strength Concrete in residual conditions (Noumowe et al., 1996), as a function of the temperature.	45
Fig.2. 21Direct tension tests on notched cylinders: (a) plots of the residual strength; and (b) plots of two strength ratios (f_c/f_t = compressive-to-tensile strength ratio; f_t^*/f_t = indirect-to-direct strength ratio; indirect strength = 3-point bending; Felicetti and Gambarova, 1998).	45
Fig.2. 22(a) The normalized stress as a function of the Poisson ratio, for different temperatures (Ehm, 1985); and (b) the Poisson ratio as a function of the temperature (Marechal, 1972).....	47
Fig.2. 23Effect of aggregate type and concrete strength on Poisson ratio (Cruz, 1966).	47
Fig.2. 24The normalized concrete elastic modulus for(a) different aggregate types according to <i>fib</i> (2007), and for(b) different sealing conditions according to	

Nanstad (1976), as a function of the temperature.....	48
Fig.2. 25 Normalized fracture energy G_f as a function of temperature (Heinfling, 1998).....	49
Fig.3. 1 Explosive spalling: an empirical envelope for Normal-Strength Concrete, showing the influence of moisture content and applied stress (Khoury, 2000). 52	
Fig.3. 2 Profile of temperature, pore pressure and moisture content in Normal-Strength and High-Performance Concrete wall exposed to fire (after Khoury, 2000).	54
Fig.3. 3 The process for the build-up of pressure in a concrete wall exposed to fire (after Zeiml et al., 2006).	55
Fig.3. 4 Concrete spalling mechanisms in a heat-exposed wall: qualitative diagrams of (a) the temperature T and of the normalized tensile strength f_{ct}^T / f_{ct}^{20} (b,c), of (b) the thermal stress σ and normalized compressive strength f_c^T / f_c^{20} , and of (c) pore pressure p for two different values of fire durations, $t_2 > t_1$	56
Fig.4. 1 Heat transfer inside a plate made by homogeneous and isotropic material... 59	
Fig.4. 2 Density variation according to EN 1992-1-2:2004 (E).	60
Fig.4. 3 Specific heat c_p , as a function of temperature at 3 different moisture contents u , of 0, 1,5 and 3 % by weight for siliceous concrete, EN 1992-1-2:2004 (E).....	61
Fig.4. 4 Thermal conductivity of concrete according to EN 1992-1-2:2004 (E).....	62
Fig.5. 1 Geometry of the beam studied by numerical simulation.....	67
Fig.5. 2 Geometry studied by numerical modelling	67
Fig.5. 3 Surface film condition in ABAQUS.....	68
Fig.5. 4 Element type for simulation in ABAQUS	69
Fig.5. 5 Temperature distribution at the end of heating (7200s) in ABAQUS	69
Fig.5. 6 Sample section for temperature distribution profile.....	70
Fig.5. 7 Plot of temperature distribution profile as a function of time	70

Fig.5. 8	Mathematical model for stress-strain relationships of concrete under compression at elevated temperatures	71
Fig.5. 9	Coefficient $k_{c,t}(T)$ allowing for decrease of tensile strength ($f_{ck,t}$) of concrete at elevated temperatures, EN 1992-1-2:2004	74
Fig.5. 10	Total thermal elongation of concrete at elevated temperatures, EN 1992-1-2:2004.....	74
Fig.5. 11	Parameters of Concrete damage plasticity.....	76
Fig.5. 12	Basic value of G_{F0}	77
Fig.5. 13	Fracture Energy G_F	77
Fig.5. 14	Tensile Behavior determined by fracture energy in ABAQUS	78
Fig.5. 15	Boundary condition to confirm translation.....	78
Fig.5. 16	Boundary condition to confirm symmetricity	79
Fig.5. 17	External load.....	79
Fig.5. 18	Constraint in left boundary	79
Fig.5. 19	Predefined field	80
Fig.5. 20	Element type in mechanical performing.....	80
Fig.5. 21	Stress distribution along the thickness of the specimen at different time point, respectively, when external load is 10MPa.....	81
Fig.5. 22	Stress distribution along the thickness of the specimen at different time point, respectively, when external load is 5MPa.....	81
Fig.5. 23	Stress distribution along the thickness of the specimen at different time point, respectively, when external load is 0.5MPa.....	81
Fig.5. 24	Comparison of displacement distribution as function of time with different external loads, respectively.....	82
Fig.6. 1	Section and increment of the specimen	83
Fig.6. 2	Constitutive law of concrete.....	86
Fig.6. 3	Constitutive law for compression.....	87
Fig.6. 4	Constitutive law for tension.....	87

Fig.6. 5 Stress distribution comparison between two methods along the thickness during 120min, with external load equal to 10MPA.....	88
Fig.6. 6Elastic modulus distribution along the thickness during 120min, with external load equal to 10MPA.....	89
Fig.6. 7 Displacement development during a fire for an external load of 10MPA. ...	89
Fig.6. 8 Stress distribution along the thickness during 120min, with external load equal to 5MPA. Analysis via Matlab – Software A	90
Fig.6. 9 Elastic modulus distribution along the thickness during 120min, with external load equal to 5MPA.....	90
Fig.6. 10 Stress distribution comparison along the thickness during 120min, with external load equal to 5MPA.....	91
Fig.6. 11 Displacement development according to ABAQUS and MATLAB for the external load of 5MPA.	92
Fig.6. 12 Stress distribution along the thickness during 120min, with external load equals to 0.5MPA,.....	92
Fig.6. 13 Stress distribution comparison between two methods along the thickness during 120min, with external load equal to 0.5MPA.....	93
Fig.6. 14 Elastic modulus distribution along the thickness during 120min, with external load equal to 0.5MPA.....	94
Fig.6. 15 Displacement development according to ABAQUS and MATLAB for the external load of 0.5MPA.	94
Fig.7. 1“Tension stiffening” model, ABAQUS User guide, vol. 3.	96
Fig.7. 2Fracture energy cracking model, ABAQUS User guide, vol. 3.	96
Fig.7. 3 Displacement implementation.	97
Fig.7. 4 Cracklings after 2 hours performance and selected Section-1.	98
Fig.7. 5 Constitutive law in tensile branch (MATLAB)	99
Fig.7. 6Displacement controlled tensile behavior (Case 1)	99
Fig.7. 7Fracture Energy Cracking Criterion (Case 2).....	100

Fig.7. 8Fracture Energy Cracking Criterion (Case 3).....	100
Fig.7. 9 Stress distribution with mesh size equals to 25x25mm (Case 4)	101
Fig.7. 10Fracture Energy Cracking Criterion (Case 4).....	101
Fig.7. 11 Stress distribution along the thickness during 120min, with external load equal to 0.5MPa and mesh size equal to 5mm.	102
Fig.7. 12 Secant modulus distribution along the thickness during 120min, with external load equal to 0.5MPa and mesh size equal to 5mm.	102
Fig.7. 13 Displacement histogram of ABAQUS (mesh size 5mm) results and MATLAB results (characteristic length 50mm and 5mm), when external load equal to 0.5MPa.	102
Fig.7. 14 Section 2-crack section.....	103
Fig.7. 15 Section 3-un-crack section	103
Fig.7. 16 Stress distribution: ABAQUS result section 1, average of section 2 and section 3, and MATLAB, along thickness (120min), external load (0.5MPa).	104
Fig.8. 1 Geometry for studied model.....	107
Fig.8. 2 Flow chart of the software.....	112
Fig.8. 3 Stress distribution comparison, elastic modulus implement by linear interpolation and 3 order polynomial, (external load=10mpa).....	113
Fig.8. 4 Stress distribution comparison, elastic modulus implement by linear interpolation and 3 order polynomial, (external load=5mpa).....	114
Fig.8. 5 Stress distribution comparison, elastic modulus implement by linear interpolation and 3 order polynomial, (external load=0.5mpa).....	115
Fig.8. 6 Displacement comparison, (elastic modulus implement by linear interpolation and 3 order polynomial), among external load equal to 10MPa, 5MPa, 0.5MPa, respectively.....	116
Fig.8. 7 Flow chart for assumption of normalized distance and Software-B development.....	116

Fig.8. 8 Input modulus decay for Software A, as function of temperature (EC2 , 3 order polynomial interpolation).....	117
Fig.8. 9 Input modulus decay of Software A, and output modulus decay from Software B, as function of temperature.	118
Fig.8. 10 Input modulus decay of Software A (Random selected), as function of temperature in fire duration.	118
Fig.8. 11 Input modulus decay of Software A (Random selected), and output modulus decay from Software B, as function of temperature.	119
Fig.8. 12 Input modulus decay of Software A (implement by tabular data with intermediate value interpolated by linear interpolation), and output modulus decay of Software-B, as function of temperature.	119
Fig.8. 13 Specimen investigated in experiment.....	122
Fig.8. 14 Locations of LVDTs and evaluation method.....	123
Fig.8. 15 Evaluated thermal profile according to experimental temperatures, regarding different thickness, for specimens Monofilament B, Fibrillate A, and Fibrillate B.....	123
Fig.8. 16 Experiment obtained specimen vertical displacement profile, for specimen Monofilament B, Fibrillate A, and Fibrillate B.	124
Fig.8. 17 Stiffness decay suggested by EC2, as a function of temperature.	124
Fig.8. 18 Modulus decay for 4 specimen evaluated by numerical simulation, as function of temperature.....	125
Fig.8. 19 Comparison of displacements obtained according to EC2 stiffness decay, software evaluated stiffness decay, and experiment results, as function of temperature, for different specimens.	126

Abstract

The usage of High-Performance Concrete (HPC) is gradually increasing in many structures exposed to extreme environmental conditions. One specific case is high temperature. Previous studies have made important achievements about the mechanical behavior of High-Performance Concrete (HPC) under high temperature on the basis of experiments. But so far little effort has been made on numerical simulation.

Two topics will be discussed in the present work: the concrete cracking behavior in hot conditions and the evaluation of material stiffness decay. To study the former topic, the commercial software ABAQUS is also used. The present work not only studies the aspects concerning cracking behavior by using commercial software (Abaqus), but also develops algorithms implemented in Matlab. With known experimental data and elastic modulus decay (EC2), the software evaluates concrete behavior under high temperature. The software results have good agreement with ABAQUS but consumes much less time.

Then a discussion about fracture energy cracking criterion will be carried out to study the implementation of constitutive law of concrete after cracking occurs.

Finally, for the latter topic, how to monitor or estimate the concrete stiffness decay during high temperature is addressed. The present work addresses the development of another software to evaluate the concrete stiffness decay with temperature. It is an inverse analysis starting from experimental data, expressed in terms of thermal profile and tested member flexural behavior during heating. In this way, consideration on concrete stiffness decay will be carried out. Several experimental data from different tests (content different concrete mixes) will be estimated by the software. Comparisons will be made among the different specimens to verify the reliability of the software.

Sommario

L'utilizzo di Calcestruzzo ad Alte Prestazioni (High-Performance Concrete - HPC) sta gradualmente aumentando in molte strutture esposte a condizioni ambientali estreme. Un caso specifico è l'alta temperatura. Studi precedenti hanno importanti risultati sul comportamento meccanico dell'HPC ad alta temperatura sulla base di prove sperimentali. Ma finora poco sforzo è stato fatto sulla simulazione numerica.

Due temi saranno discussi nel presente lavoro: il comportamento a fessurazione del calcestruzzo a caldo e la valutazione del decadimento della rigidità del materiale. Per studiare il primo aspetto, viene utilizzato anche il software commerciale ABAQUS. Il presente lavoro non solo studia gli aspetti relativi alla fessurazione utilizzando un software commerciale (Abaqus), ma riporta lo sviluppo di un algoritmo implementato in Matlab. Con dati sperimentali noti e il decadimento del modulo elastico (EC2), il software valuta il comportamento del calcestruzzo a temperatura elevata. I risultati del software hanno buon accordo con ABAQUS ma ad un costo computazionale nettamente più basso.

Una discussione sull'energia di frattura sarà effettuata per studiare l'implementazione della legge costitutiva del calcestruzzo dopo il verificarsi di fessurazione.

Infine, per il secondo argomento, viene trattato il monitoraggio del decadimento del modulo elastico del calcestruzzo ad alta temperatura. Il presente lavoro riguarda lo sviluppo di un altro software per valutare il decadimento di rigidità del calcestruzzo con la temperatura. Si tratta di un'analisi inversa partendo da dati sperimentali, espressa in termini di profili termici e comportamento flessionale durante il riscaldamento. Diversi dati sperimentali provenienti da diversi test (differenti miscele di calcestruzzo) saranno stimati dal software. I confronti saranno effettuati tra i diversi campioni per verificare l'affidabilità del software.

Acknowledgement

The authors sincerely appreciate the help from Prof. Roberto FELICETTI, and the co-supervisor Dr. Francesco LO MONTE. The valuable guidance, suggestions, as well as kindly encouragements they provided helped much in completing the present thesis during the whole process.

Thanks and love to the families and friends for understanding and supporting at any time.

1. Introduction

1.1 Fire Engineering

Ten thousand years ago, one lucky guy who once succeeded in starting a fire with stone and wood did not know that he brought one of the most powerful and important element into his race history by the occasion. It should not exist any doubt that fire is a symbol of evolution.

Nowadays, fire has dual implications to structure. It is an essential resource for engineering material acquisition. Yet, the primary character of fire should be an external load in extreme condition. However, this load always occurs with destructive effects which usually leads to severe damage or even collapse. Respect to this consequence, the necessity of Fire Engineering can be understood, while Fire Engineering usually aims at two levels of safe structure design:

- a. to avoid the activation of a fire or to prevent flames spreading outside the compartment to other parts of the building;
- b. to design structures that can face the fire event for a sufficient time-length.

The first level aim can be achieved by implement active or passive devices, such as sprinklers, fans, into the structures. To achieve the second level is to allow people to leave the compartment in the fire.

A typical development of fire is split into four steps: Incipient, Growth, Burning, and Decay. The time-temperature curve is for a typical fire evolution given in Fig. 1. 1. It assumed that the fire happened inside a room which is without devices to stop the fire spreading.

The critical parameter involved in the abovementioned strategies is time. The Incipient period is the time interval before combustion, and the maximum predictable heating depends on potential fuel. Ignition is the starting point of flaming combustion. During the Growth period, fire spreads. At the start of this phase, the burning rate starts slowly and grows rapidly and is generally controlled by the nature of the fuel. Once if upper layer temperatures reach a certain value (600°C), the burning rate increases rapidly

yielding to *flashover* which represents the transition between Growth and Burning period. Then, usually the full room would be considered involved and the fire should be the fully developed fire. While the rate of burning is usually governed by the available ventilation. So far, if the fire is left to burn it will develop into Decay period, the fuel burns out, temperatures drop while the rate of burning becomes a function of the fuel.

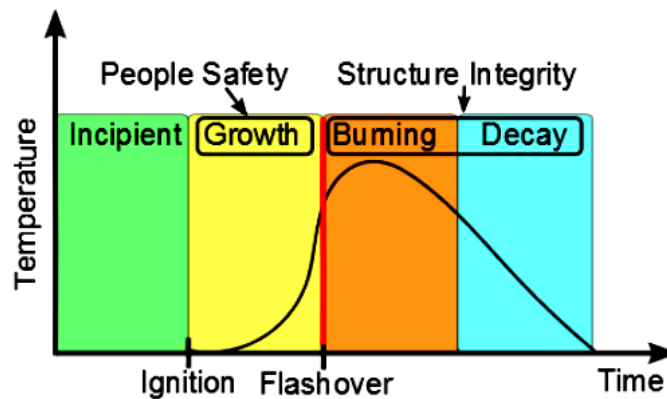


Fig.1. 1Typical time-temperature curve in the fire development

Base on the abovementioned separation, the flashover is also known as the threshold of the full development of a fire. Because of the associated high temperatures, the post-flashover phase only is taken into account from the structural point of view. It is necessary and mandatory to take enough measures when designing structures so as to provide sufficient time for people to escape towards safe places. Time is closely related to the type of material used in the structure (steel, timber or concrete).

In this work the performance of concrete structures will be studied and the study will focus on the concrete behavior during a fire. It is proper to point out that high attention will be paid to the High-Performance Concrete (HPC), which is gradually replacing the role of ordinary concrete in the important structures, such as tunnels, marine platforms, Liquefied Natural Gas terminals, containment shells for industrial facilities, etc. who usually have high exposure to extreme environmental conditions. Also, when this kind of structures is required for repair or strength according to the current code, HPC would be preferred than ordinary concrete. As a matter of fact, the widespread usage of HPC among extreme condition brings in new phenomena and those who are beyond the current knowledge of the behavior of ordinary ones will become new problems. One example of these new induced unknowns is recognized: High-Performance Concrete is particularly sensitive to the

phenomenon of spalling under certain thermal and mechanical conditions.



Fig.1. 2Spalling-damaged heat-exposed columns (Pentagon, Washington, USA, 2001).

Once a progressive spalling occurs, it involves the gradual fall out of small pieces of concrete from the surface of the structural members, or sudden failure with a large release of energy and flake of large pieces. Obviously, this phenomenon will reduce the capacity of the structure. And if you imagine the worst condition, the complete failure of members or even the whole structure can be expected. A severe scenario is shown in Fig.1. 2, which shows some columns' behavior after the fire. This is the reason that spalling should be taken into account while considering fire resistance of the structure. Frankly, spalling could be considered as a complicated function of a series of different factors, including temperature, moisture content, vapor pressure, cement paste, etc. It would be difficult but interesting to have a full understanding of the mechanism behind spalling and to quantify the risk of the occasion.

One of the most commonly-used and most economical methods to reduce or even prevent spalling is adding polypropylene fibers to the concrete mix within a range of 1-2% by mass (Buchanan, 2001). During fire exposure, polypropylene fibers increase concrete porosity by creating cavities and micro-fractures due to their expansion and melting. This further porosity will provide channels so that water vapor can escape easily, so the vapor pressure will decrease, so will the risk of spalling. Generalizing all the above, with these new materials, a new approach is required in building design.

Technical solutions should focus on a number of parameters, such as the type of concrete, external protection, member dimensions, the microstructure of the materials, the

aggregate type, the cement paste, etc.

1.2 Source and Mechanism of Fire

1.2.1 Source of Fire

Ignition occurs when a combustible mixture of fuel and gasses is heated to the temperature which is able to trigger the reactions of exothermic oxidation (so-called combustion). Ignition generally requires heat to be provided by an external source and a few are the possible heat sources that cause fire ignition:

- a.** Sources with flame (matches, candles, gas heaters, open fires);
- b.** Smoldering sources (cigarettes);
- c.** Electrical sources (overheating);
- d.** Radiant sources (sunlight, hot items, heaters).

There are also other less common sources related to hot surfaces, mechanical factors (friction), natural events (lightning), transportation (car, bus and train accidents), crime (arson) and socio-political issues (terrorism, war). With these sources fire can take place in the building and spread from the first burning object to a second object by flame contact - if it is very close - or by radiant heat transfer - if it is further away. To ignition, a second object depends on the intensity of the radiation from the flame and the distance between the objects. The amount of heat and the temperature required to cause ignition depend on the material properties of the fuel, on the size and shape of the ignited object, and on the time of heat exposure.

1.2.2 Mechanism of Fire

An effective ignition source is the one that has sufficient heat and temperature to cause ignition in the expected time of exposure. The time to ignition of the materials depends on the thermophysical properties (density, thermal conductivity, and specific heat). The thermal inertia is defined from these thermos-physical properties. When exposed to the same heat source, the surface of a material with higher thermal inertia will heat more slowly than the lower ones, so it will lead to slower ignition. The understanding of the evolution of a fire

requires the knowledge of the phenomena and the govern laws of the transmission of heat, which occurs by conduction, convection, and radiation.

Conduction is a key factor in the ignition of solid surfaces and in the fire resistance of barriers and structural members.

Convection is the heat transfer which is induced by the movement of fluids, either gasses or liquids. It is an important aspect in flame spreading and in the upward transport of smoke and hot gasses to the ceiling or through the window from a room fire. Usually, convective heat-transfer calculations content heat transfer between the surface of a solid and a surrounding fluid which heats or cools the solid material. The rate of heating or cooling depends on several factors, such as the velocity of the fluid at the surface.

Radiation is the energy transfer by means of electromagnetic waves. This should be the main mechanism for heat transfer from flames to fuel surfaces, from hot smoke to building objects and from a burning building to the adjacent one. Its extreme importance in fires should be recognized.

1.3 Fire Scenario

For one structural system, especially when it is not built for critical use, fire can be one of the most severe conditions during its service life. Here listed main structures that may subject to fire:

- a.** buildings for residential, office or other kind daily usage;
- b.** offshore structures and petrochemical plants;
- c.** tunnels;
- d.** bridges and viaducts;
- e.** nuclear power plants.

The fire load is generally applied to a structure by means of standard *temperature-time curves* of the hot gasses which will be suggested by Code provisions. The curves are defined considering a number of parameters, while the source of combustion plays a major role among the parameters.

1.3.1 Buildings

The Standard Fire Curve represents the development of the temperature for a cellulosic fire. In a standard fire curve, the fuel source is usually composed of wood, paper, fabric, etc. This fire profile contains a slow temperature rise up to 1000 °C during a period of 120 minutes. It is representing a single-exposure condition to a fully developed fire and does not include cooling, which occurs in real conditions, where for temperature decreasing side, it considers that most of the combustible material has been consumed.

Real fires can have a slower or longer growth phase, and, though rarely, once they are fully developed, temperatures can be higher than those of the Standard Fire

One of the most known expressions for the Standard Fire is that proposed by *EN 1991-1-2 (2004)*, the equation is given by Equation and the plotted in Fig. 1. 3:

$$T = 20 + 345 \log_{10}(8t + 1) \quad (1.1)$$

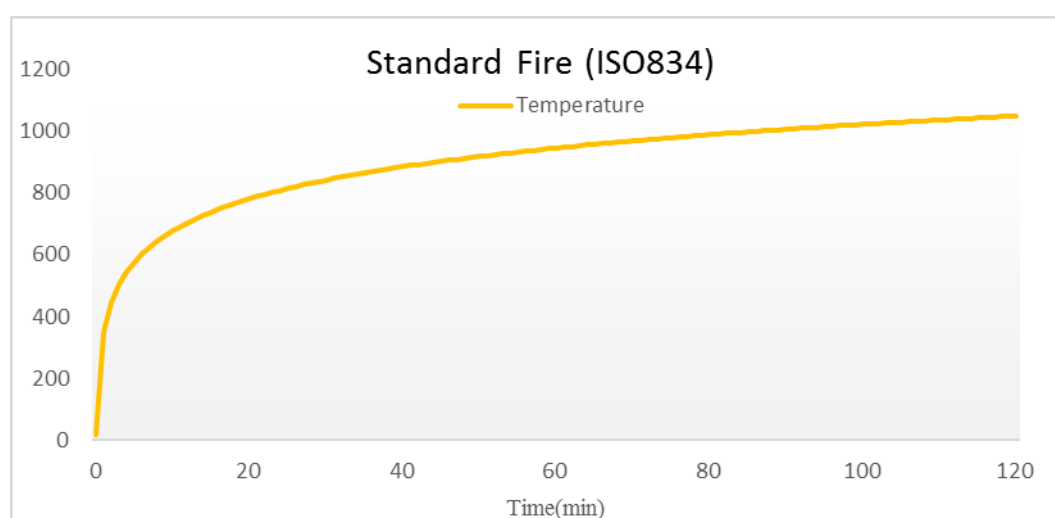


Fig.1. 3 Standard Fire.

1.3.2 Offshore Structures and Petrochemical Plants

In the 1970s, the oil company Mobil investigated Hydrocarbon Fire, which is induced due to the combustion of liquid fuels, and developed a temperature-time profile with a rapid temperature rise in the first 5 min of the fire up to 900 °C and a peak of 1100 °C. This research should be the foundation for test procedures to assess fire-protecting materials for the offshore and petrochemical plants. The Equation (1.2) and Fig. 1. 4 provide the equation and plot which represent the Curve ($T_0=20$ °C).

$$T = 1080(1 - 0.325e^{-0.167t} - 0.675e^{-2.5t}) + T_0 \quad (1.2)$$

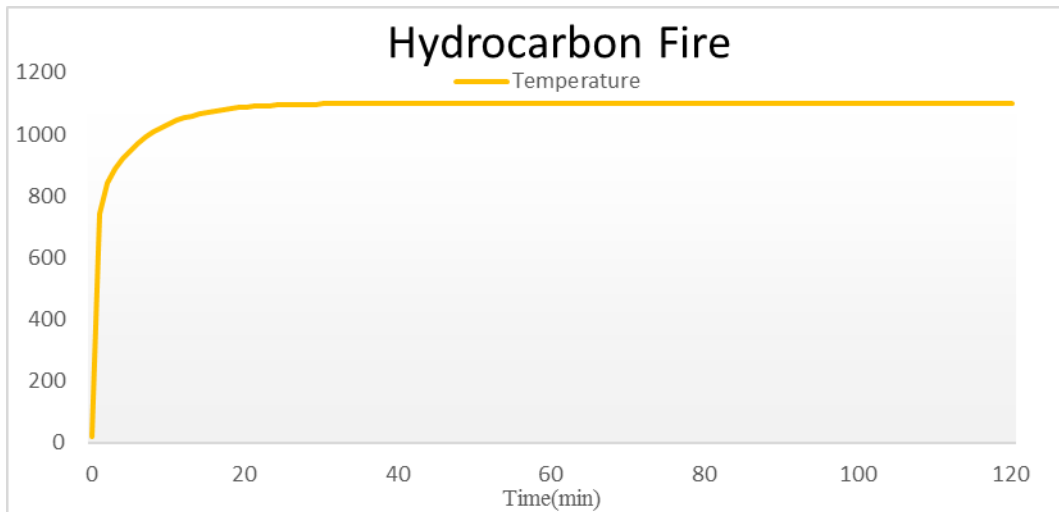


Fig.1. 4Hydrocarbon Fire

1.3.3 Tunnels

In modern life, tunnels play a significant role in transportation systems. For example, Italy, who is representing 12% of the population and 6% of the surface of the Continent, owns 30% of the railway tunnels, which means more than 1200 km. Meanwhile, it also owns 37% of the roadway tunnels, more than 600 km. Since over 75% of them were built before 1940, it indicates that during the constructing time the fire problems were under rated in the design of the structure. On the basis of the abovementioned data, assessing fire resistance of tunnels became a big issue in Italy. Several temperature-time curves have been developed and implemented in designing with the purpose of resolving this issue.

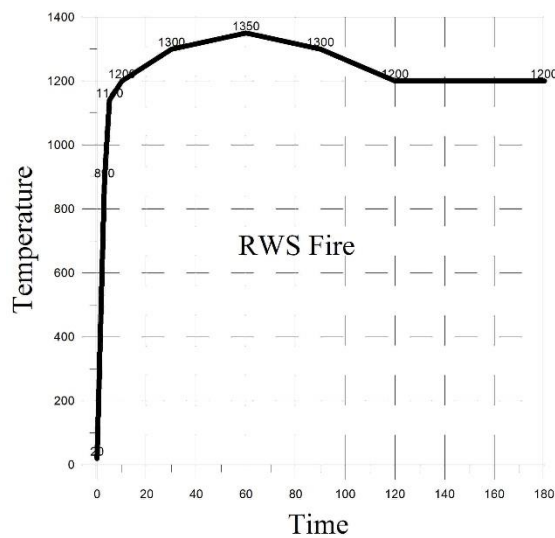


Fig.1. 5RWS Fire

Among all the alternative temperature profiles, the most commonly-adopted temperature-time curves in tunnel design are RWS and RABT Fire curves. In the Netherlands, the Ministry of Public Works (Rijswaterstaat - RWS), and the TNO Centre for Fire Research have established a fire curve for the evaluation of protecting materials in tunnels. This RWS Fire curve is a very severe hydrocarbon fire. After ignition, it will increase rapidly exceeding 1200 °C and arriving the peak at 1350 °C, which is the melting temperature of concrete, during the first 60 minutes, and then go falling gradually till 1200 °C at 120 min, which is the end time of the curve.

Fig.1. 5 shows the temperature-time curve of the RWS fire profile. RWS is intended to simulate railway tankers who carries petrol in tunnels with a fire load of 300 MW and will cause a fire of 2 hours, and is based on Dutch experience in tunnel fires.

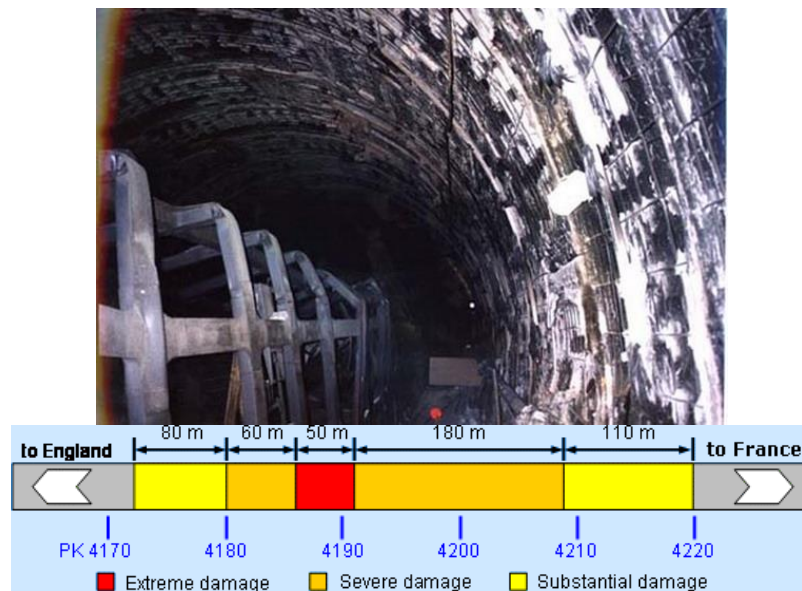


Fig.1. 6 Fires in Channel Tunnel

Yet, the maximum temperatures according to RWS is extremely high while according to recent research little major fires were able to attain its peak level. One case which happened in the English Channel (*Great Britain/France, November 1996* –Fig.1. 6) in the railway tunnel once reached the maximum temperature was 1100 °C, while another that got in the road tunnels of Mont Blanc (*Italy/France, April 1999* –Fig.1. 8) was 1000 °C.

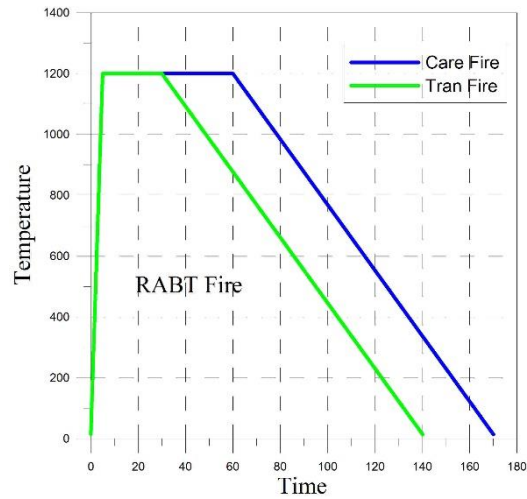


Fig.1. 7RABT Fire

The RABT German fire curve represents a less severe fire scenario in tunnels with respect to the RWS curve with a maximum temperature of 1200 °C, which is reached the melting point of some aggregates and will keep for 1 hour before fire decaying.

Fig.1.7 shows the profile of RABT Fire.

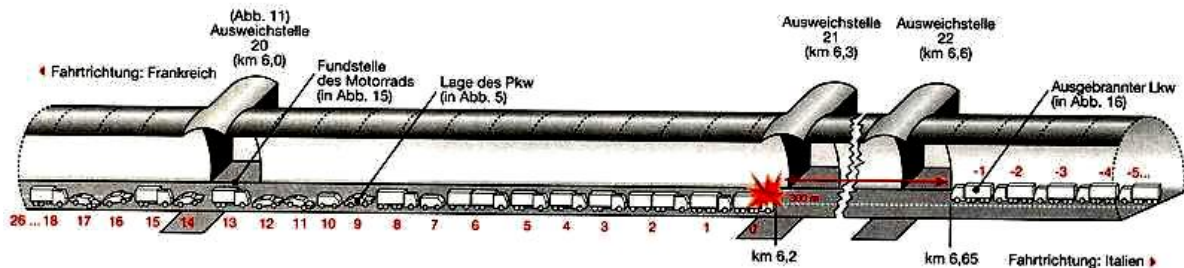


Fig.1. 8 Fire in the Mont Blanc Tunnel

1.3.4 Bridges

Comparably, fire in bridges is less likely to occur than the other condition which was

mentioned in above sections, yet there still existed a well-known example of bridge collapse due to fire. It was induced by a severe event (Fig.1. 9): the MacArthur Maze, a multilevel freeway interchange bridge which was located near Oakland and was serving several major cities in California, USA (April 2007). The fire was triggered by an accident that occurred early in the morning, involving a truck loaded with 32600 liters of gasoline. The fire finally reached the temperatures of 1650 °C, which is extremely high by any point of view. Then the resistance of the bridge was quite low, considering that a whole section of the overpass collapsed on the underneath interchange just 20 min after the beginning of the fire. The cause of the collapse could be blamed for the failure of the connections, whose steel structure was strongly weakened by the fire, overstressed by the significant deflection of the road section.



Fig.1. 9 McArthur Maze Collapse by Fire

1.3.5 Nuclear Power Plants

The containment structures of nuclear reactors are generally constituted by a double shell structure system: the inner one is usually made of pre-stressed concrete while the outer is made of reinforced concrete. The inner shell, which is mentioned as the primary shell, should guarantee the seal of gasses and liquids while the outer shell, which is the so-called secondary shell, should ensure the resistance for the impact of external objects. The high ductility of the material pledged the collaboration of the resistance for internal explosions.

The eventual fusion of the reactor would set both containers at elevated temperatures. It is, therefore, necessary to accurately study the behavior of concrete at high temperature

in order to understand if the material has adequate strength characteristics.

2. Concrete Behavior at High Temperature

The concept of *Fire Resistance* is related to the structural behavior but is not directly relevant to materials. Meanwhile, consider both during and after the fire, structural safety depends on the thermo-mechanical behavior of the materials. It has been already known for the good performance of concrete structures in hot conditions since it has its foundation on some positive aspects of cementations composites.

Firstly, concrete is incombustible and has good insulating properties since it has low thermal diffusivity. Moreover, the cement paste withstands endothermic chemical and physical processes during heating so that it can perform well in delaying heat transmission. In addition, during a fire, concrete could maintain its geometry, thus it would ensure the inner core of any given member to perform adequately.

Besides, there are still two critical issues that have to be taken into account. Firstly, the deterioration of the mechanical properties with the temperature due to the physic-chemical changes in the materials. Meanwhile, the explosive spalling, which results in loss of material, reduction in section size and possible direct exposure of the reinforcing steel to the flames.

Structural effects have to be taken into account in order to assess concrete elements and members' safety. The relatively low thermal diffusivity of concrete leads to high thermal gradients. When considering heat-exposed structural members, such thermal heterogeneity brings positive and negative effects. On the positive side, it maintains a low heat-affected core in the member. On the negative side, it brings in thermal dilation that is not uniform, in which condition that self-stresses will induce by restrained thermal dilation. Base on this acknowledgment, mechanical as well as thermal properties of the materials become fundamental in assessing the fire resistance. It is necessary to determine the temperature distribution in the cross section, which has the hot external layers that are exposed to the fire and cold layers inside. When the thermal field is known, the mechanical response can be evaluated point by point in the sections, and the structural fire resistance can be calculated.

2.1 Temperature Effects on the Chemical Composition

Concrete is a composite material. The material consists mineral aggregates, cement, and water in general. Among the compositions, cement and water together create the cement paste, which glues the aggregates and fills the voids (Fig.2. 1).

Concrete exposed to fire experiences chemical decomposition, depending on the temperature. The main chemical and physical processes taking place in concrete during heating are reported in Fig.2. 2(Khoury, 2000) and are described in the following:

(i) $100^{\circ}\text{C} \leq T \leq 200^{\circ}\text{C}$: free water starts to evaporate increasing the pressure inside the pores; dehydration of cement gel begins at around 180°C ;

(ii) $200^{\circ}\text{C} < T \leq 500^{\circ}\text{C}$: loss of water from gel pores, increasing dehydration rate and breakdown of tobermorite gel; above 450°C , portlandite $\text{Ca}(\text{OH})_2$ dissociates into calcium oxide (CaO) and water (H_2O);

(iii) $500^{\circ}\text{C} < T \leq 700^{\circ}\text{C}$: the rate of weight loss keeps increasing because of the decomposition of calcium hydroxide and of C-S-H (calcium silicate hydrate) phases; this is followed by the formation of β - C_2S (quartz silica) with larger volume per unit mass;

(iv) $700^{\circ}\text{C} < T \leq 900^{\circ}\text{C}$: calcination occurs (maximum rate at about 800°C);

(v) $T > 900^{\circ}\text{C}$: melting of cement paste and aggregates occurs at 1150°C and 1200°C with no further measurable weight loss; at 1270°C limestone-aggregate concrete consists mostly of white porous calcium oxide.

As regards the weight change as the temperature increases, the studies of Schneider, referring to concrete made with Portland cement, quartzite, basalt and limestone aggregates heated up to a temperature of 1300°C , showed the following results (Schneider, 1982):

(i) $20^{\circ}\text{C} \leq T \leq 100^{\circ}\text{C}$: weight loss caused by evaporation of water through the capillary pores;

(ii) $100^{\circ}\text{C} \leq T \leq 200^{\circ}\text{C}$: weight loss continues, with an increasing rate due to evaporation of water contained in the gel;

(iii) $200^{\circ}\text{C} < T \leq 500^{\circ}\text{C}$: weight loss proceeds but in smaller quantities, due to both the loss of pore water of the gel from the dehydration of first step and the breakage of bonds in

the tobermorite gel;

(iv) $500^{\circ}\text{C} < T \leq 700^{\circ}\text{C}$: weight loss increases again. At such temperatures it is due to both the decomposition of the calcium hydroxide in the cement paste and the decomposition of the C-S-H;

(v) $T > 900^{\circ}\text{C}$: when the melting of aggregates of basalt and quartzite is about to begin (1150-1200 $^{\circ}\text{C}$) there is no further loss of weight in the aggregate.

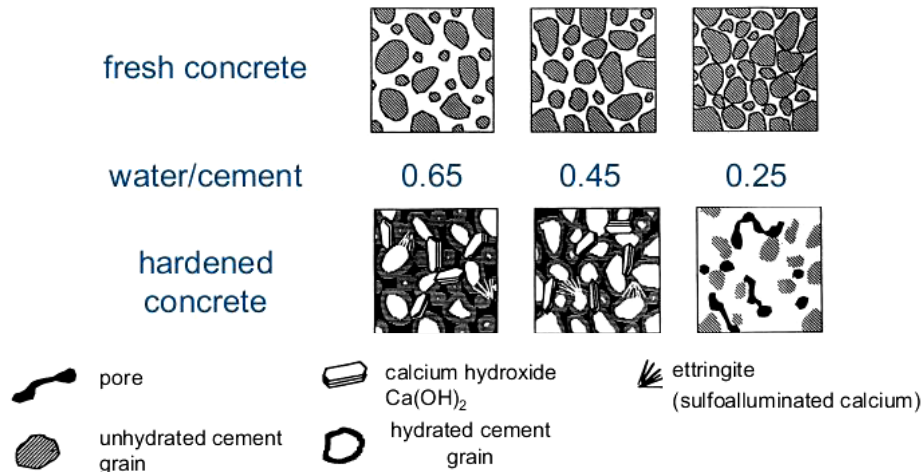


Fig.2. 1 Microstructure of concrete (Aïtcin and Neville, 1993)

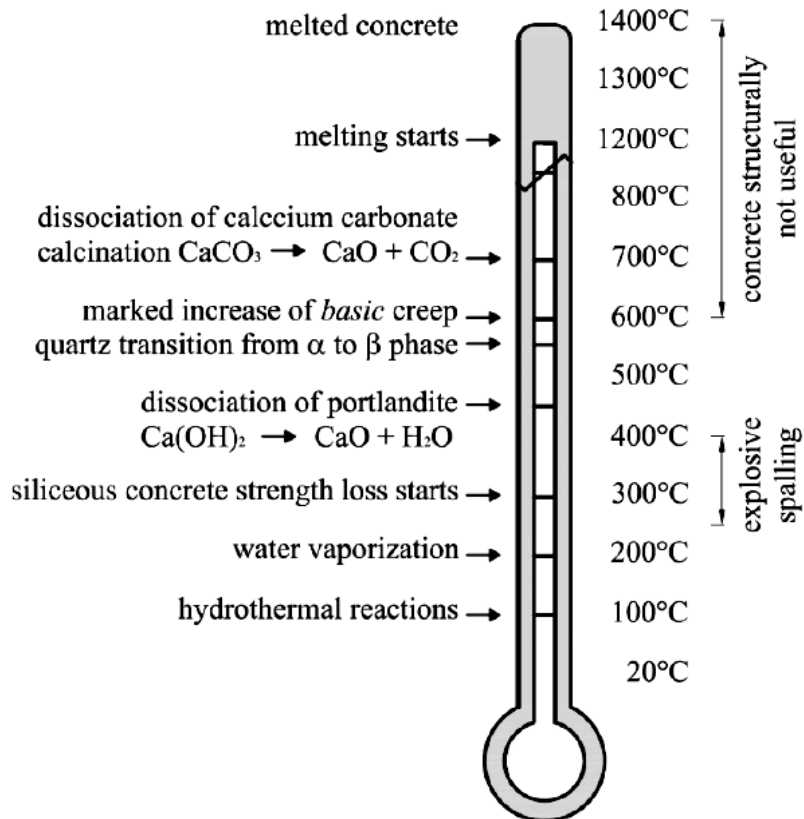


Fig.2. 2: Concrete thermometer (after Khoury, 2000).

2.2 Porosity

When it is exposed to high temperature, the pore structure, which refers to total porosity and pore size distribution, will be affected due to physical and chemical changes and it will induce loss of stability of concrete solid skeleton.

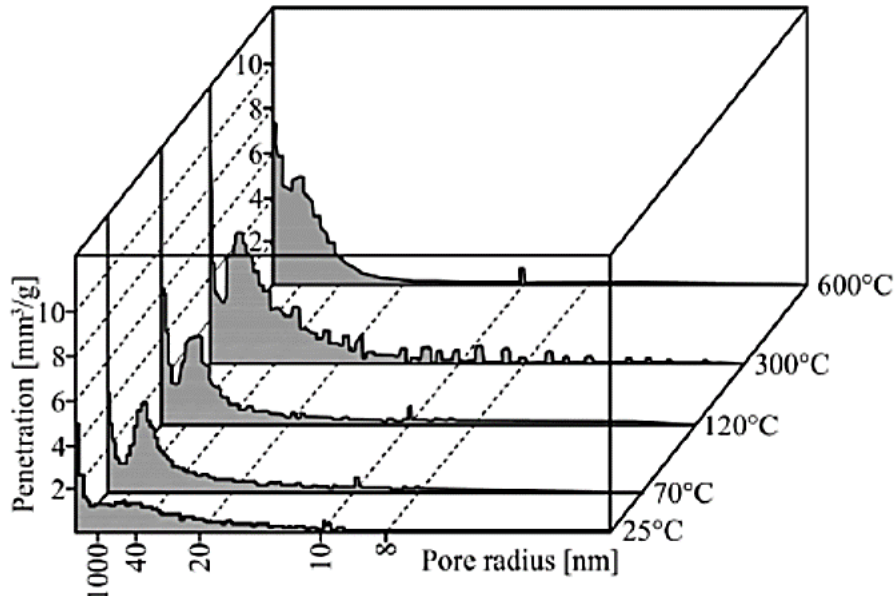


Fig.2. 3: Concrete pore size distribution at different temperatures (after Noumowe, 1995).

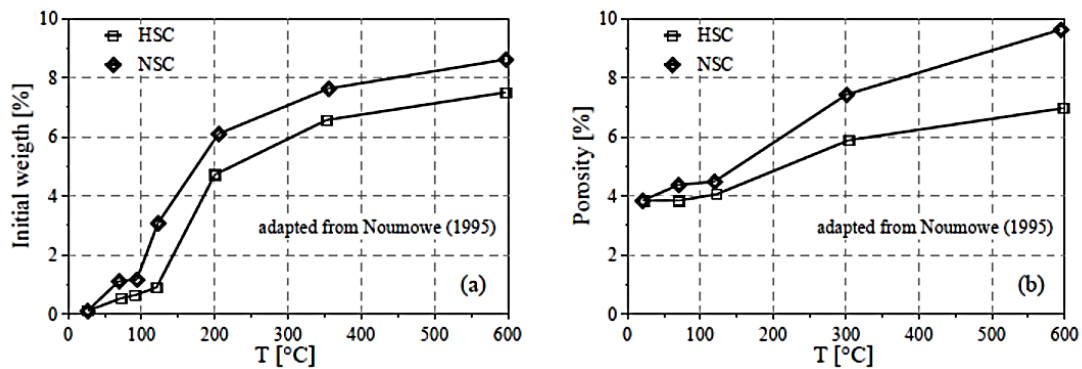


Fig.2. 4: Plots of weight loss (a) and total porosity (b) in concrete (Noumowe, 1995).

In Fig.2. 3 the pore size distribution of an ordinary concrete is shown for different temperatures (Noumowé, 1995). It can be seen that the total pore volume increases non-linearly with the temperature. The increase of porosity is quite small with respect to the weight loss up to 300 °C. In this phase, the pore structure changes inside are related to desiccation. The majority of dehydration processes occurring in the pores which have a radius smaller than 4 nanometers (Castellote et al., 2004). If they move to higher temperatures, total pore volume increases even significantly compared with the weight loss (Fig.2. 4).

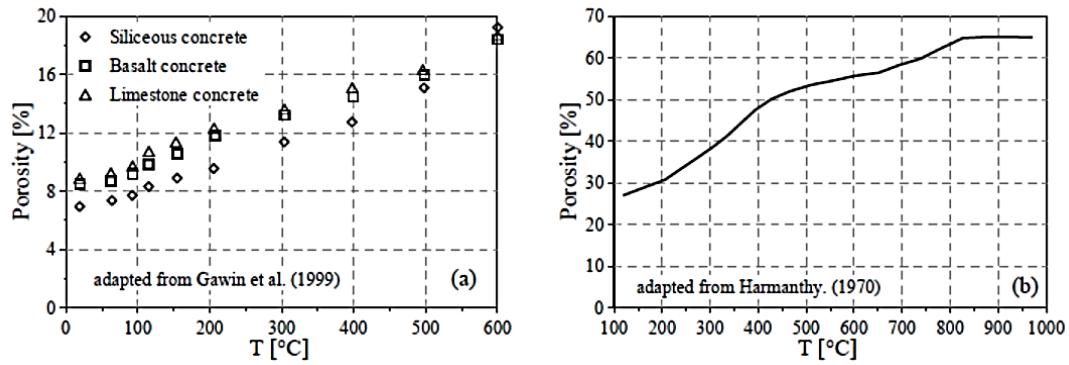


Fig.2. 5: (a) The total porosity at different temperatures (Gawin et al., 1999); and (b) Portland cement paste porosity as a function of the temperature (Harmathy, 1970).

Bazant and Thonguthai (1978, 1979) observed an upward jump in the permeability by two orders of magnitude. Several points can probably be related to the increasing pore volume available to capillary water, the decrease of water saturation, and a better connectivity of the pores (Castellote et al., 2004). Micro-cracking seems to play a primary role in permeability increasing. As it is mentioned above, the loss of interlayer and absorbed water and the dehydration of the cement paste increase pore volume and pore connectivity.

Porosity was also studied by Gawin et al. (Fig.2. 5).

The increase in porosity is caused by two main mechanisms (Tsimbrovska, 1997):

(i) $20^{\circ}\text{C} \leq T \leq 250\text{-}300^{\circ}\text{C}$: loss of adsorbed and interlayer water;

(ii) $T > 250\text{-}300^{\circ}\text{C}$: micro-cracking (due to dehydration and thermal incompatibility).

The same occurs for permeability. However, it is worth noting that between 20 and 400 °C porosity increases by about 30-100%, while permeability increases by more than 2 orders of magnitude (Bazant and Thonguthai, 1978, 1979).

The variation of the total porosity with temperature has been deeply studied by Schneider and Herbst (1989). The results proved that this variation can be approximated by a linear relationship:

$$n(T) = n_0 + A_n (T - T_0) \quad (2.1)$$

Where:

n : the porosity,

A_n : a constant depending on the type of concrete.

	Silicate concrete	Limestone concrete	Basalt concrete
n0 [%]	6.00	8.70	8.02
An [10⁻⁴ °C⁻¹]	1.95	1.63	1.70

Tab.2. 1 Experimental-obtained values for the parameters of Eq. 2.1.

Tab.2. 1 provided the values that are given starting from the experimental data suggested for different concrete types by Gawin et al. (1999).

$$n(T) = n_0 + 0.73 \cdot 10^{-3} \cdot m_{dehydr} \quad (2.2)$$

Where,

m_{dehydr} : The water mass expelled by dehydration, with the Le Chatelier contraction is taken into account (Feraille, 2000).

2.3 Density

As a result of the pore volume increase, the bulk mass density of the cement paste decreases with temperature from 1.45 g/cm³ at 105°C to 1.3 g/cm³ at 850°C. Changes in mass density result also from thermal expansion and drying shrinkage, diffusion of water or released gasses, and dehydration, melting, or sintering.

Concrete density depends on the density of the aggregates and on its moisture content. In Fig. 2. 6, it presents the variations of true density, bulk density, and porosity for a cement paste. Storage conditions is another important parameter at room temperature since it will have an influence on both the moisture content and the hydration degree of the cement paste. Aggregates play another important role because, for example, the dissociation of carbonate aggregates controls the significant reduction in density above 600°C.

In the same figure, it also presents the effect of aggregate-type on the density of concrete (T = 20-1000 °C).

From 150 °C to 600 °C the density of limestone concrete keeps rather constant.

From 600 to 900 °C de-carbonation of limestone and weight loss occurs as the concrete porosity increases.

Siliceous aggregates exhibit a steeper decrease in density because of the large thermal expansion of the quartz (T ≥ 700°C). Whereas basalt exhibits the smallest reduction in

density because of its lower thermal expansion.

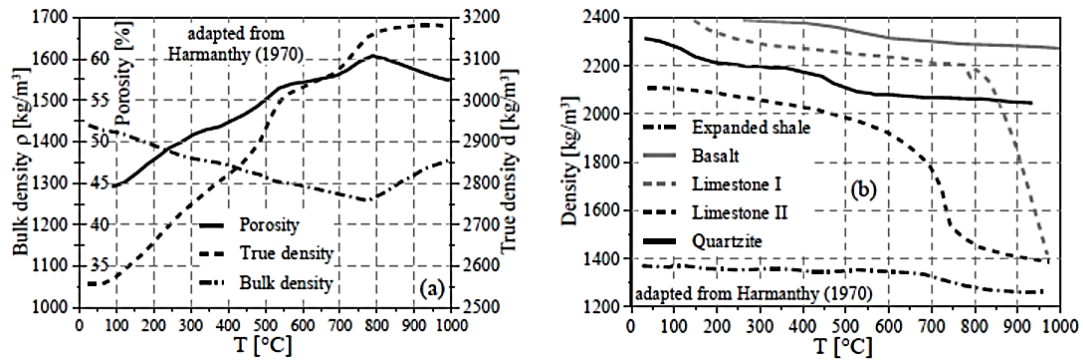


Fig.2. 6 (a) True density, Bulk density and porosity of cement paste versus temperature; and (b) density of concretes with different coarse aggregates (Harmathy, 1970).

2.4 Vapor Diffusivity

Daian (1989) has suggested that the diffusivity of vapor in dry air depends on both temperature and gas pressure. The expression is suggested by Equation(2.3)

$$D_{va}(T, p_g) = D_{v0} \left(\frac{T}{T_0} \right)^{A_v} \left(\frac{p_{g0}}{p_g} \right) \quad (2.3)$$

Where,

$D_{v0} = 2.58 \times 10^{-5} [m^2 / s]$: is the diffusivity of vapor in air at the reference temperature $T_0 = 0$ °C,

$$p_{g0} = 101325 [Pa],$$

A_v : is a constant, and a good correlation $A_v = 1.667$ was obtained with by Mason and Monchik, 1965).

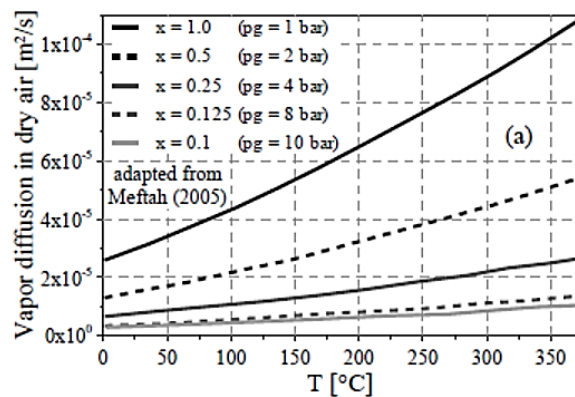


Fig.2. 7 Vapor diffusivity in dry air as a function of temperature and pressure, according to

$$\text{Equation(2.3), } x = p_{g0} / p_g$$

2.5 Thermal Properties

It is required for a determined thermal field so that can be taken out to analyze the structural response to fire and to evaluate the structural fire resistance. With this purpose, it requires a clear understanding of the thermal properties of the materials. If refer to concrete, the thermal parameters depend on the aggregate type and the initial moisture content. The type of coarse aggregate is one of the main factors affecting concrete properties ending temperature. There are three major types of aggregate: carbonate or calcareous, siliceous and lightweight, which are usually be referred to as fine, medium and coarse aggregates as well.

2.5.1 Thermal Conductivity

The thermal conductivity is the ability of material to conduct heat. It can be described by heat flux that transmitted through a unit area of a material under a unit temperature gradient. The thermal conductivity of concrete mainly depends on the thermal conductivity of the aggregates at normal temperatures. And at the time of heating, moisture content become the main factor, since the higher the aggregate-to-cement ratio means the lower the water-to-cement ratio so that the higher the concrete conductivity.

There are also other important factors: cement paste, pore volume and distribution, and water content, while the thermal conductivity at high temperature is rarely affected by the age. During heating, thermal conductivity firstly has a slight increasing up to 50-60 °C, then goes down and above 300 °C the increasing cracking favors this trend.

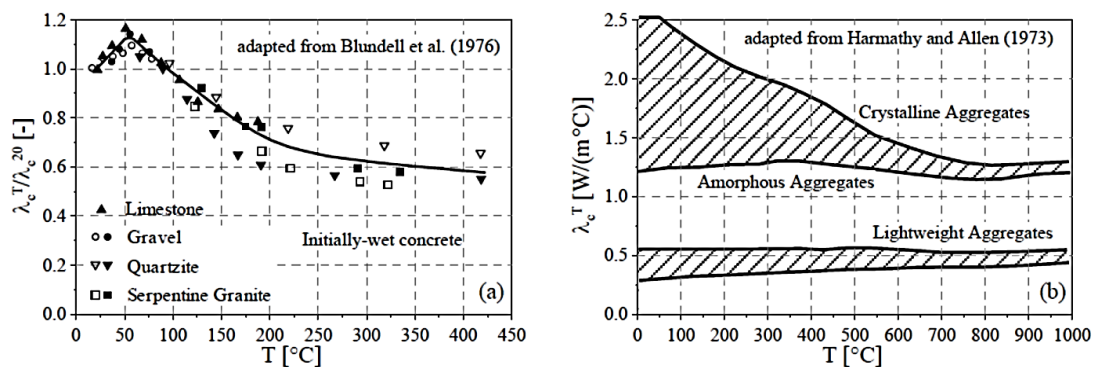


Fig.2. 8 (a) Thermal conductivity of initially-saturated concrete according to Blundell et al.

(1976), and (b) of different types of concrete according to Harmathy and Allen (1973), as a function of the temperature.

Aggregate type plays domination role in depending concrete thermal conductivity since it represents to 70 to 80 percent by mass of concrete. Light weight aggregates have higher porosity so that it determines lower thermal conductivity. Water conductivity is approximately 50 percent lower than that of cement paste. Similarly as the aggregates, the lower water contents mean the higher the conductivity of the harden concretes.

There is an example for different aggregates influence concrete thermal conductivity. For highly-crystalline aggregates, it decreases up to 1000 °C, while for the amorphous aggregate it keeps rather constant (Fig.2. 8).

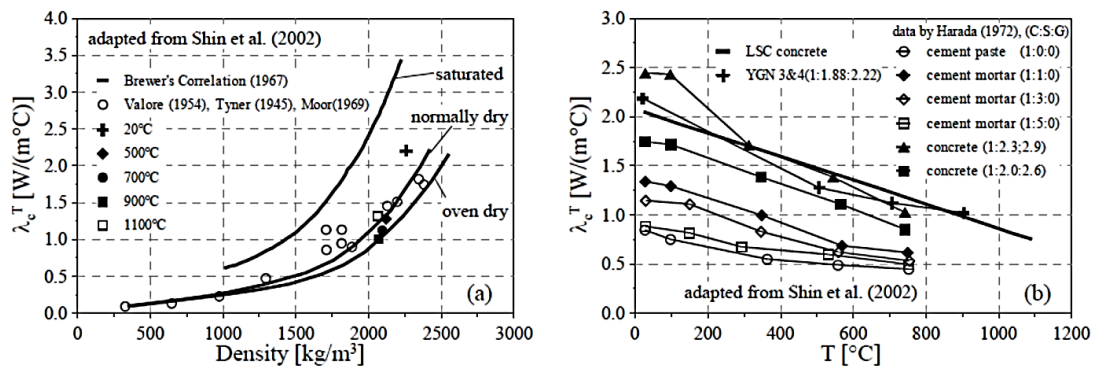


Fig.2. 9 (a) Thermal conductivity as a function of the density and moisture content; and (b) thermal conductivity as a function of the temperature, (Shin et al., 2002).

The concrete thermal conductivity can be plotted as a function of concrete density and moisture. It can also be a function of the temperature. These plots are presented in Fig.2. 9.

The formal literature has indicated that the major factors which will influence thermal conductivity of concrete are moisture content, aggregate type, cement paste, and pore volume and distribution. Furthermore, concrete conductivity goes linearly with moisture content and varies in a same trends with the aggregates conductivity. Concretes with lower cement paste content can be expected to have a lower conductivity than lean concrete mixtures.

The thermal conductivity on cooling depends on the maximum temperature reached during heating. After cooling to ambient temperature, the thermal conductivity falls to a level below the virgin concrete.

2.5.2 Thermal Diffusivity

Thermal diffusivity is the thermal parameter which controls the heat transmission by conduction. It is a measure of the rate when a material is enduring temperature variation that heat will diffuse at all directions. It is the ratio between the heat transmitted and stored by the unit mass of the material. It denotes the material's ability in transmitting heat when it is encountering temperature changes.

Thermal diffusivity is defined according to given function.

$$D = \frac{\lambda}{\rho c} \quad (2.4)$$

Where,

D is the thermal diffusivity m^2/s - ranging between 0.3 and 0.8 m^2/s ,

λ is the thermal conductivity $W/m \text{ } ^\circ C$,

c is the specific heat $J/Kg \text{ } K$

ρ is the density Kg/m^3 .

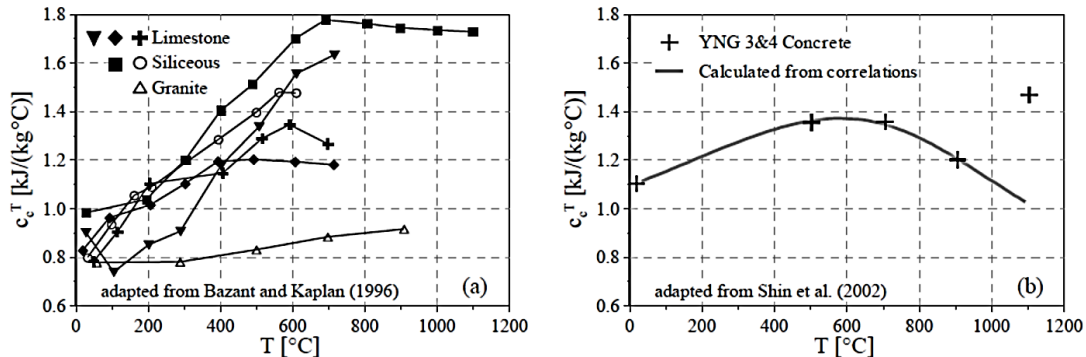


Fig.2. 10 Specific heat of various concretes according to (a) Bazant and Kaplan (1996), and of (b) a Korean nuclear power plant concrete (Shin et al., 2002).

Thermal diffusivity is important. Concrete thermal diffusivity can be determined from the thermal properties of its constituents. Same as conductivity, thermal diffusivity is firstly governed by the thermal diffusivity of the aggregates. Aggregates with increasing values of thermal diffusivity include basalt, rhyolite, granite, limestone, dolerite, and quartzite. Factors that affect thermal conductivity generally have the same influence on thermal diffusivity.

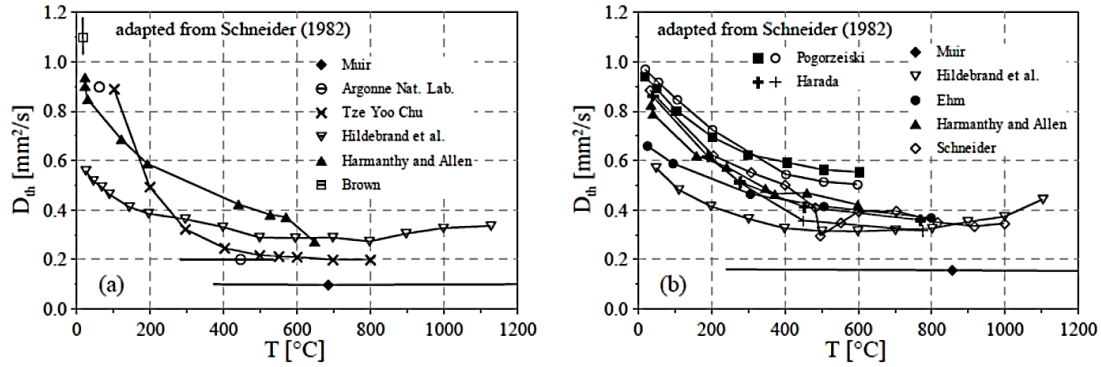


Fig.2. 11 Thermal diffusivity of limestone (a) and siliceous (b) concretes (Schneider, 1982).

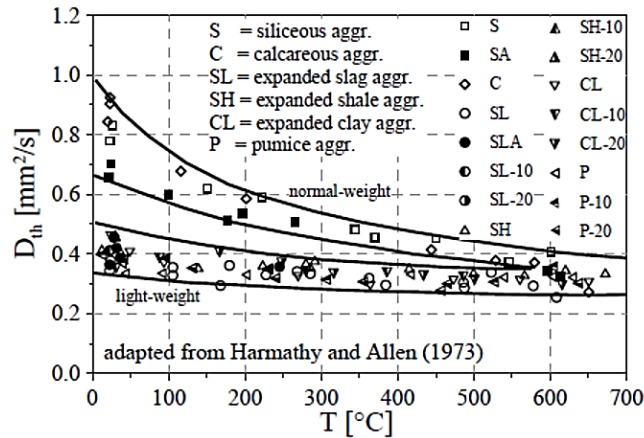


Fig.2. 12 Thermal diffusivity of normal and lightweight concretes, as a function of the temperature (Harmathy and Allen, 1973).

In Fig.2. 11 (Schneider, 1982) and Fig.2. 12 (Harmathy and Allen, 1973), the thermal diffusivity is plotted for different concretes. At about 600°C the thermal diffusivity of all concretes is close to $0.33 \text{ mm}^2/\text{s}$.

2.5.3 Specific Heat

The heat capacity is the amount of heat per unit mass required to change the temperature of the material by one degree.

$$c_p = \left(\frac{\partial H}{\partial T_p} \right) \quad (2.5)$$

Where,

H : is the enthalpy,

T : is the temperature,

p : is the pressure.

At room temperature, the specific heat of ordinary concrete ranges from 0.5 to 1.13

$\text{kJ}/(\text{kg } ^\circ\text{C})$, while the specific heat of cement paste ranges from 0.63 to 1.72 $\text{kJ}/(\text{kg } ^\circ\text{C})$. At room temperature, aggregate type, mix proportions, and age do not have a great effect on the specific heat of concrete. If the moisture content in the concrete increases, the specific heat capacity increases. The specific heat of concrete can be determined based on the mineralogical content of the aggregates and its relative proportions.

Concrete specific heat increases with the temperature. At elevated temperature, specific heat is sensitive to the various transformations that take place in concrete. Heating initially saturated concrete causes a rapid but temporary rise in the specific heat which usually results by the rapid release of latent heat of vaporization (Bazant and Kaplan, 1996). The specific heat can be plotted as a function of the temperature for a basalt-aggregate concrete used in the construction of Yonggwang Nuclear power plant units 3 and 4 in Korea. The specific heat increases up to 500 $^\circ\text{C}$, then decreases from 700 $^\circ\text{C}$ to 900 $^\circ\text{C}$, and increases at temperatures above 900 $^\circ\text{C}$.

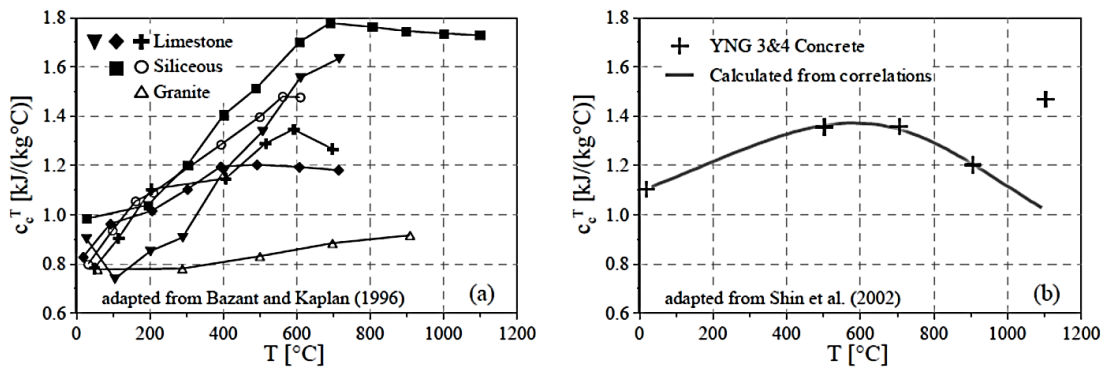


Fig.2. 13 The specific heat (a) of various concretes according to Bazant and Kaplan (1996), and (b) of a Korean nuclear power plant concrete (Shin et al., 2002)

2.5.4 Thermal Expansion

The coefficient of thermal expansion in a material is a parameter that represents the change per unit length which results by a unit variation of the temperature. It is given as a change in length per degree of temperature change. It is an important coefficient in evaluating the structural displacements and the heat-induced thermal stresses during a fire. Concrete thermal expansion results from the interaction of its two main components, aggregates, and cement paste, each of which has its own thermal behavior.

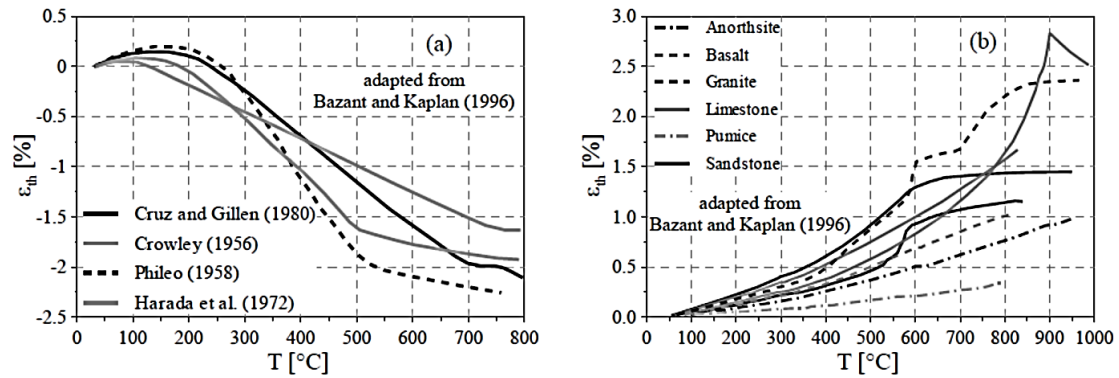


Fig.2. 14 The thermal strain (a) of Portland cement paste and(b) of different aggregates, as a function of the temperature (Bazant and Kaplan, 1996).

The intrinsic thermal expansion differences between aggregates and cement paste cause tensile stresses to split in the cement paste and will be followed by micro-cracking.

It is rather difficult to have an observation of thermal expansion in concrete since there will be various extraneous effects, such as additional volume changes, chemical reactions, creep, micro-cracking, etc., inside that accompanies the temperature changes.

2.5.4.1 Aggregates

Fig.2. 14 (Bazant and Kaplan, 1996) presents that Compare with natural materials, such as rocks, processed lightweight aggregates (expanded slag, shale, or clay) have lower coefficients of thermal expansion.

Aggregates generally make up most of the concrete mix. Thus, they should be the primary influence of the coefficient of thermal expansion. Selection of aggregates with a low coefficient of thermal expansion, which also be referred as thermal stability, may help in crack prevention. Silica contents form the main factor that affects the coefficient of thermal expansion. Aggregates with little or no silica (e.g. limestone) have the lowest coefficient of thermal expansion.

2.5.4.2 Cement paste

Fig.2. 14 also presents the elongation of the cement paste at elevated temperature. The hardened cement paste expands up to approximately 150-250 °C at the start, while the maximum expansion is on the order of 0.2% at 100-150 °C. Then from 300 till 800 °C cement paste shrinks (by -1.6 to -2.2% at 800 °C; see Bazant and Kaplan, 1996). The initial expansion has been attributed to the kinetic molecular movements in the cement paste

which are accompanied by swelling pressures that caused by a decrease in capillary tension of water as the temperature increases.

Below 150-200 °C thermal expansion has the upper hand over the shrinkage. At 200-300°C thermal shrinkage and thermal expansion could balance each other. At higher temperatures thermal shrinkage exceeds thermal expansion. Shrinkage of the cement paste results from loss of evaporable and chemically-combined water (Bazant and Kaplan, 1996).

2.5.4.3 Concrete

The thermal expansion of concrete is a resultant coefficient that is dominated by the aggregate type. The values of the coefficient for concretes range from 2.2 to 3.9 [$10^{-6} \text{ } ^\circ\text{C}^{-1}$]. It depends on the age and type of curing as well, being influenced by the moisture content of the cement paste, with minimum values in dry and saturated conditions. The thermal strain increases with the temperature as a result of aggregate expansion which is dominating over cement paste shrinking.

In Fig. 2. 15a, it presents the thermal strain of Portland cement paste, mortars and concretes for up to 871°C.

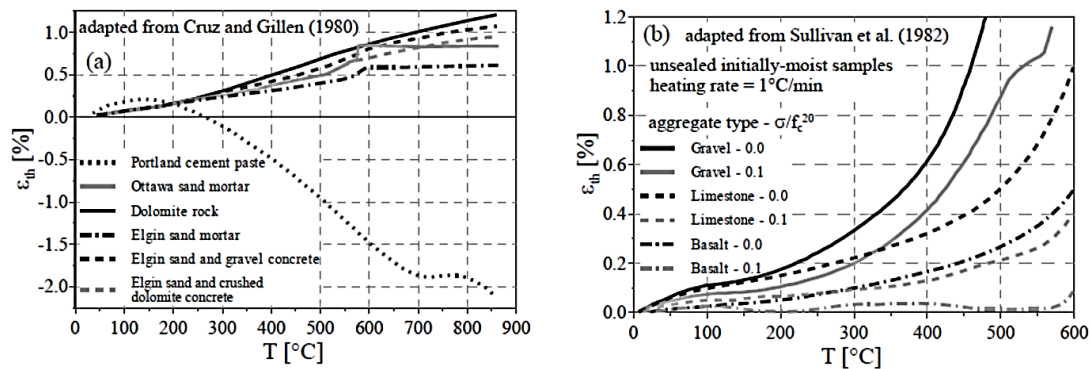


Fig.2. 15(a) Portland cement, mortar, and concrete according to Cruz and Gillen (1980), and (b) Portland cement concretes subjected to different load levels according to Sullivan et al. (1982), as a function of the temperature.

Lightweight-aggregate concretes may shrink at temperatures greater than 300°C. Tests on sealed concrete indicate that under thermal cycling permanent expansive strains occur after the first cycle, and the permanent expansion increases with an increasing number of cycles but a decreasing rate, as well as the thermal coefficient, decreases as the number of cycle increases. Moreover, specimens which allowed drying after the initial heating show

less expansion during any subsequent thermal cycles. For limestone concrete, until de-carbonation leads to a reduction of the coefficient, there exists an approximately monotonic increase in the thermal expansion coefficient.

The thermal expansion of siliceous concrete is greater than limestone concrete. Basalt concrete exhibits a lower expansion than siliceous concrete thanks to its fine crystalline structure. The presence of the loads reduces the thermal expansion as noted in Fig.2. 15b.

2.6 Mechanical Properties

Although the structural resistance to fire is not directly applicable to the material, the properties of the material still determine the structural behavior. It is necessary to study the influence of high temperatures on the mechanical behavior when it is about to define the fire resistance of an element in concrete.

The chemical reactions will affect concrete constituents during heating together with the interaction between aggregates, inducing a remarkable deterioration of its mechanical response. Durability and serviceability will be significantly influenced by high temperature, hence the physical deterioration processes may lead to severe cracking.

During fire, the mechanical decay of concrete may be denoted by three material factors:

- (i) Physic-chemical changes in the cement paste.
- (ii) Physic-chemical changes in the aggregates.
- (iii) Thermal incompatibility between aggregates and cement paste.

Only above 550-600 °C cement-based materials lose their resistance capacity evidently. At lower temperatures, the decay of the mechanical properties, which is mainly expressed as compressive strength and elastic modulus, can be reduced by choosing a proper mix formula, by which the CaO/SiO₂ ratio is low produced, or in another word, the thermally stable aggregates of low thermal expansion and cement blends are selected.

In Equation(2.6), according to Buchanan (2001), concrete deformation is usually described by assuming that the total strain ε consists of four components.

$$\varepsilon = \varepsilon_{th}(T) + \varepsilon_{\sigma}(\sigma, T) + \varepsilon_{cr}(\sigma, T, t) + \varepsilon_{tr}(\sigma, T) \quad (2.6)$$

Where,

$\varepsilon_{th}(T)$: represents the thermal strain, which is a function of the temperature,

$\varepsilon_{\sigma}(\sigma, T)$: represents the instantaneous stress-related strain, which is a function of both the applied stress and the temperature,

$\varepsilon_{cr}(\sigma, T, t)$: represents the creep strain, which is a function of the stress, temperature, and time,

$\varepsilon_{tr}(\sigma, T)$: represents the transient strain, which is a function of both the applied stress and the temperature.

A positive aspect of heated concrete needs to be recalled in order to explain the changes of concrete mechanical properties as a function of the increasing temperature. Concrete does not break up when the ambient temperature is lower than 100 °C. Though the differential strain that results from the expansion of the aggregates and the shrinkage of the cement paste may be too large to be adapted by elastic strains.

This beneficial evidence is caused by the transient creep. It is the summation of creep $\varepsilon_{cr}(\sigma, T, t)$ and transient $\varepsilon_{tr}(\sigma, T)$ strains, the so-called load-induced thermal strains, LITS. It develops during first heating, under load and is unique among structural materials. It will not develop during the cooling phase. Above 100 °C it is essentially a function of the temperature, while time plays a minor role. A typical LITS curve can be drawn for temperatures up to 450 °C as it is in Fig.2. 16, regardless of the aggregate type or cement blend used.

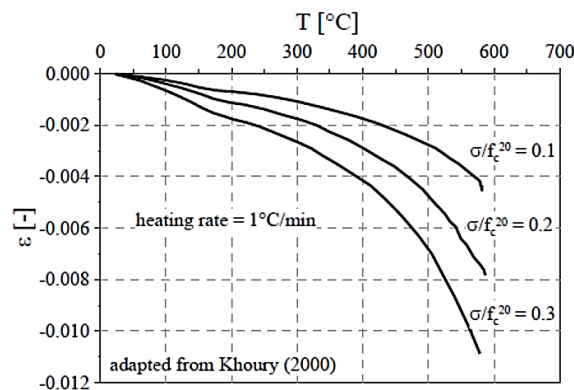


Fig.2. 16 LITS - of concrete during heating under compressive loads (Khoury, 2000).

When enduring high temperature, LITS are much larger than the elastic strains, and promote a significant relaxation and redistribution of the thermal stresses in heated

concrete. Any structural analysis of heat-exposed concrete that ignores LITS will be completely inappropriate and will yield absurd results, particularly for columns exposed to fire (Khoury, 2000).

There is a further positive aspect that is given by the beneficial influence of compressive loading during heating. This influence compacts concrete and cement paste and inhibits the development of cracks. As for unloaded concrete, the elastic modulus is more affected by the temperature than both tensile and compressive strength (Khoury, 2000).

2.6.1 Compressive Strength

Concrete compressive strength is based on the load-carrying capacity of a structure. Considered dependent on the temperature, the hot behavior of concrete in compression is generally described by a temperature-dependent stress-strain diagram, which depends on three parameters:

- (i) Compressive strength f_c^T ,
- (ii) Strain at the peak stress ϵ_{cl}^T ,
- (iii) Elastic modulus E_c^T .

Though some codes take care only of the type of the aggregates, it should be proper to pay attention that the values of these properties also depend on aggregate content, heating rate and type of loading.

The physically combined water is released from concrete about 100 °C, while during the process the strength does not change. Then start from above 100 °C the elastic modulus decreases by about 10-20%. Above 300 °C the silicate hydrates decompose and above 500 °C the portlandite is dehydrated, so the compressive strength is limited reduced before 450-500 °C and rapidly after 500 °C. Temperatures higher than 500 °C can reduce concrete compressive strength to only a small fraction of its original value. This can be specially recognized in highly siliceous concrete according to Felicetti and Gambarova (1998). Such concretes are unlikely to possess any useful structural strength as they may contain a considerable amount of calcium oxide, which easily expands under moisture attack.

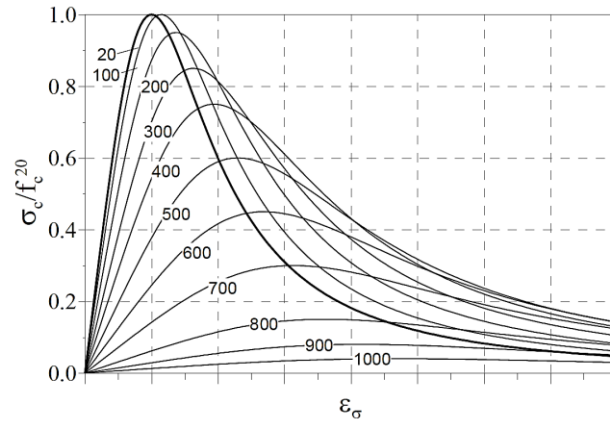


Fig.2. 17Temperature effect on the stress-strain curves of concrete.

At temperatures above 600 °C, some aggregates begin to convert or to decompose. In any case, even if spalling does not occur, the external layers are no longer able to carry any load whereas it still prevents the inner core from being overheated. It is somehow positive for a structural member on the fire resistance view.

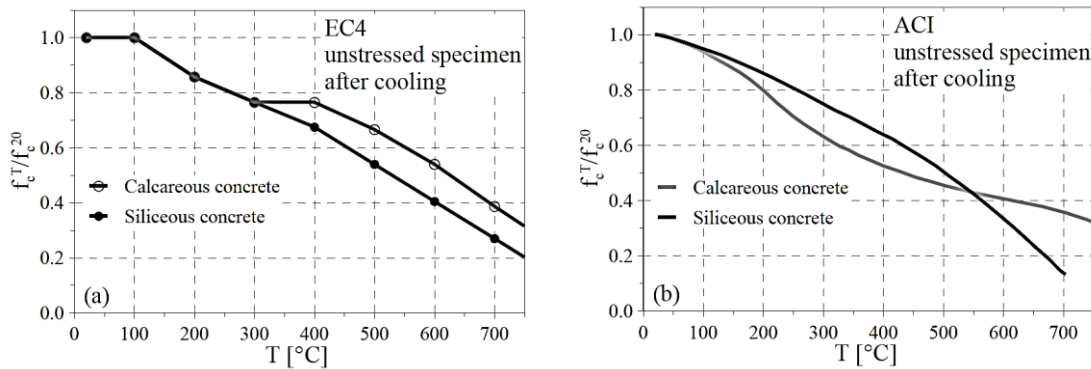


Fig.2. 18Residual compressive strength as a function of temperature according to (a) EN1994-1-2 (2004) and (b) ACI 216-1.07 (2007).

In Fig.2. 18, the effect of temperature on the residual compressive strength of Normal-Strength Concrete is shown respectively according to EN1994-1-2 (2004) and ACI 216-1.07 (2007).

Recently the research has extended the testing of compressive strength from Normal-Strength Concrete to High-Performance Concrete (HPC, $f_c = 60-130 \text{ Mpa}$) and even Ultra-High Performance Concrete (UHPC containing steel fibers, $f_c = 130-200 \text{ Mpa}$). The results plotted in Fig.2. 19 show that the residual strength of the HPC declines less with the temperature than that of the UHPC, but, possibly due to the steel fiber, that the reverse is true for the residual strength measured after cooling.

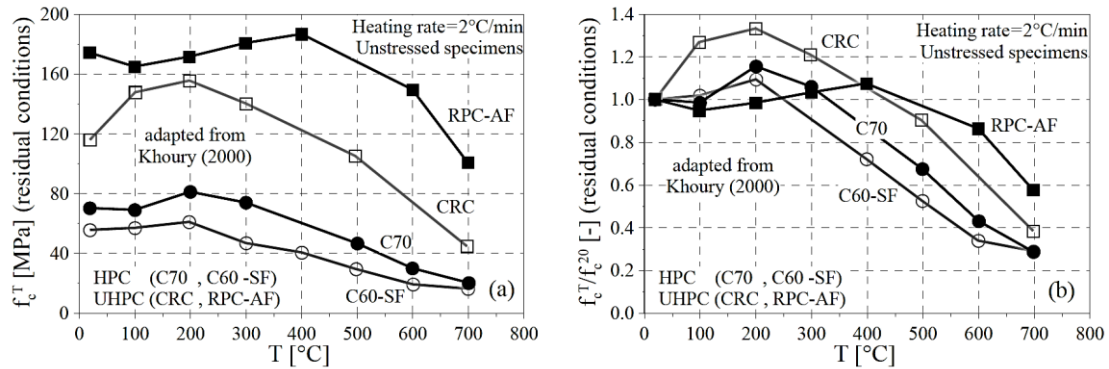


Fig.2. 19 The residual compressive strength of two HPC and two UHPC: (a) actual value; (b) values normalized with respect to the virgin strength (Khoury, 2000).

The relatively poorer hot performance of the UHPC could be blamed to its very dense structure, where moisture escapes relatively harder. Two effects induce by this fact:

(i) A physical effect due to reduced Van der Waals forces as water expands upon heating

(ii) A chemical effect whereby detrimental transformations can take place under hydrothermal conditions.

2.6.2 Tensile Strength

Tensile strength is related to avoiding or delay cracking. Direct measurements of concrete tensile strength are seldom made because of the difficulties in fastening the specimen to apply the loads and in maintaining a uniformly distributed tensile stresses in any section. The difficult is even more complex at high temperature. An indication of concrete tensile strength can be obtained by testing in indirect tension prismatic specimens subjected to 3- or 4-point bending tests, or prismatic/cylindrical disks subjected to splitting along the section aligned with the applied loads. These tests can be much more easily performed at high temperature than direct-tension tests.

Fig.2. 20a shows a result of tensile strength reduction with the temperature in hot conditions takes place at rather low temperature ($T \geq 100$ °C). The experiment proceeded consists in a horizontal concrete cylinder loaded in compression through bearing strips placed along two axial lines that are diametrically opposite.

Fig.2. 20b shows the residual tensile strengths for both NSC and High-Strength Concrete (HSC) will decrease similarly and approximately linearly with temperature

increasing. The tensile strength of the HSC remains 10-15% higher than that of the NSC over the entire temperature range. Which is correspond with expected is that, at any temperature, the tensile strength by splitting is larger than that in direct tension. The same result have been proved for the flexural tests as well.

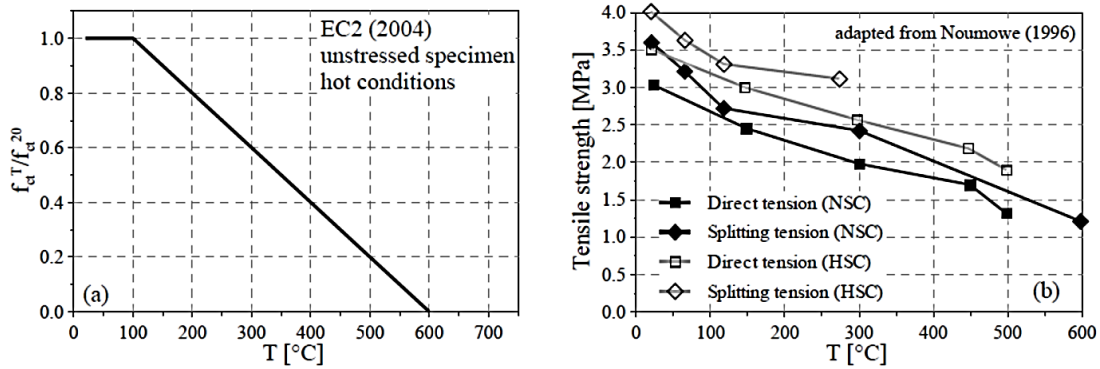


Fig.2. 20(a) The normalized tensile strength according to EN1992-1-2 (2004) in hot conditions, and(b) of High-Strength Concrete and Normal-Strength Concrete in residual conditions (Noumowe et al., 1996), as a function of the temperature.

High-Performance Concrete containing silica fume ($f_c = 60-130 \text{ MPa}$) is more sensitive to high temperature ($T = 100-800 \text{ }^{\circ}\text{C}$) than ordinary concrete, owing to its denser cementations matrix with lower diffusivity. And to the more important role of the aggregates, whose thermal decay is much more harmful. In Fig. 2. 21 the comparison between indirect tension strength (f_i^* , 3-point bending) and direct tension tests (f_t) is shown with respect to the temperature. It appears that the ratio f_i^*/f_t increases with the temperature.

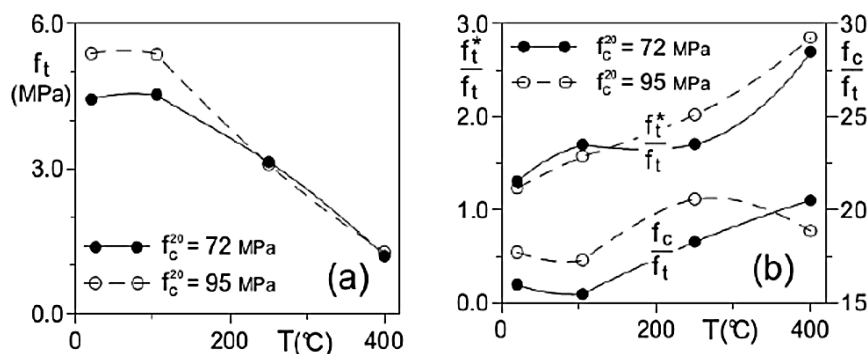


Fig.2. 21 Direct tension tests on notched cylinders: (a) plots of the residual strength; and (b) plots of two strength ratios ($f_c/f_t =$ compressive-to-tensile strength ratio; $f_t^*/f_t =$ indirect-to-direct strength ratio; indirect strength = 3-point bending; Felicetti and Gambarova, 1998).

It is clear that the tensile strength tends to decrease more than the compressive strength after heating, when considering the resistant mechanisms based on the tensile

strength, such as bond, bar tension-stiffening, web shear and punching shear (Felicetti and Gambarova, 1998).

The results on the tensile strength are limited available in the literature. Even though, from them, it can be concluded that aggregate type and mix proportions have a significant effect on the tensile strength, whose decrease in calcareous-aggregate concrete is twice as high as that of siliceous-aggregate concrete at 500 °C. Mixes with a rather low cement content are less heat-sensitive than mixes with a rather high cement content. Finally, the residual tensile strength is a bit lower than the tensile strength measured at elevated temperature.

2.6.3 Poisson Ratio

The knowledge of the Poisson ratio is needed for structural analyses of bi-dimensional and three-dimensional structures. In normal ambient conditions, the Poisson ratio of concrete can vary from 0.11 to 0.32, but is generally comprised between 0.15 and 0.20. In uniaxial compression, the beginning of matrix cracking corresponds to an apparent increase in the Poisson ratio. At ambient temperature, there is no consistent relationship between the Poisson ratio and concrete characteristics such as water-cement ratio, curing age, and aggregate size and type. It is generally lower in High-Performance Concrete and higher in saturated concrete and in dynamically-loaded concrete.

In Fig. 2. 22, it is given the plot that at 20°C the Poisson ratio is constant until the load exceeds about 70% of the ultimate load, while as the temperature increases the deviation of Poisson ratio increases. It indicates that the Poisson ratio decreases with increasing temperature from about 0.2 at room temperature to about 0.1 at 400°C. This drop is because of a change in state of heating that leads water desorption, for example, weakening of the microstructure caused by breakage of bonds due to heating and by micro-cracking. And if the specimen is allowed to cool after a given change in state, the variation of the Poisson ratio with temperature is slight and nil when the evaporable water is removed.

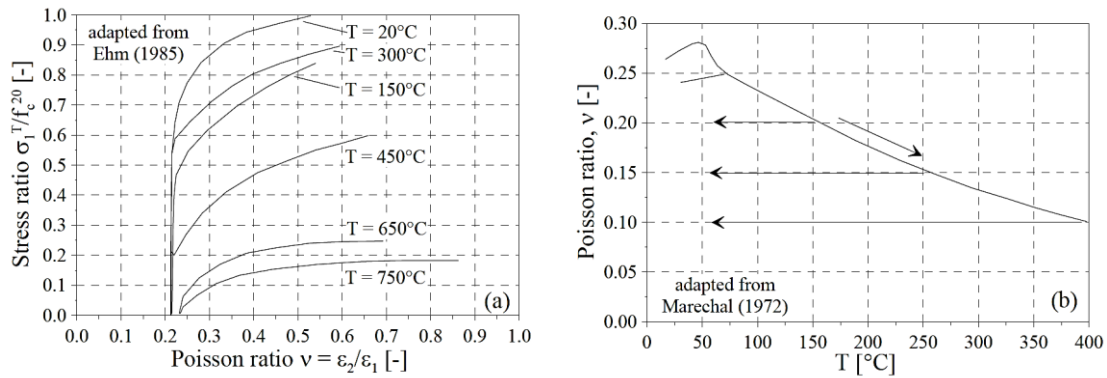


Fig.2. 22(a) The normalized stress as a function of the Poisson ratio, for different temperatures (Ehm, 1985); and (b) the Poisson ratio as a function of the temperature (Marechal, 1972).

Poisson ratio could also be presented as a function of the temperature for different aggregate types and two nominal concrete compressive strengths, according to Fig.2. 23. The values generally ranged from 0.11 to 0.25. Though the results obtained at higher temperature were a bit erratic and without a general trend apparent, it did show lower Poisson ratio values at room temperature for higher strength concretes.

Additionally, the Poisson ratio in High-Strength Concrete has also been reported to range from 0.11 at 20 °C to 0.25 at 400 °C, while above 400 °C it increases (Wu et al., 2000).

Besides, according to Bamonte and Gambarova (2010), it can be clearly indicated that in a siliceous High-Strength Concrete ($f_c = 125 \text{ MPa}$), the residual Poisson ratio increases up to 0.30-0.35 for $T = 250\text{-}350 \text{ }^\circ\text{C}$, and then tends to decrease. For example, the value of the Poisson ratio is close to that of the virgin material (i.e. 0.15) at 600 °C.

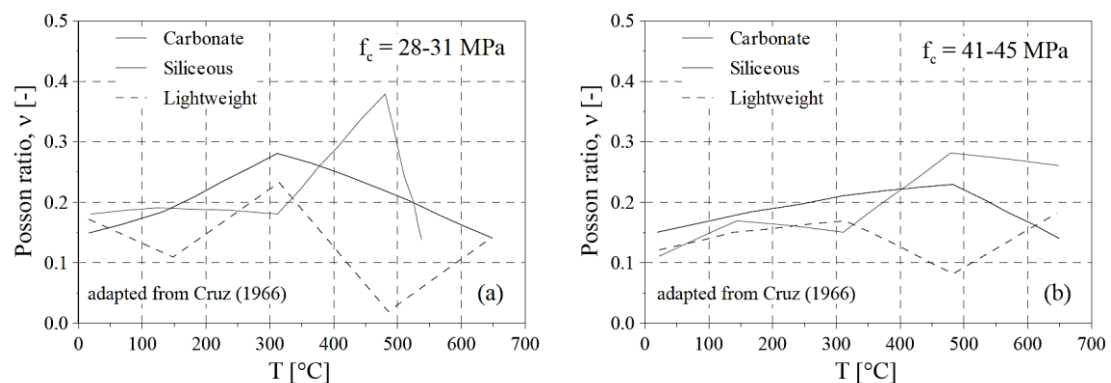


Fig.2. 23 Effect of aggregate type and concrete strength on Poisson ratio (Cruz, 1966).

2.6.4 Elastic modulus

Elastic modulus is a measure of concrete's stiffness or resistance to deformation,

which is used extensively in the analysis to determine the stresses and displacements. Many studies in the past showed that the elastic modulus depends mainly on concrete compressive strength. Thus it is proper to describe that the elastic modulus is affected by the same factors that affect the compressive strength. The factors include cement type, water-cement ratio, aggregate type, loading conditions during heating, maximum reached temperature. Besides these parameters, only the aggregate type and the loading conditions during heating have a sizable influence on the elastic modulus. The modulus is more temperature sensitive than the compressive strength both at high temperature and after cooling, as a matter of the fact that concrete stiffness is directly affected by thermal cracking.

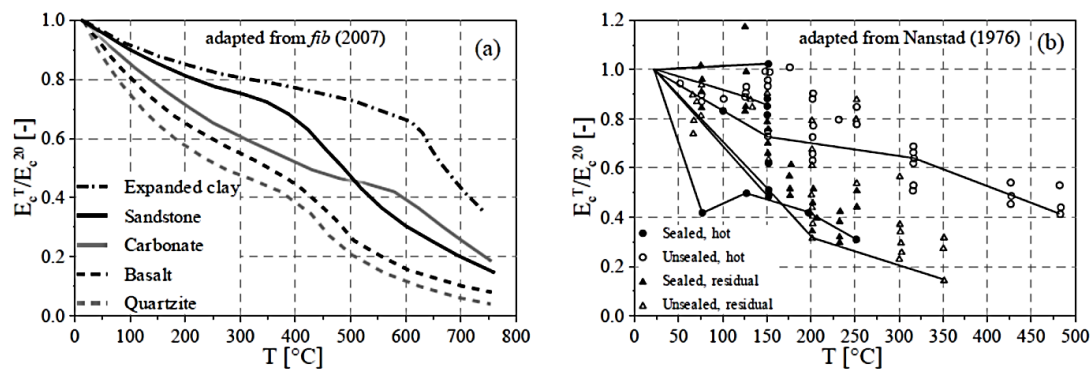


Fig.2. 24 The normalized concrete elastic modulus for (a) different aggregate types according to fib (2007), and for (b) different sealing conditions according to Nanstad (1976), as a function of the temperature.

For siliceous aggregates, the ratio E_{cT}/E_{c20} is 0.4-0.5 at 500 °C, while light-weight aggregates are close to or better than calcareous aggregates. For instance, E_{cT}/E_{c20} is up 0.70-0.75 for expanded clay at 500 °C. These data can be referred from Fig.2. 24

Fig.2. 24 also presents a summary of data assembled for sealed and unsealed specimens that were tested at a temperature or after cooling. Generally, during all kind of test, elastic modulus decreases with increasing temperature. Further decreases in modulus occurred can be observed with an increase in a number of thermal cycles and exposure time. Moreover, sealed specimens are more sensitive to these factors, with the elastic modulus decreasing evidently at temperatures above 150°C.

2.6.5 Fracture Energy

Fracture energy G_f is defined as the total amount of energy dissipated for the propagation of a crack per unit area. It given the evolution of the normalized fracture energy as a function of the temperature by Heinfling(1998). According to Zhang and Bicanic (2001), the decrease at 105 °C is mainly caused by the rise in pore pressure due to water vaporization. If the moisture content is higher, the decrease of fracture energy will also be higher. For higher values of the temperature that is above vaporization, the effect of pore pressure becomes negligible and fracture energy increases. Up to 300 °C further cement hydration helps recovery. Above 300 °C, micro-cracking, dehydration, and decomposition cause a reduction of fracture energy.

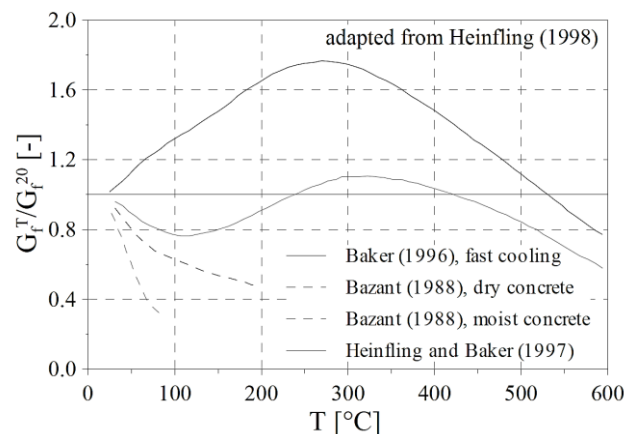


Fig.2. 25 Normalized fracture energy G_f as a function of temperature (Heinfling, 1998).

Several experiments have been done by different authors. And in any case, the experimental results show a sizeable scattering also because of the lack of uniformity in the definition of fracture energy. However, for example, on the basis of the research that has been done by Felicetti and Gambarova (1998), compare with tensile and compressive strength, and elastic modulus, fracture energy is much less temperature-sensitive than the other mechanical parameters. In the present work, fracture energy will be given a further discussion in further chapter.

2.7 High-Performance Concrete

Different from the early research, starting from the eighties of last century, concrete with increasing compressive strengths became commercially available and primarily

utilized in the construction of high-rise buildings. High-Performance Concrete provided quantity economic advantages, including reduced size concrete columns, permission of lighter structures and more usable space. Given that low permeability is also a kind of High-Performance, HPC was also used in the construction of pre-stressed girders for bridge decks and other specialized applications.

High-Performance Concrete can be produced primarily through the use of relatively low water-binder ratios and often incorporates silica fume and/or fly ash. In this way, the permeability is reduced with respect to Normal-Strength Concrete. Concerns arose about the possible higher susceptibility of High-Performance Concrete to explosive spalling under fire conditions, since the pore pressure in the cement paste should be higher. Recently, High-Performance Concrete behavior at high temperature has become a critical issue.

Based on several authors' works, the following considerations can be made:

Consider varying with the temperature, the material properties of High-Performance Concrete (HPC) behaves differently from those of Normal-Strength Concrete (NSC). The differences are more pronounced when higher strength concretes have higher rates of strength loss than lower grade concretes, which should be referred to the temperature range between 25 °C and about to 400 °C. These differences become less significant above 400 °C. At 800 °C, compressive strength of HPC decreases to about 10-30% of the virgin one;

In non-stressed and stressed tests in hot conditions on HPC, the variations of compressive strength with the temperature are characterized by three stages:

- (i) Initial stage of strength loss (25 °C ~ 100 °C),
- (ii) Stage of stabilized strength and/or recovery (100 °C ~ 300-400 °C),
- (iii) Stage above 300-400 °C characterized by a monotonic strength decrease with increase in temperature;

In contrast, HPC has a higher rate of compressive strength loss in the temperature range between 100 °C and 400 °C than NSC;

For non-stressed residual compressive tests on HPC, the strength-temperature relationships are characterized by two stages: an initial stage of minor strength gain or loss from 25 °C to 200 °C, and a stage above 200 °C in which the strength decreases with

increasing temperature;

The strength recovery stage of higher grade concretes more likely occurs at higher temperatures than lower grade concretes. The compressive strength of HPC obtained from stressed compressive tests is higher than those obtained from the non-stressed and non-stressed residual tests in the temperature range of 25-400 °C. Pre-loading reduces the strength loss in this range of temperature. Besides, increasing the pre-load levels from 25 to 55% of the virgin compressive strength does not increase significantly the compressive strength of HPC at high temperature.

3. Concrete Spalling at High Temperature

The spalling phenomenon is the violent or non-violent breaking off of layers or pieces of concrete from the surface of a structural member when it is exposed to more or less rapidly rising temperatures, as experienced in fires with heating rates typically in the range 10-30 °C/min.

Spalling can be subdivided into four categories : (i) Aggregate spalling, (ii) Explosive spalling, (iii) Surface spalling, and (iv) Corner/sloughing-off spalling.

The first three types of spalling occur during the first 20-30 minutes of a severe fire and are influenced by the heating rate, while the fourth occurs after 30-60 minutes and is influenced by the maximum reached temperature (Khoury, 2000).

The breaking-off of the material comes in different ways (Institution of Structural Engineers – ISE, 1975):

(i) *Explosive spalling*: this is a violent form of spalling. It occurs at an early stage of the heating process and may result in extensive damage or complete destruction of the concrete member;

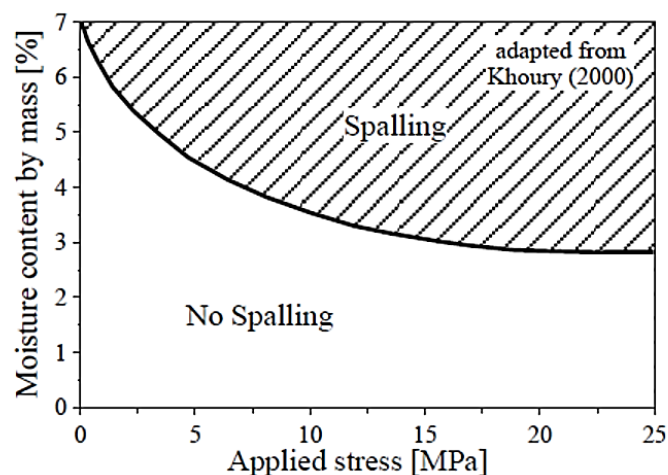


Fig.3. 1 Explosive spalling: an empirical envelope for Normal-Strength Concrete, showing the influence of moisture content and applied stress (Khoury, 2000).

(ii) *Local spalling*: this consists. Aggregate spalling is caused by aggregate failure close to the surface and includes small pieces expelled from the surface. Since only superficial damage is produced, this type of spalling does not adversely affect the structural performance;

(iii) *Sloughing off*: this is a process of breakdown, it involves partial separation of material from the concrete member. Corner spalling occurs in the decay stages. It is characterized by larger corner pieces breaking-off of the concrete due to tensile cracks developing close to the corners and edges. Due to the late occurrence of this type of spalling, concrete are already weakened. Corner spalling may not have a significant impact on structural fire performance.

Considering the fact that explosive spalling induces the greater threat to structural stability, it will be investigated in more detail.

In current design codes like Eurocode 2 there is not much information about spalling. It is stated that no checks for spalling are necessary if the moisture content of the member is less than 3% and that the tabulated data can be used to prescribe generic fire ratings for concrete members (Fig.3. 1).

For concrete grades in the range C80/95 - C90/105, spalling can occur in any situation when there is a direct exposure to the fire and four methods are recommended to be used, regarding reinforcement mesh, concrete type, protective layers and inclusion in the concrete mix of more than 2 kg/m³ of monofilament polypropylene fibers.

3.1 Factors Influence Spalling

The main factors influencing concrete spalling in fire are listed as the following:

Material: permeability, saturation level, aggregate type, fiber type and content, presence of cracking and reinforcement,

Geometry: section shape and size,

Environment: heating rate, heating profile, load level.

The main factors are: heating rate, permeability, pore saturation level, reinforcement (if any) and loading (Khoury, 2000).

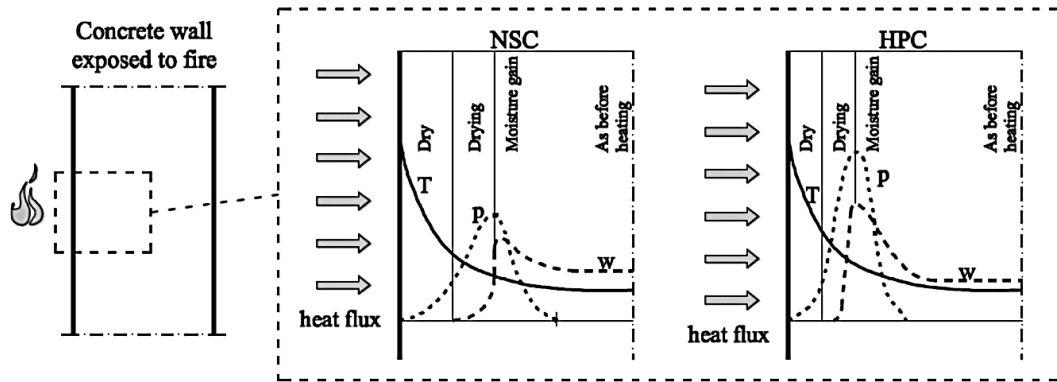


Fig.3. 2 Profile of temperature, pore pressure and moisture content in Normal-Strength and High-Performance Concrete wall exposed to fire (after Khoury, 2000).

Low-permeability HPC is more likely to explosive spalling, and with respect to NSC it is easier to experience multiple spalling, despite the higher tensile strength of the former. This is because higher values of pore pressures during heating are expected to have low permeability. Thinner concrete sections spall from HPC in a fire because the peak pressure occurs near the surface for HPC. The high compactness is the main parameter for HPC that is responsible for its higher spalling sensitivity at high temperature (Fig.3. 2). If compares the experimental results concerning NSC and HPC, both with calcareous aggregates, it can be observed that their global thermal behavior is similar, due to their similar thermal properties.

The difference regards pore pressure is up to 4-5 MPa in High-Performance Concrete and 1-2 MPa in the Normal-Strength Concrete (Felicetti et al., 2012; Felicetti and Lo Monte, 2013).

As a consequence of the lower permeability of HPC, the thermodynamic conditions reached in the porous network of HPC are very different from those of NSC, which results in much higher pore pressures.

As an overview of the experimental results on different types of concrete, the main factors contributing to spalling are the aggregate-binder and the water-cement ratios. As regards High-Performance Concrete, low water-binder ratios bring in a greater susceptibility to spalling because of the very dense concrete structure. Though low water-binder ratios imply higher strength and lower porosity, this will lead to higher pressures and increase material spalling sensitivity. In order to design concretes with low

spalling sensitivity, it is necessary to understand what the mechanisms are that lead to this phenomenon.

There are at least three causes of explosive spalling: *pore pressure, thermal stresses and thermal cracking.*

3.2 Pore Pressure Spalling

Pore Pressure Spalling is a mechanism that is driven by the pressure build-up inside concrete pores due to water vaporization. It ensued pressure gradients cause the transport of liquid water, vapor and dry air in the porous matrix. Part of the vapor is pushed towards the hot face so it can be released into the environment, while the part is forced towards the inner and cooler core and condensate, causing a local increase of the pore water saturation.

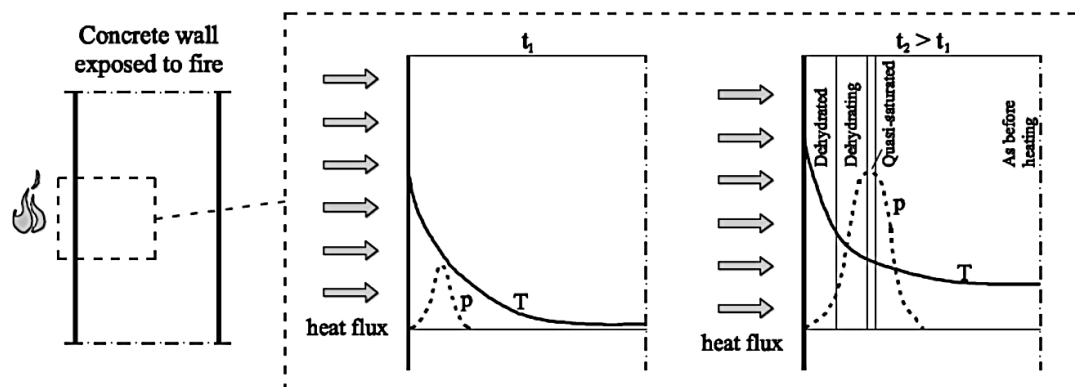


Fig.3. 3The process for the build-up of pressure in a concrete wall exposed to fire (after Zeiml et al., 2006).

As a result, a quasi-saturation layer can be formed. The material can be divided now into four zones (Fig.3. 3): (1) dry and dehydrated zone, (2) drying and dehydrating zone, (3) quasi-saturated layer, and (4) virgin zone far away from the heated surface.

The quasi-saturated layer is the critical zone, as in HPC this increased value of saturation can reach saturation, leading to the so-called moisture clog. The pressure build-up is favored by situation, so that it can reach very high values (up to 5 MPa). The lower the permeability, the higher the probability of moisture clog and the higher the pressure (Yufang, 2010). The pressure inside the pores acts on the cement matrix as a tensile action and when the critical level is attained, spalling occurs. However, how to define the value of pore pressure needed to cause concrete fracturing is still an open issues.

3.3 Thermal Stress Spalling

The low concrete thermal diffusivity combined with the high heating rate will result in sizable thermal gradients in concrete members. These thermal gradients induced compressive thermal stresses in the heated face and tensile stresses in the inner core. Compressive stresses cause vertical cracking and a decrease of the stability of the external layers. Both aspects are favored by spalling.

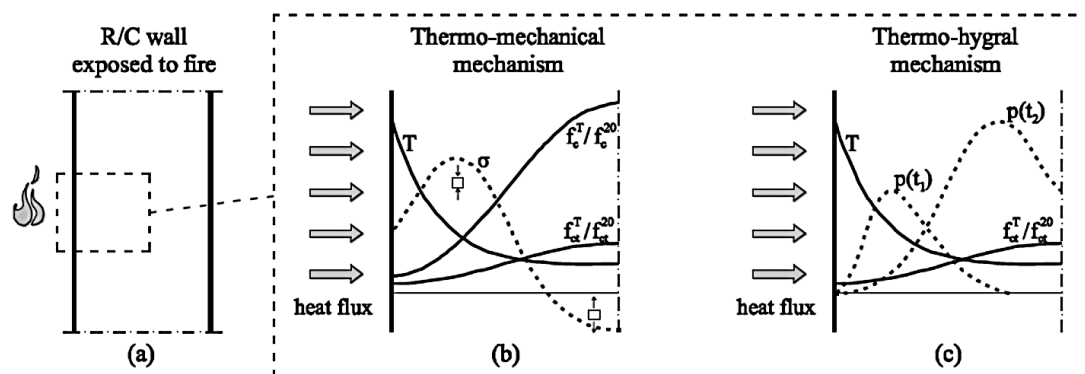


Fig.3. 4Concrete spalling mechanisms in a heat-exposed wall: qualitative diagrams of (a) the temperature T and of the normalized tensile strength f_{ct}^T/f_{ct}^{20} (b,c), of (b) the thermal stress σ and normalized compressive strength f_c^T/f_c^{20} , and of (c) pore pressure p for two different values of fire durations, $t_2 > t_1$.

3.4 Thermal Cracking Spalling

Cracking in heated concrete is favored by the material heterogeneity and the occurring chemo-physical reactions.

Several factors influence concrete cracking during heating:

- (i) The release of absorbed and chemically bound water,
- (ii) The thermal kinematic incompatibility between aggregates and cement paste,
- (iii) Cement dehydration.

Thus, thermal cracks can be divided into three types:

- (i) Shrinking cracks induced by the release of absorbed and chemically bound water,
- (ii) Cracks caused by the tensile action since the cement paste has different thermal behavior with respect to the aggregates,

(iii) Internal and external cracks induced by temperature gradients, (Yufang, 2010).

The last mechanism which is acting in parallel to the two previous can lead to explosive spalling, which is most severe from structure view.

4. Thermal Problem

It is the priority need to describe the thermal field inside the specimen which is enduring heating, whenever the investigation of high-temperature effects is carried out. With proper assumption, the maximum temperature of a certain point can be linked to the degradation at the same point. As most experimental measurements of the temperature are discrete so that they cannot be performed at any given point of a specimen, the thermal field is often obtained through numerical analysis. The analysis should consider the thermal properties of the materials, the fire scenario and the boundary conditions of the structure.

Owing to the above-mentioned, a theoretical basis for heat transfer is in need to be discussed from both the physical and mathematical point of view.

4.1 Heat Transfer Mechanisms

Heat is a chaotic form of energy. It develops in a process that leads to dissipative phenomena (friction, Joule effect, etc.), and it is more difficult to convert heat into other storable energy.

Heat transfer occurs between physical systems with different temperatures by dissipating heat. It takes place through three mechanisms: (i) Conduction, (ii) Convection, and (iii) Radiation.

4.1.1 Conduction

Conduction is energy transport without macroscopic mass movement, usually, it is defined inside a certain domain. Heat transport takes place only because of the collision among the molecules, which lead to particles kinetic energy variation.

Consider a plate of a homogeneous and isotropic material. Assuming it is bounded by two parallel surfaces Γ_1 and Γ_2 at a distance L , and for each surface, there is uniform values of temperature, T_1 and T_2 , respectively ($T_1 > T_2$).

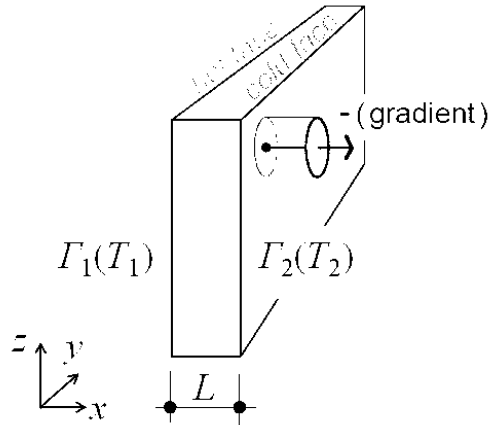


Fig.4. 1Heat transfer inside a plate made by homogeneous and isotropic material

Let the values of temperature be maintained for a sufficient time, the isothermal planes inside the plate be parallel to the external faces and the heat flux be perpendicular to these planes. The second law of thermodynamic has stated that energy transport takes place always from the points at higher temperature to those at lower temperature. So heat moves from T_1 to T_2 . Equation (4.1), so-called Fourier Law, gives the evaluation function that the total amount of heat Q moved through the area A in the time interval Δt :

$$Q = \frac{\lambda A}{L} (T_1 - T_2) \Delta t \quad (4.1)$$

It allows to define conductivity λ , generally expressed in terms of specific heat flux:

$$\dot{q} = \frac{Q}{A \Delta t} = \frac{\lambda}{L} (T_1 - T_2) \quad (4.2)$$

As it is mentioned in Section 2.6, the material properties, include density, specific heat and thermal conductivity, should be known.

ρ : density, mass of the material per unit of volume [kg/m^3],

c_p : specific heat, heat required to increase 1 °C per unit mass [$J kg^{-1} K^{-1}$],

λ : thermal conductivity, amount of heat that passes a unit cross section of the material through a unit of time, by the action of one thermal gradient unit ($\Delta T / \Delta L = 1$) [$W m^{-1} K^{-1}$].

In the present work, the material properties are introduced according to EN 1992-1-2:2004 (E) suggestion for further implementation. For density, the variation of the property is given by the Equation(4.3) and plotted in Fig.4. 2, with $\rho(20^\circ C)$ is equal to $2400 kg/m^3$.

$$\begin{aligned}
\rho(t) &= \rho(20^\circ\text{C}) && \text{for } 20^\circ\text{C} \leq t \leq 115^\circ\text{C} \\
\rho(t) &= \rho(20^\circ\text{C}) \cdot (1 - 0.02(t - 115)/85) && \text{for } 115^\circ\text{C} \leq t \leq 200^\circ\text{C} \\
\rho(t) &= \rho(20^\circ\text{C}) \cdot (0.98 - 0.03(t - 200)/200) && \text{for } 200^\circ\text{C} \leq t \leq 400^\circ\text{C} \\
\rho(t) &= \rho(20^\circ\text{C}) \cdot (0.95 - 0.07(t - 400)/800) && \text{for } 400^\circ\text{C} \leq t \leq 1200^\circ\text{C}
\end{aligned} \tag{4.3}$$

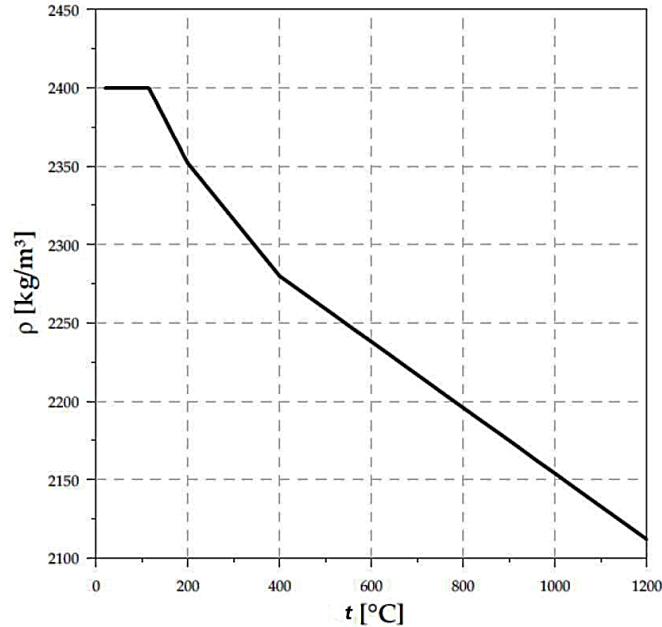


Fig.4. 2 Density variation according to EN 1992-1-2:2004 (E).

In Chapter 2, it is underlined that the trend of the specific heat as a function of temperature is not strongly influenced by the type of aggregates, instead, it is linked to the moisture content at the time of heating.

The specific heat c_p of the dry concrete may be determined, may be determined from Equation(4.4) for both Siliceous and calcareous aggregates according to EN 1992-1-2:2004 (E):

$$\begin{aligned}
c_p(t) &= 900(J/kgK) && \text{for } 20^\circ\text{C} \leq t \leq 100^\circ\text{C} \\
c_p(t) &= 900 + (t - 100)(J/kgK) && \text{for } 100^\circ\text{C} \leq t \leq 200^\circ\text{C} \\
c_p(t) &= 900 + (t - 200)(J/kgK) && \text{for } 200^\circ\text{C} \leq t \leq 400^\circ\text{C} \\
c_p(t) &= 1100(J/kgK) && \text{for } 400^\circ\text{C} \leq t \leq 1200^\circ\text{C}
\end{aligned} \tag{4.4}$$

Where t is the concrete temperature (°C).

When the moisture content is not considered explicitly in the calculation method, the function is given as the specific heat of concrete with siliceous or calcareous aggregates may be modeled by a constant value, $c_{p,peak}$, situated between 100 °C and 115 °C with linear

decrease between 115 °C and 200 °C:

$c_{p,peak} = 900 \text{ J/kg K}$ for moisture content of 0 % of concrete weight,

$c_{p,peak} = 1470 \text{ J/kg K}$ for moisture content of 1.5 % of concrete weight,

$c_{p,peak} = 2020 \text{ J/kg K}$ for moisture content of 3.0 % of concrete weight.

And the linear relationship between 115 °C and 200 °C. For other moisture contents, a linear interpolation is acceptable. The plot of specific heat is illustrated in Fig.4. 3.

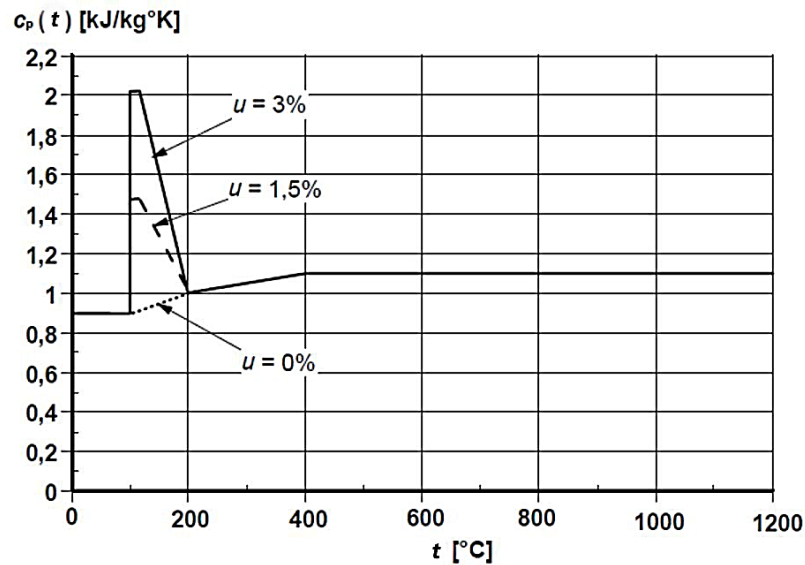


Fig.4. 3 Specific heat c_{p} , as a function of temperature at 3 different moisture contents u , of 0, 1,5 and 3 % by weight for siliceous concrete, EN 1992-1-2:2004 (E).

Also, the thermal conductivity of the concrete varies depending on the temperature, particularly it is influenced by the type of aggregate and the initial moisture content.

The Eurocode 2 defines an upper limit and a lower limit for thermal conductivity, through which it is possible to interpolate the values so as to be able to better characterize the material. According to, the equations that define these limits are respectively given in Equation(4.5):

$$\lambda_c^{\max}(t) = 2 - 0.2451 \left(\frac{t}{100} \right) + 0.0107 \left(\frac{t}{100} \right)^2$$

$$\lambda_c^{\min}(t) = 1.36 - 0.136 \left(\frac{t}{100} \right) + 0.0057 \left(\frac{t}{100} \right)^2 \quad (4.5)$$

The variation of the upper limit and lower limit of thermal conductivity with temperature is illustrated in Fig.4. 4.

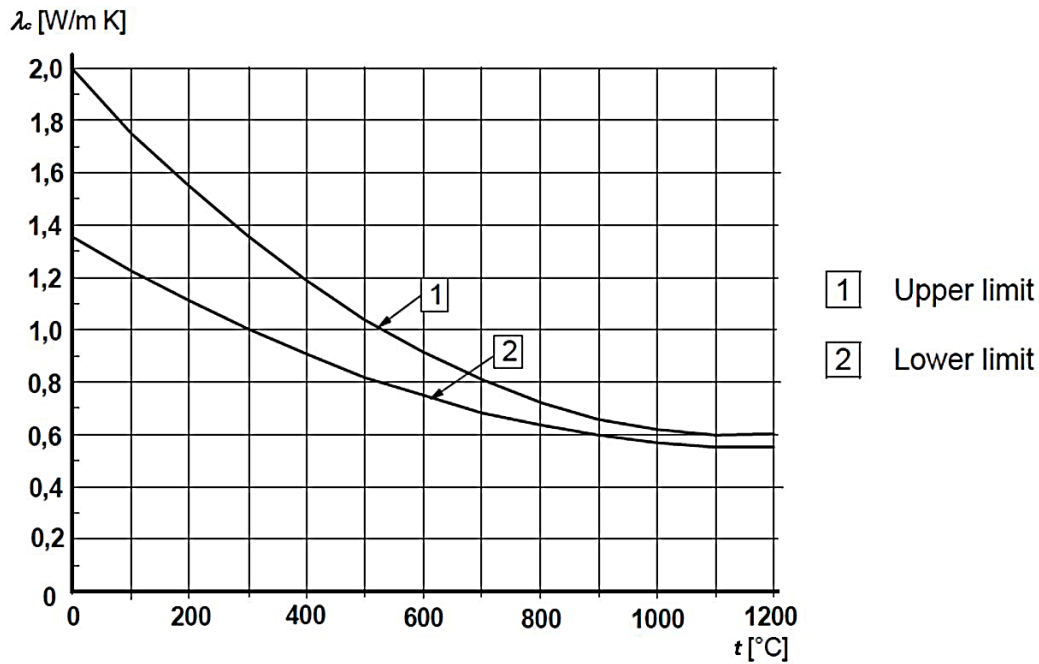


Fig.4. 4 Thermal conductivity of concrete according to EN 1992-1-2:2004 (E).

The thermal diffusivity is also defined by Equation(2.4). Then another derivative property, thermal inertia i_T [W^2s/m^4K^2], is also necessary to be known and given by Equation (4.6)

$$i_T = k \cdot \rho \cdot c_p \quad (4.6)$$

When the material with low thermal inertia is subjected to heating, the surface temperature increases rapidly, hence the ignition of the material should be very fast.

4.1.2 Convection

Convection is the heat transport taking place due to the contact between two bodies in relative motion. It characterizes the heat transfer between a solid body and its surrounding fluids.

Considering a solid body with external surface temperature of T_1 and its surrounding fluids at a temperature of T_2 (where $T_1 > T_2$), according to Newton Law:

$$\dot{q} = \alpha_c (T_1 - T_2) \quad (4.7)$$

The convection coefficient α_c is permitted to be defined by Equation(4.7). To emphasize, α_c is both strictly dependent on the characteristics of the fluid and linked to the parameters defining the relative motion of the fluid with respect to the solid. A typical value

for structural elements exposed to fire is $25 \text{ W/m}^2\text{K}$ (Buchanan, 2001).

4.1.3 Radiation

Radiation is defined as the heat transport by means of emission and absorption of electromagnetic waves radiated by a hot body. Stefan in 1798 first defined the expression to generate the heat flux by a surface at the absolute temperature T , and later the Boltzmann demonstrated the evaluation method theoretically in 1884.

$$\dot{q} = \sigma \cdot T^4 \quad (4.8)$$

Where,

σ : is the Stefan-Boltzmann constant, with $\sigma = 5.67 \cdot 10^{-8} \text{ [W/m}^2\text{K}^4]$.

The radiative heat flux per unit surface area is determined according to EN 1991-1-2 by Equation(4.9)

$$\dot{q} = \sigma \cdot \varepsilon_m \cdot \varepsilon_f \cdot \Phi \cdot (T_f^4 - T_m^4) \quad (4.9)$$

Which is described for a member with emissivity ε_m at a thermodynamic temperature of T_m exposed to a fire with emissivity ε_f (generally equals to 1) at a thermodynamic temperature of T_f .

4.2 General Numerical Modelling

4.2.1 General Equations according to Fourier Law

In Civil Engineering, conduction is considered as the main mechanism of heat transfer, while convection and radiation are usually considered as boundary conditions that define the thermal loads acting on the surfaces of the domain. For an isotropic, homogeneous and continuous body, the specific heat flux of two surfaces at a distance dx can be evaluated according to the *Fourier Law*. The balance of fluxes can be written as Equation(4.10).

$$\frac{\partial}{\partial x} \left(\lambda \frac{\partial T}{\partial x} \right) = \nabla \cdot (\lambda \cdot \nabla T) \quad (4.10)$$

Now define the concepts of stored energy and internal heat source. Then enforce the conservation of energy at any time for the unit volume. The stored energy can be expressed by the product of density and specific heat ρc_p , which actually refers to the specific heat per

unit mass, and the partial derivative of the temperature T with respect to the time t , and is the sum of ingoing and outgoing fluxes and the internal energy (per unit volume) H . The *Energy Conservation Equation* is expressed by Equation(4.11)

$$\rho \cdot c_p \frac{\partial T}{\partial t} = \nabla \cdot (\lambda \nabla T) + H \quad (4.11)$$

In the present work, it takes a very simple example into the analysis, so the equation needs to be simplified according to some reasonable assumption. The first assumption is that the conductivity of material is space invariant, with a constant value λ . So the Equation(4.12) is obtained.

$$\frac{\partial T}{\partial t} = \frac{\lambda}{\rho \cdot c_p} \nabla^2 T + \frac{H}{\rho \cdot c_p} \quad (4.12)$$

Another easier calculated assumption is to assuming no internal heat sources, which means $H = 0$. Therefore, if $D = \lambda/\rho c_p$ is the thermal diffusivity as defined in Chapter 2, Equation(4.12) can be further simplified so that Equation(4.13) is obtained.

$$\frac{\partial T}{\partial t} = D \cdot \nabla^2 T \quad (4.13)$$

4.2.2 Initial and Boundary Conditions in Fire Design

Defining a reasonable initial and boundary conditions is a fundamental request to solve the thermal problems in the most appropriate way, as previously mentioned. Generally, in real cases, the initial condition should be the initial temperatures in the member or structure, simplified as a single value for all the points. Usually, the ambient temperature is carried out as the initial condition.

The boundaries of the tested region can be considered as two part: hot and cold surface. For the hot surface, the thermal load is usually described by a firing curve for convection and radiation heat transfer, with corresponding coefficients taking a reference *EN 1991-1-2 (2004)*. The cold surface can be dealt by implementing the ambient temperature, an adiabatic boundary (Tan and Yao, 2003). A heat sink is even closer to the real situation. Generally, the thermal gradient at the cold surface is low, which indicates a small value of heat fluxes. Besides, if the adiabatic is imposed, it will lead to higher temperatures, which brings the benefit of safety consideration.

5. Benchmark in Crack Behavior Study

As it is mentioned in Chapter 2, there were rarely direct experiments aimed at evaluating concrete tensile strength or elastic modulus decay with temperature under different levels of load during heating, because of the complex material behavior at high temperature. Hence, it would be interesting the development of a numerical method aimed at elastic modulus investigation in fire.

The present work addresses the study of a numerical algorithm to evaluate the decay of concrete stiffness with temperature via an inverse analysis starting from experimental data, expressed in terms of stress profile and tested member curvature during heating. In this way, consideration on concrete stiffness decay will be carried out. On the other hand a few aspects concerning cracking behavior will be tackled, by using both a commercial software (Abaqus) and an algorithm implemented in Matlab.

5.1 Numerical Simulation in Commercial Software

Numerical simulations are performed in ABAQUS, in order to have a reliable benchmark to check the results obtained via the algorithm implemented in Matlab. Moreover a few considerations on modelling cracking behavior, in particular fracture energy and characteristic length, will be carried out as regards Abaqus model.

In this chapter, a 2D beam, which is under thermal loading in one direction while subjected to pure compressive load, is used as an example. The simulations of thermal and mechanical are both carried out in ABAQUS.

A simple algorithm is developed by MATLAB to simulate the same specimen tested in ABAQUS. Several comparisons are made between ABAQUS results and the algorithm results. By the comparison of two results, it could be fulfilled to understand how the software works with the property implemented (mainly regarding fracture energy and characteristic length).

5.2 Heat transfer analysis in ABAQUS

5.2.1 Geometry

In this chapter, a beam section with height of 0.1 meters and length of 1 meter is introduced to represent the property. Thanks to the symmetry of geometry and loading, just one half of the specimen can be modelled.

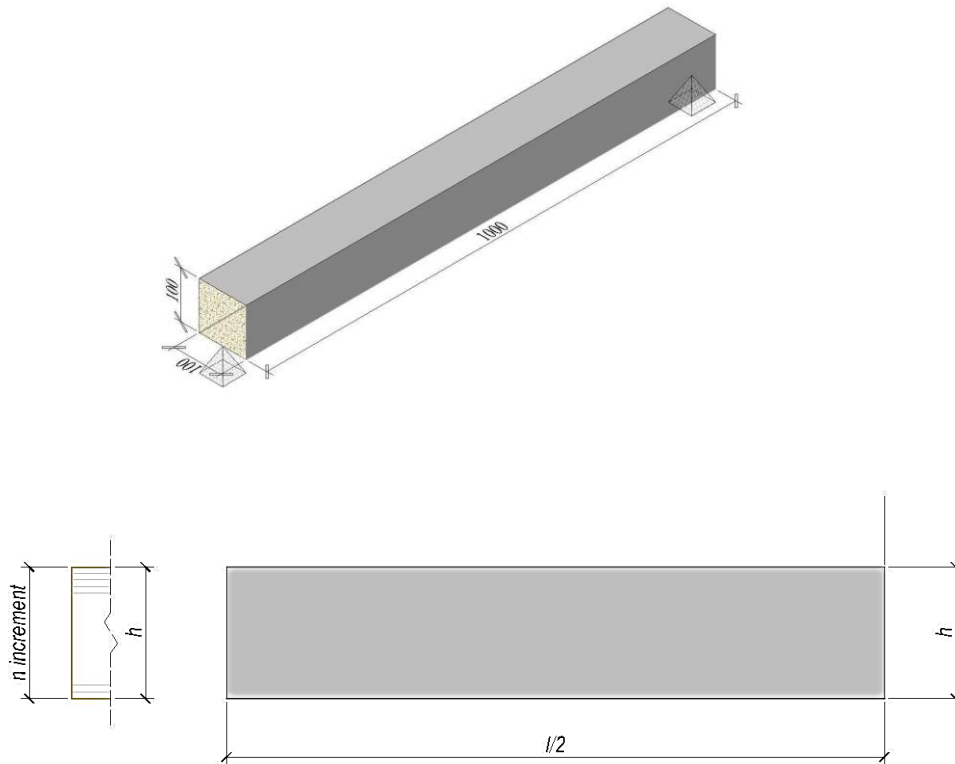


Fig.5. 1 Geometry of the beam studied by numerical simulation

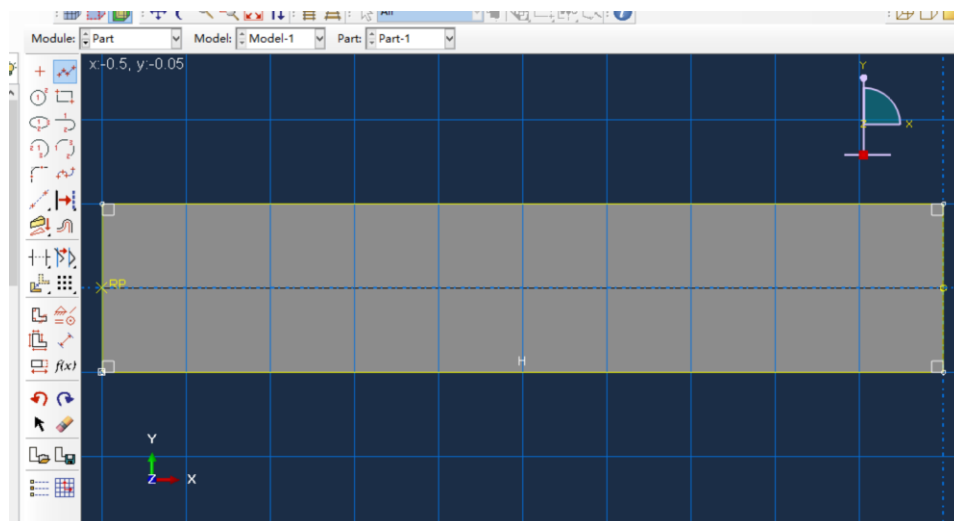


Fig.5. 2 Geometry studied by numerical modelling

5.2.2 Thermal Effects

5.2.2.1 Temperature Curve

As abovementioned in Chapter 2, heat load is applied according to Standard Fire, for two hours (7200 seconds).

The ISO834 temperature-time curve is implemented as the Standard Fire according to *EN 1991-1-2 (2004)* (the equation has been given by Equation(1.1) and the plotted in Fig. 1. 3).

5.2.2.2 Thermal Properties Implementation

Material density, thermal conductivity, and specific heat are implemented in ABAQUS according to the information given in Chapter 4.

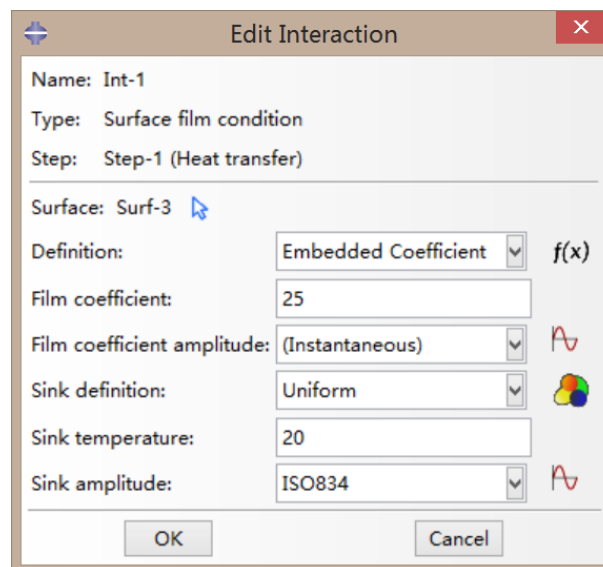


Fig.5. 3 Surface film condition in ABAQUS

A typical value of convection for structural elements exposed to fire is $25 \text{ W/m}^2\text{K}$ (Buchanan, 2001).

The interaction property should be given to the specimen in order to perform the analysis. In this case, the convection is defined in *surface film condition* (Fig.5. 3).

5.2.3 Thermal Profile

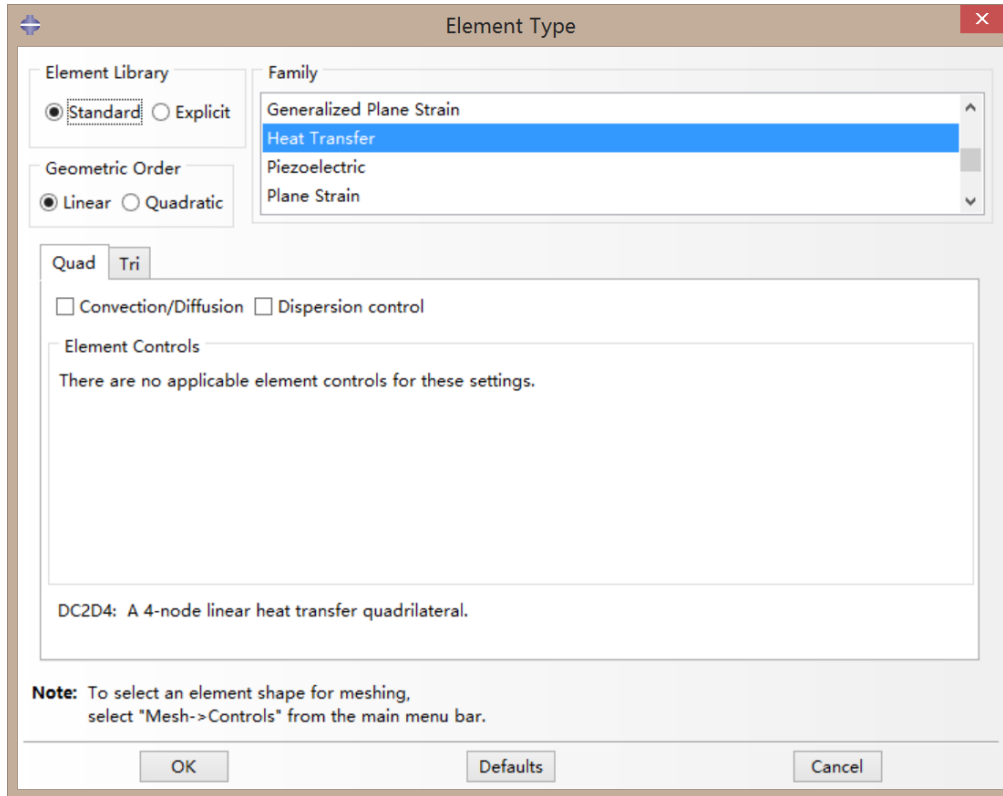


Fig.5. 4Element type for simulation in ABAQUS

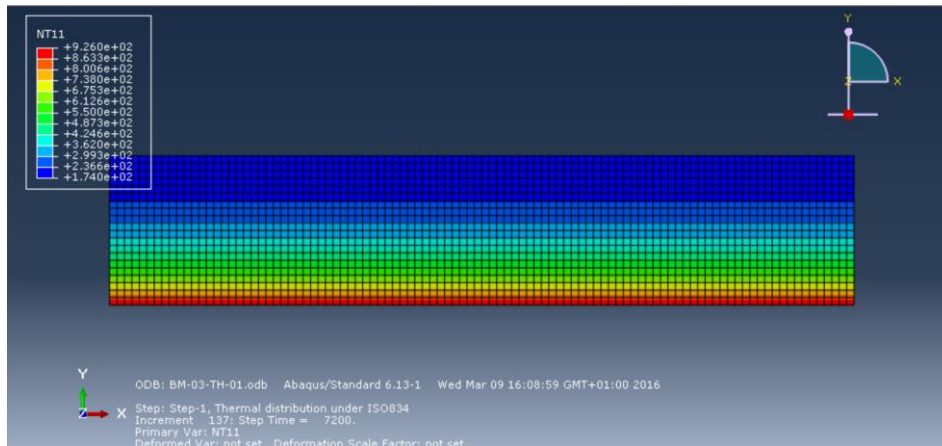


Fig.5. 5Temperature distribution at the end of heating (7200s) in ABAQUS

The simulation was performed for a fire duration of 2 hours, 7200 seconds. The performed element is *Heat transfer Quadratic element DC2D4* (Fig.5. 4), with a mesh size of 5x5 millimeters.

After running the simulation the temperature distribution are obtained. Fig.5. 5 gives the temperature distribution at the final time step. It can be observed that the highest value of temperature is about 926°C. By selecting the symmetric axial section (Fig.5. 6), as

sample, the thermal profile can be plotted for different fire durations (Fig.5. 7). Such distribution profile is also the input for the following mechanical simulation.

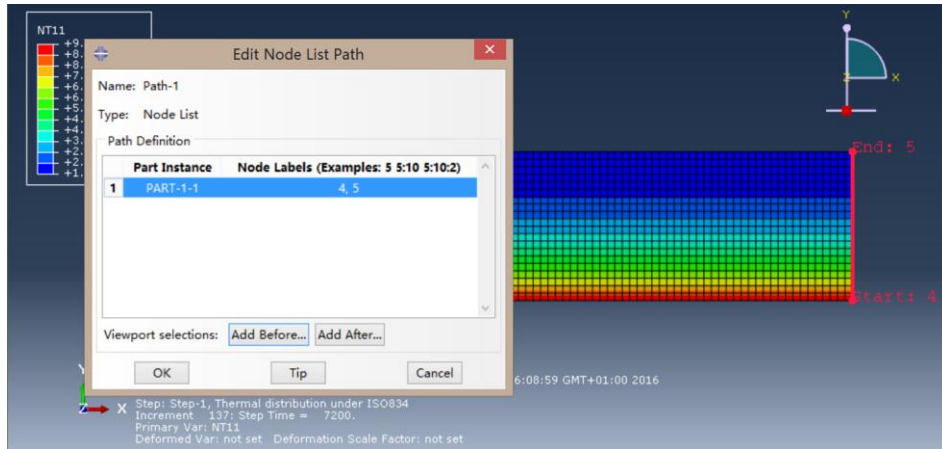


Fig.5. 6 Sample section for temperature distribution profile

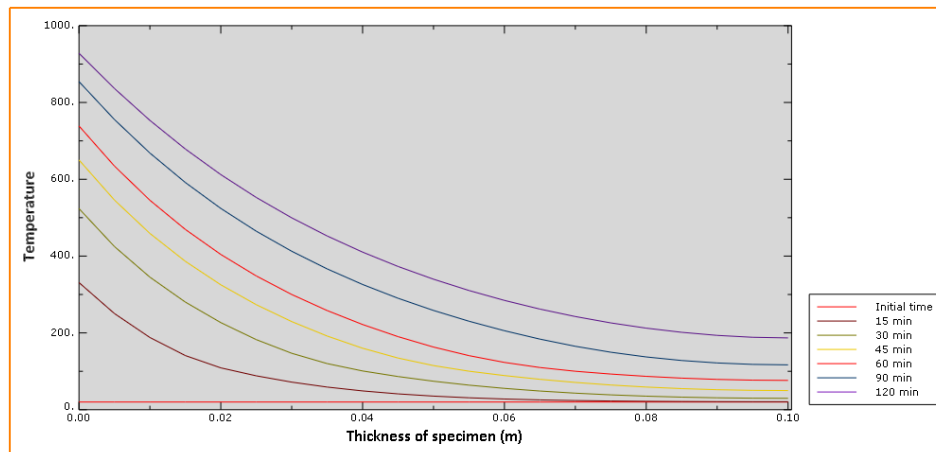


Fig.5. 7 Plot of temperature distribution profile as a function of time

5.3 Mechanical Analysis in ABAQUS

Since the target of the current step is forming a benchmark, it is reasonable to use well-understood material properties for implementation. The behavior of the concrete at high temperature is strongly influenced by many factors. For this reason, despite the number of studies and experimental campaigns, it is difficult to predict at the design stage the hot behavior or in residual conditions of the materials and of the structures. In order to provide a clear, although simplified, in this chapter the properties given by European standards Eurocode 2 Fire Design will be used.

Eurocode *EN1992-1-2 (2004)* gives explicit suggestion about concrete numerical values on strength and deformation properties, based on steady-state as well as transient

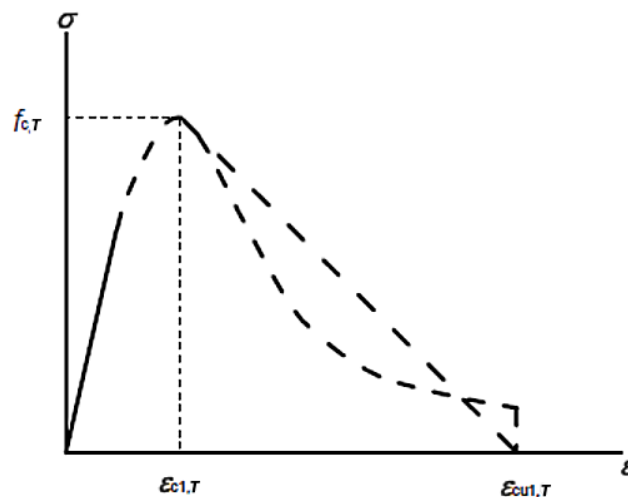
state tests and a combination of both. As creep effects are not explicitly considered, the material models in this Eurocode are applicable for heating rates between 2 and 50 K/min.

5.3.1 Mechanical Properties

5.3.1.1 Concrete under Compression

Usually, the performance of the material in compression is influenced by the chemical and physical changes of the cement paste and aggregates, as well as thermal incompatibility between them.

The deformation properties of uniaxially compressed concrete at a given temperatures shall be obtained from the stress-strain relationships. As recommended by Eurocode 2, Fig.5. 8 provides the stress-strain relationships that are defined by two parameters: (i) the compressive strength $f_{c,T}$, (ii) the strain $\epsilon_{c1,\theta}$ corresponding to $f_{c,T}$.



Range	Stress $\sigma(\tau)$
$\epsilon \leq \epsilon_{c1,T}$	$\frac{3 \epsilon f_{c,T}}{\epsilon_{c1,T} \left(2 + \left(\frac{\epsilon}{\epsilon_{c1,T}} \right)^3 \right)}$
$\epsilon_{c1,T} < \epsilon \leq \epsilon_{cu1,T}$	For numerical purposes a descending branch should be adopted. Linear or non-linear models are permitted.

Fig.5. 8 Mathematical model for stress-strain relationships of concrete under compression at elevated temperatures

The values suggested in EC2 are reported in Tab.5. 1 as a function of temperatures. For intermediate values of the temperature, linear interpolation can be used. Generally, the parameters can be used for normal weight concrete with siliceous aggregates or

calcareous aggregates, which containing at least 80% of calcareous aggregate by weight.

Concrete temperature	Siliceous aggregates			Calcareous aggregates		
	$T(^{\circ}C)$	$f_{c,T}/f_{ck}$	$\varepsilon_{cl,T}$	$\varepsilon_{cu1,T}$	$f_{c,T}/f_{ck}$	$\varepsilon_{cl,T}$
<i>1</i>	<i>2</i>	<i>3</i>	<i>4</i>	<i>5</i>	<i>6</i>	<i>7</i>
20	1	0.0025	0.02	1	0.0025	0.02
100	1	0.004	0.0225	1	0.004	0.0225
200	0.95	0.0055	0.025	0.97	0.0055	0.025
300	0.85	0.007	0.0275	0.91	0.007	0.0275
400	0.75	0.01	0.03	0.85	0.01	0.03
500	0.6	0.015	0.0325	0.74	0.015	0.0325
600	0.45	0.025	0.035	0.6	0.025	0.035
700	0.3	0.025	0.0375	0.43	0.025	0.0375
800	0.15	0.025	0.04	0.27	0.025	0.04
900	0.08	0.025	0.0425	0.15	0.025	0.0425
1000	0.04	0.025	0.045	0.06	0.025	0.045
1100	0.01	0.025	0.0475	0.02	0.025	0.0475
1200	0	-	-	0	-	-

Tab.5. 1 Values for the main parameters of the stress-strain relationships for normal weight concrete with siliceous or calcareous aggregates at elevated temperatures, according to **EN1991-1-2 (2004)**

Concrete stiffness can be evaluated by the initial tangent of the stress-strain relationship. According to Equation(5.1) which is suggested by Fig.5. 8

$$\sigma(T) = \frac{3\varepsilon f_{\varepsilon,T}}{\varepsilon_{cl,T} \left(2 + \left(\frac{\varepsilon}{\varepsilon_{cl,T}} \right)^3 \right)} \quad (5.1)$$

The tangent stiffness should be expressed as Equation(5.2)

$$E = \frac{3}{2} \cdot \frac{f_{c,T}}{\varepsilon_{cl,T}} \quad (5.2)$$

Attention must be paid to the fact that such stiffness takes implicitly into account two contributions of strain: instantaneous load-induced strain and transient thermal strain. (This is the reason why it is addressed as “stiffness” rather than “elastic modulus”)

By considering compressive strength equal to 60MPA, and considering the values corresponding to an average between siliceous and calcareous aggregates, the reduction of concrete stiffness can be evaluated according to Equation (5.2) and the result is given

by Tab.5. 2

Concrete stiffness decay		
$f_{c,T}/f_{ck}$	<i>Elastic modulus</i>	T
[-]	[MPA]	[°C]
1	36000	20
1	22500	100
0.96	15709	200
0.88	11314	300
0.8	7200	400
0.67	4020	500
0.525	1890	600
0.365	1314	700
0.21	756	800
0.115	414	900
0.05	180	1000
0.015	54	1100
0	0	1200

Tab.5. 2 Tangent stiffness as a function of temperature.

5.3.1.2 Concrete under Tension

A common design of concrete structure usually is based on the hypothesis that the tensile strength of concrete is negligible. However, in the present work it is necessary to take into account the tensile strength. According to EN 1992-1-2:2004 the strength can be defined as a function of temperature, by a reduction coefficient $k_{ck,t}$. Equation(5.3) gives the corresponding expression.

$$f_{ck,t}(T) = k_{ck,t}(T) f_{ck,t} \quad (5.3)$$

In absence of more accurate information, the value of $k_{ck,t}$ should be selected according to Equation(5.4) and Fig.5. 9

$$\begin{aligned} k_{c,t}(T) &= 1.0 && \text{for } 20^{\circ}\text{C} \leq T \leq 100^{\circ}\text{C} \\ k_{c,t}(T) &= 1.0 - 1.0(T - 100) / 500 && \text{for } 100^{\circ}\text{C} < T \leq 600^{\circ}\text{C} \end{aligned} \quad (5.4)$$

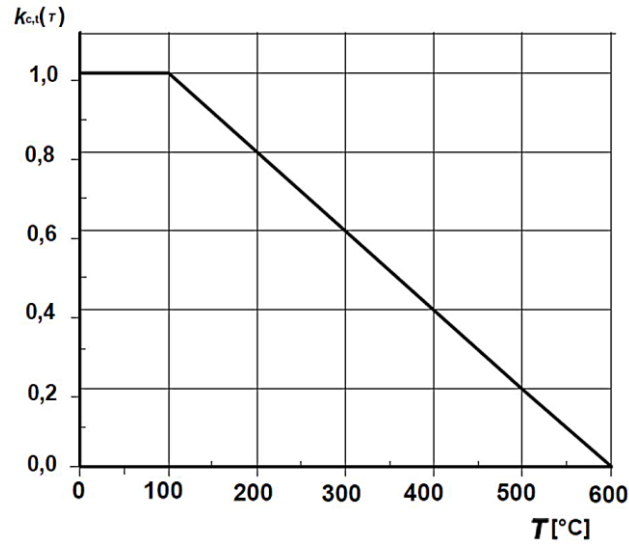


Fig.5. 9 Coefficient $k_{c,t}(T)$ allowing for decrease of tensile strength ($f_{ct,t}$) of concrete at elevated temperatures, EN 1992-1-2:2004

5.3.1.3 Thermal Elongation

EC2 gives the expression for the thermal strain $\varepsilon_c(T)$ for different aggregates:

Siliceous aggregates:

$$\begin{aligned} \varepsilon_c(T) &= -1.8 \times 10^{-4} + 9 \times 10^{-6} T + 2.3 \times 10^{-11} T^3 && \text{for } 20^\circ\text{C} \leq T \leq 700^\circ\text{C} \\ \varepsilon_c(T) &= 14 \times 10^{-3} && \text{for } 700^\circ\text{C} < T \leq 1200^\circ\text{C} \end{aligned} \quad (5.5)$$

Calcareous aggregates:

$$\begin{aligned} \varepsilon_c(T) &= -1.2 \times 10^{-4} + 6 \times 10^{-6} T + 1.4 \times 10^{-11} T^3 && \text{for } 20^\circ\text{C} \leq T \leq 805^\circ\text{C} \\ \varepsilon_c(T) &= 12 \times 10^{-3} && \text{for } 805^\circ\text{C} < T \leq 1200^\circ\text{C} \end{aligned} \quad (5.6)$$

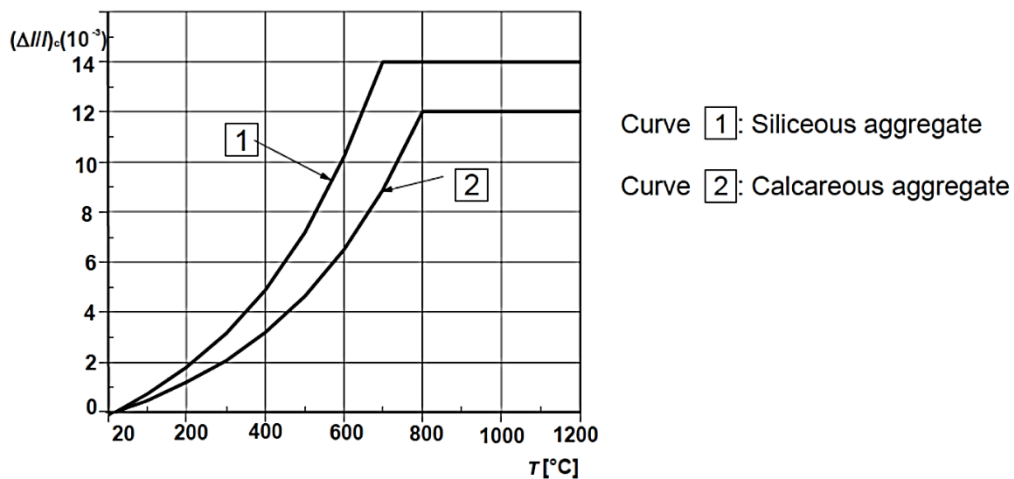


Fig.5. 10 Total thermal elongation of concrete at elevated temperatures, EN 1992-1-2:2004

The variation of the thermal elongation with temperatures is illustrated in Fig.5. 10. In the numerical simulations the average values of those corresponding to the two

aggregates. Tab.5. 3 gives the average elongation coefficient; for the intermediate value, linear interpolation can be used.

Concrete temperature	Siliceous aggregates	Calcareous aggregates	Average
T	$\varepsilon_c(T)$	$\varepsilon_c(T)$	
20	1.840E-07	1.120E-07	1.480E-07
100	7.430E-04	4.940E-04	6.185E-04
200	1.804E-03	1.192E-03	1.498E-03
300	3.141E-03	2.058E-03	2.600E-03
400	4.892E-03	3.176E-03	4.034E-03
500	7.195E-03	4.630E-03	5.913E-03
600	1.019E-02	6.504E-03	8.346E-03
700	1.401E-02	8.882E-03	1.145E-02
800	1.400E-02	1.200E-02	1.300E-02
900	1.400E-02	1.200E-02	1.300E-02
1000	1.400E-02	1.200E-02	1.300E-02
1100	1.400E-02	1.200E-02	1.300E-02
1200	1.400E-02	1.200E-02	1.300E-02

Tab.5. 3 Average thermal elongation of concrete

5.3.1.4 Coefficient of Thermal Expansion

As it is mentioned in Section 5.2.1, the present simulation is modeling in the 2D plane.

Expansion			
alpha11	alpha22	alpha33	Temperature[°C]
7.40E-09	0	0	20
6.19E-06	0	0	100
7.49E-06	0	0	200
8.67E-06	0	0	300
1.01E-05	0	0	400
1.18E-05	0	0	500
1.39E-05	0	0	600
1.64E-05	0	0	700
1.63E-05	0	0	800
1.44E-05	0	0	900
1.30E-05	0	0	1000
1.18E-05	0	0	1100
1.08E-05	0	0	1200

Tab.5. 4 Expansion of orthotropic material

In order to have strains and stress only in the direction parallel to the axis of the

concrete member, to define the material as isotropic is no more appropriate. Hence, a temperature dependent orthotropic material is used with the present work with thermal *Expansion coefficient* in a form that is given by Tab.5. 4.

5.3.1.5 Concrete Damage Plasticity

Name: Concrete
Description:

Material Behaviors

- Density
- Elastic
- Expansion
- Specific Heat
- Concrete Damaged Plasticity**

General Mechanical Thermal Electrical/Magnetic Other

Concrete Damaged Plasticity

Plasticity Compressive Behavior Tensile Behavior

Use temperature-dependent data

Number of field variables:

Data

	Dilation Angle	Eccentricity	f_{b0}/f_{c0}	K	Viscosity Parameter
1	30	0.1	1.16	0.66666667	0

Fig.5. 11 Parameters of Concrete damage plasticity

Once defined the parameters for the linear-elastic behavior and for compression and uniaxial tensile response, the model *Concrete Damaged Plasticity* requires the entry of the parameters required for defining the failure surface and the plastic potential.

The parameter f_{b0}/f_{c0} is the ratio between the resistance to biaxial and uniaxial compression;

K_c is the ratio of the second invariant of the stress on the traction meridian $q_{(TM)}$ and the second invariant of the stress on the compression meridian $q_{(CM)}$.

5.3.1.6 Tensile Behavior

The calculation model also requires the definition of the uniaxial tensile behavior of the material. The tensile behavior can be divided into two phases: (i) elastic phase up to the tensile strength, σ_{t0} ; (ii) post-limited phase which is also called as tension stiffening. The tensile resistance value at 20°C is implemented as $\sigma_{t0} = 4\text{MPa}$.

The model *Concrete Damaged Plasticity* considers a failure criterion according to Hilleborg (1976), in which the fracture energy GF is defined as the energy required to

propagate a tensile crack in the unit area; thus it appears to be a parameter of the material and allows to adequately describe the phenomenon Tension stiffening in concrete. With this approach, the tensile behavior of the material is expressed in terms of crack opening.

The fracture energy was evaluated by using the formula (Equation(5.7)) described by the CEB - FIP Model Code 90 (1993).

$$G_F = G_{F0} \left(f_{cm} / f_{cm0}^{0.7} \right) \quad (5.7)$$

Where,

f_{cm} : is average resistance to compression of the material, equal to 60 MPa,

f_{cm0} : is equal to 60 MPa,

G_{F0} : is the basic value of the fracture energy, depending on the maximum diameter of the aggregates used in the mix design.

The basic values of the fracture energy can be referred to Fig.5. 12.

d_{max} (mm)	G_{F0} (Nmm/mm ²)
8	0.025
16	0.030
32	0.058

Fig.5. 12 Basic value of G_{F0}

The maximum aggregate size is considered to be 16 mm; so that $G_F=0.115Nmm/mm^2$, according to Fig.5. 13.

Max. aggregate size d_{max} (mm)	G_F (Nm/m ²)							
	C12	C20	C30	C40	C50	C60	C70	C80
8	40	50	65	70	85	95	105	115
16	50	60	75	90	105	115	125	135
32	60	80	95	115	130	145	160	175

Fig.5. 13 Fracture Energy G_F

Then the fracture energy can be implemented as the plasticity property according to the software manual.

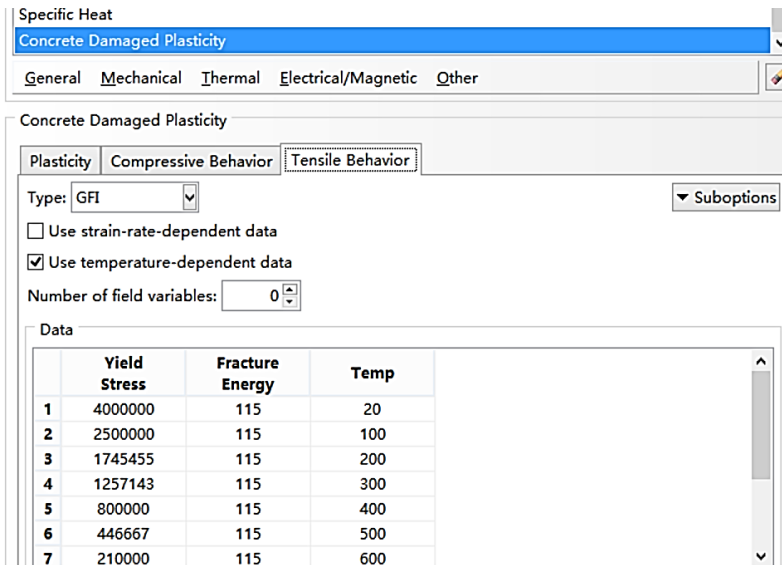


Fig.5. 14 Tensile Behavior determined by fracture energy in ABAQUS

5.3.2 Boundary Conditions

5.3.2.1 Boundary Constraint

Thermal loading according to the standard ISO 834 curve is implemented. As regards mechanical simulation, symmetry was enforced at one end of the beam. The vertical displacement was restrained in one point only (self-weight was not considered).

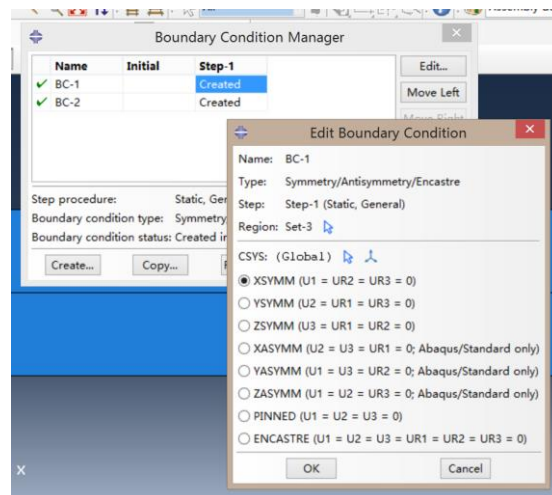


Fig.5. 15 Boundary condition to confirm translation

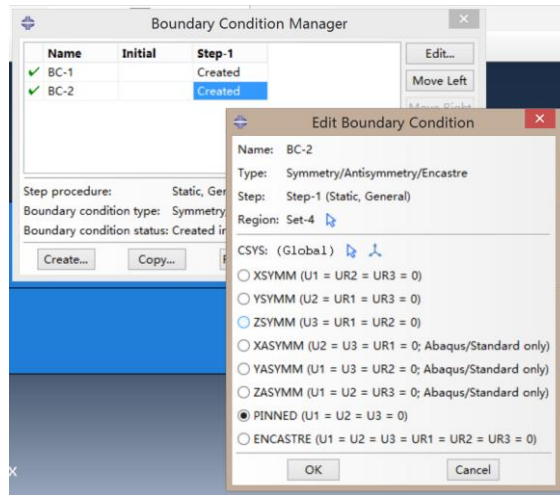


Fig.5. 16 Boundary condition to confirm symmetry

5.3.2.2 Loads

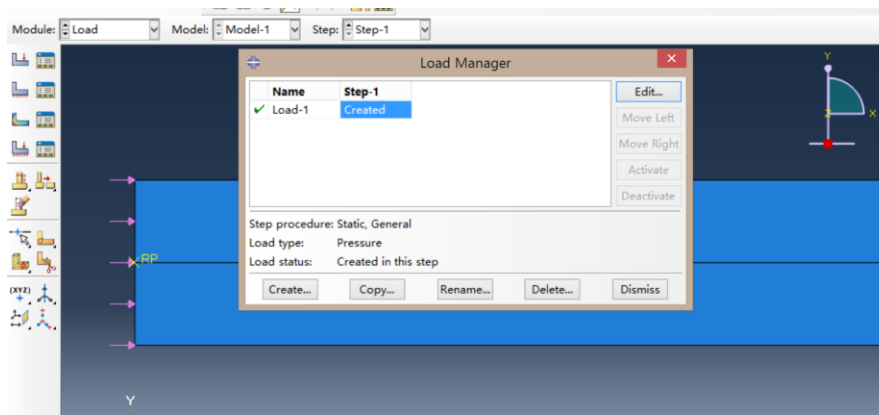


Fig.5. 17 External load

Pure compressive load leading to a uniform stress of 10 MPA was applied (Fig.5. 17). Moreover, before given the load, a constraint is set on the left section (where load is applied) so that the left boundary will respect the Navie-Bernoulli assumption (plane sections remain plane), Fig.5. 18).

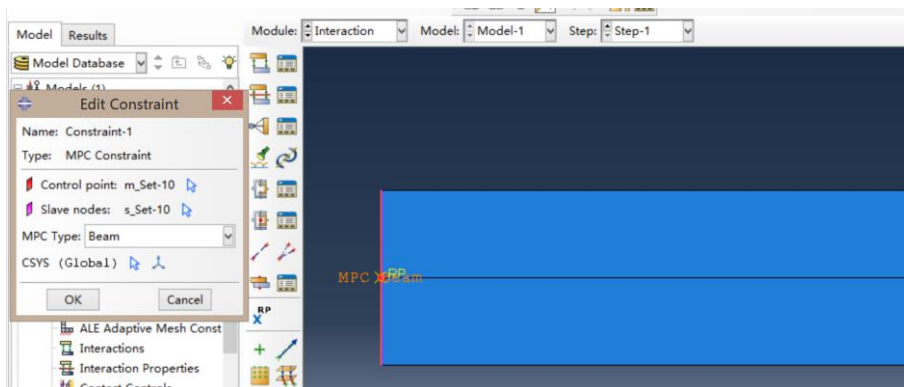


Fig.5. 18 Constraint in left boundary

5.3.2.3 Predefined Field

The resulting file from Section 5.2 describing the thermal field during heating should be implemented as predefined field (Fig.5. 19).

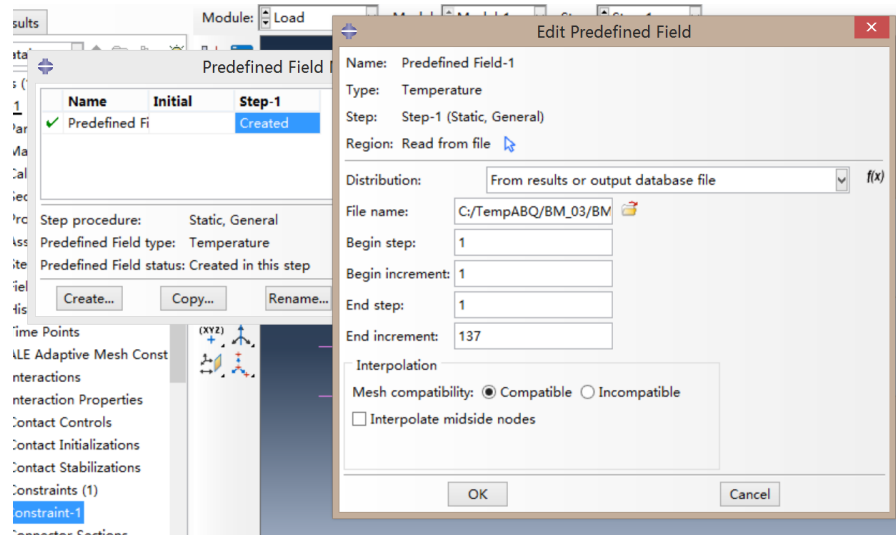


Fig.5. 19 Predefined field

5.3.3 Mesh and Element

The whole problem should be analyzed as Plane Stress Problem. Thus the type of elements has been defined as *Plane stress element*, which is referred as CPS4R in ABAQUS. In addition, the mesh size is 5x5 millimeters, which is inherited from the heat transfer simulation and confirmed is compatible with the thermal transfer result.

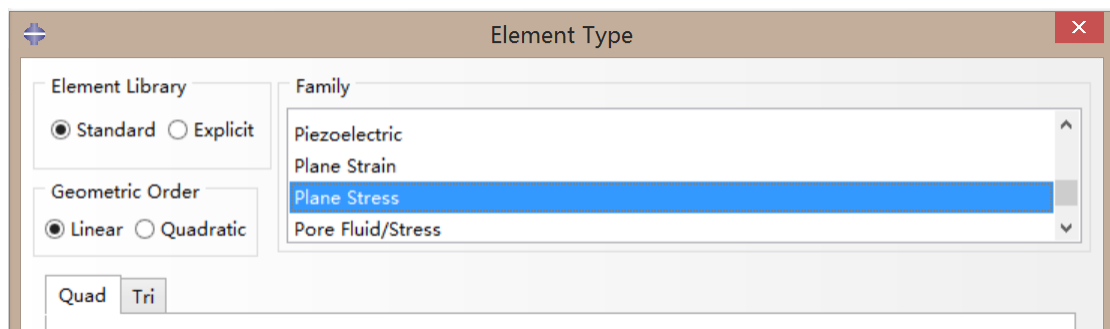


Fig.5. 20 Element type in mechanical performing

5.4 Benchmark result

By means of commercial software ABAQUS, a numerical simulation is performed. When the external load equals 10MPa, the tensile effect inside the specimen can be mostly compensated so that the tensile stress and strain are negligible.

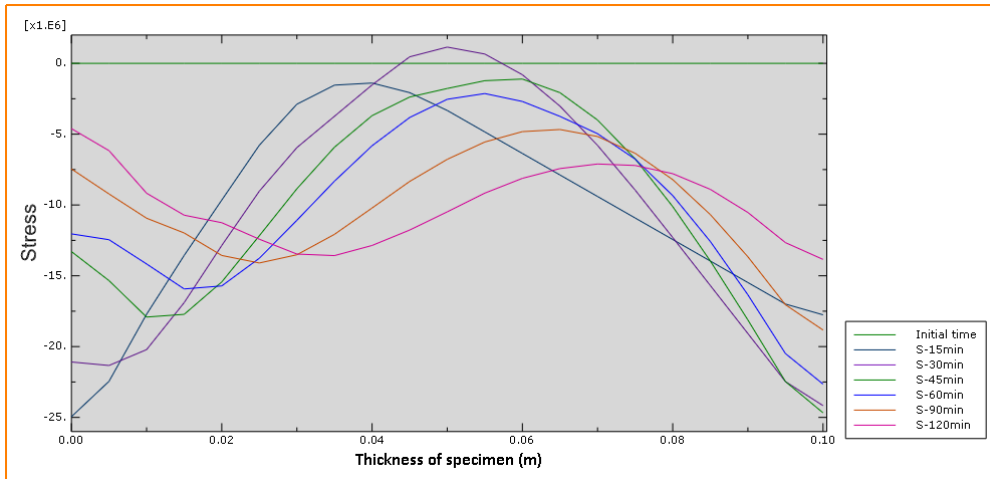


Fig.5. 21 Stress distribution along the thickness of the specimen at different time point, respectively, when external load is 10MPA

Fig.5. 21 gives the plotted of stress distribution along the thickness of the specimen at different fire durations. The present unit in the vertical axial is given Pascal.

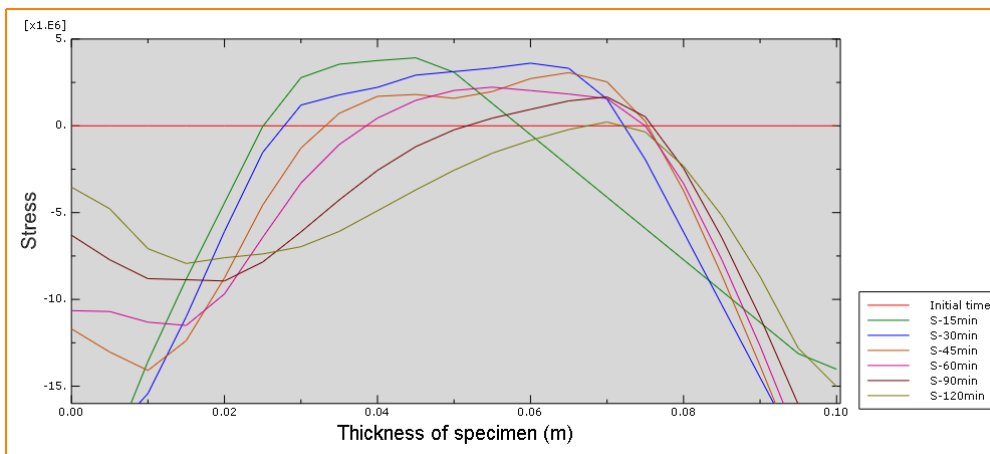


Fig.5. 22 Stress distribution along the thickness of the specimen at different time point, respectively, when external load is 5MPA

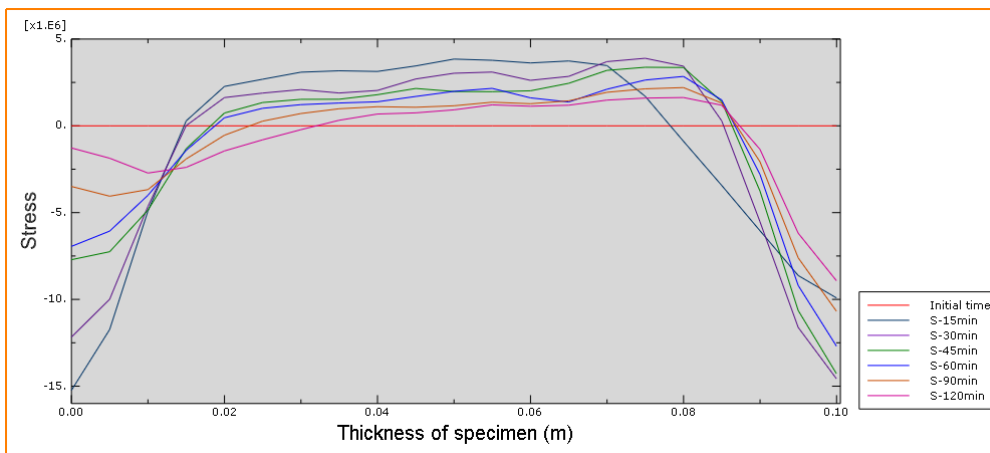


Fig.5. 23 Stress distribution along the thickness of the specimen at different time point, respectively, when external load is 0.5MPA

Other two level of external membrane compression were considered: (i) 5MPa, (ii)

0.5MPa. The former case leads to relevant tensile stresses not very severe, while the latter one (representing the case of zero external load) leads to severe cracking. It should be underlined that when the external load is reduced to less than 0.5MPa, to reach the convergence by ABAQUS is very time-consuming. The results of them are plotted in Fig.5. 22 and Fig.5. 23. The present unit in the vertical axial is given in PA.

The development of vertical displacement of specimens under different external compression loads is another meaningful benchmark for further applications. The development of the maximum vertical displacement (symmetry section) as a function of time for different external loads is plotted in Fig.5. 24.

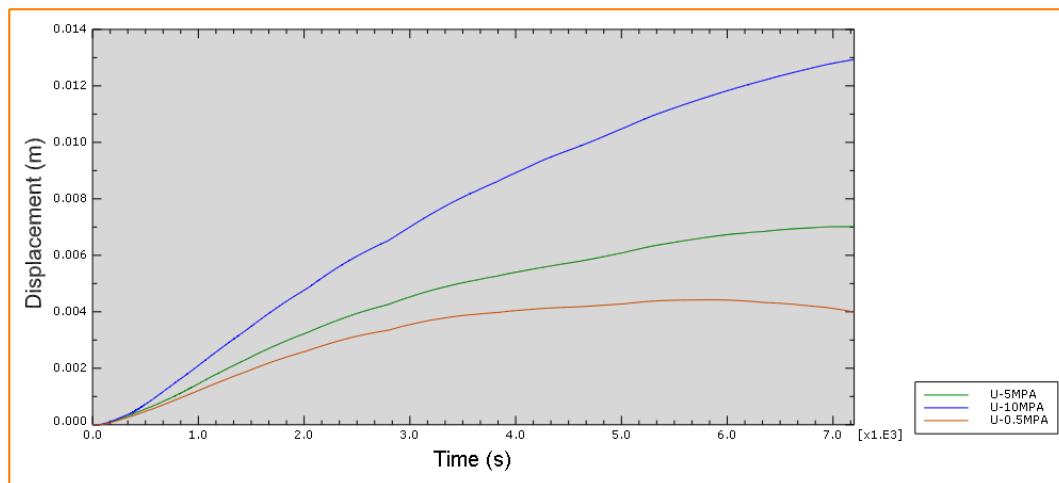


Fig.5. 24 Comparison of displacement distribution as function of time with different external loads, respectively

6. An algorithm for Cracking Behavior Study

As it is described in Section 2.6, concrete deformation in fire is usually described by assuming that the total strain ε consists of four components: the thermal strain, $\varepsilon_{th}(T)$; the instantaneous stress-related strain, $\varepsilon_{\sigma}(\sigma, T)$; the creep strain, $\varepsilon_{cr}(\sigma, T, t)$; and the transient strain, $\varepsilon_{tr}(\sigma, T)$. In this Chapter, an algorithm will be developed in MATLAB to evaluate the mechanical behavior of slabs and beams (where, the thermal problem in 1D).

6.1 Algorithm Principle

Equation(2.6) gives the expression of the total strain in concrete during heating:

$$\varepsilon = \varepsilon_{th}(T) + \varepsilon_{\sigma}(\sigma, T) + \varepsilon_{cr}(\sigma, T, t) + \varepsilon_{tr}(\sigma, T) \quad (6.1)$$

The latter three contributions of strain can be described as *mechanical stress*. Aware of this, it should be reasonable to express the total strain in another form which is given by Equation(6.2).

$$\varepsilon = \varepsilon_{th}(T) + \varepsilon_m(\sigma, T) \quad (6.2)$$

Recognized the mechanical stress as the elastic strain (assumption that can be made for monotonic loading, as the case), the expression of total strain can be changed into the form:

$$\varepsilon_{tot} = \varepsilon_{elastic} + \varepsilon_{th} \quad (6.3)$$

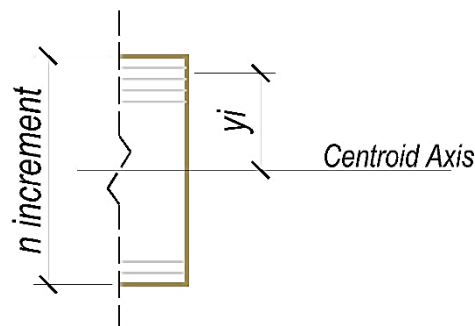


Fig.6. 1 Section and increment of the specimen

Fig.5. 1 shows the section of a beam/slab element. In the section, the temperature (hence, concrete stiffness) change with the depth along the thickness. Hence, the

thickness is divided in many layers, inside which temperature (and concrete stiffness) can be considered constant. The positive direction of y_i is same with the gravity and zero corresponds to the geometric centroid.

Considering the Navier-Bernoulli hypothesis, the total deformation of the section can be expressed via a linear function as reported in Equation(6.4).

$$\varepsilon_{tot} = \varepsilon_0 + \chi y_i \quad (6.4)$$

Where,

ε_0 : is the elongation of centroid,

χ : is the curvature of the section,

y_i : is the coordinate with respect to the geometric centroid.

Then, the elastic strain can be computed by Equation(6.5).

$$\varepsilon_{elastic} = \varepsilon_0 + \chi y - \varepsilon_{th} \quad (6.5)$$

The axial force N and moment M are described by Equation(6.6) and Equation(6.7), respectively

$$N = \int_{-\frac{h}{2}}^{\frac{h}{2}} \sigma_{el} \cdot b dy = b \cdot \int_{-\frac{h}{2}}^{\frac{h}{2}} E \cdot \varepsilon_{el} dy = b \cdot \int_{-\frac{h}{2}}^{\frac{h}{2}} E \cdot (\varepsilon_0 + \chi y - \varepsilon_{th}) dy \quad (6.6)$$

$$M = \int_{-\frac{h}{2}}^{\frac{h}{2}} \sigma_{el} \cdot b \cdot y dy = b \cdot \int_{-\frac{h}{2}}^{\frac{h}{2}} E \cdot \varepsilon_{el} \cdot y dy = b \cdot \int_{-\frac{h}{2}}^{\frac{h}{2}} E \cdot (\varepsilon_0 + \chi y - \varepsilon_{th}) y dy \quad (6.7)$$

Where,

h : is the thickness of the section

The two equations can be rewritten as follow:

$$\frac{N}{b} = \varepsilon_0 \int_{-\frac{h}{2}}^{\frac{h}{2}} E dy + \chi \int_{-\frac{h}{2}}^{\frac{h}{2}} E y dy - \int_{-\frac{h}{2}}^{\frac{h}{2}} E \cdot \varepsilon_{th} dy \quad (6.8)$$

$$\frac{M}{b} = \varepsilon_0 \int_{-\frac{h}{2}}^{\frac{h}{2}} E y dy + \chi \int_{-\frac{h}{2}}^{\frac{h}{2}} E y^2 dy - \int_{-\frac{h}{2}}^{\frac{h}{2}} E \cdot \varepsilon_{th} y dy \quad (6.9)$$

The following parameters can be defined:

$$\tilde{E} = \frac{\int_{-\frac{h}{2}}^{\frac{h}{2}} E dy}{h} ; \tilde{S} = \frac{\int_{-\frac{h}{2}}^{\frac{h}{2}} E y dy}{h} ; \tilde{I} = \frac{\int_{-\frac{h}{2}}^{\frac{h}{2}} E y^2 dy}{h}$$

$$\text{And } \tilde{\sigma}_{th} = \frac{\int_{-\frac{h}{2}}^{\frac{h}{2}} E \cdot \varepsilon_{th} dy}{h} ; \tilde{m}_{th} = \frac{\int_{-\frac{h}{2}}^{\frac{h}{2}} E \cdot \varepsilon_{th} y dy}{h}$$

Then, Equation(6.8) and Equation(6.9) can be described according to the following relation:

$$\frac{N}{bh} = \sigma_0 = \varepsilon_0 \cdot \tilde{E} + \chi \cdot \tilde{S} - \tilde{\sigma}_{th} \Rightarrow \varepsilon_0 \cdot \tilde{E} + \chi \cdot \tilde{S} = \tilde{\sigma}_{th} + \sigma_0$$

$$\frac{M}{bh} = \tilde{m}_0 = \sigma_0 \cdot e = \varepsilon_0 \cdot \tilde{S} + \chi \cdot \tilde{I} - \tilde{\sigma}_{th} y \Rightarrow \varepsilon_0 \cdot \tilde{S} + \chi \cdot \tilde{I} = \tilde{m}_{th} + \tilde{m}_0$$

And in metrical form, Equation(6.10):

$$\begin{pmatrix} \varepsilon_0 \\ \chi \end{pmatrix} = \begin{bmatrix} \tilde{E} & \tilde{S} \\ \tilde{S} & \tilde{I} \end{bmatrix}^{-1} \begin{bmatrix} \tilde{\sigma}_{th} & \sigma_0 \\ \tilde{m}_{th} & \tilde{m}_0 \end{bmatrix} \quad (6.10)$$

If the thermal profile and initial stress σ_0 are known, for a given section (geometry is known), the elongation and curvature can be evaluated by solving a linear problem.

6.2 Software Developed by MATLAB

6.2.1 Data resource

To verify the accuracy of the algorithm, it should be reasonable to start with a total compression condition since the tensile behavior introduces some uncertainties. So at the beginning the *external load* is 10MPa. As abovementioned, the elongation and curvature due to the combination effects of external load and thermal effect can be evaluated, and, therefore the stress distribution in the thickness:

$$\sigma = E \cdot (\varepsilon_0 + \chi y - \varepsilon_{th}) \quad (6.11)$$

The thickness of each increment (layer) is 5 millimeter, equal to the mesh size in ABAQUS; the total number of increment is equal to 20.

6.2.2 Functions

Several scripts have been written in Matlab.

E_Yg.m is a function for obtaining material properties. It could evaluate material Tangent Elastic Modulus and Expansion Coefficient.

In the function, the material tangent elastic modulus is obtained according to Tab.5. 2.

Considering compression negative and tension positive, the constitutive law can be expressed by Fig.6. 2.

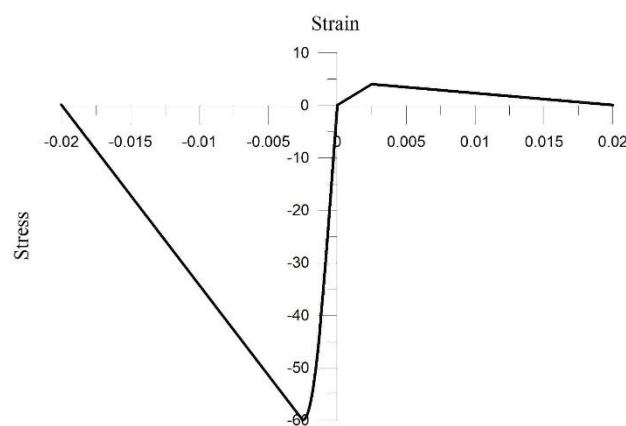


Fig.6. 2 Constitutive law of concrete.

E_YgT.m is a function to describe the constitutive law in the post-peak branch in tension (Tension Stiffening). After a first iteration in which the material is considered elastic, the stress profile is worked out. Where cracking occurs, the stress overcomes the tensile strength. In such layers, the new stresses is evaluated, by using the constitutive law in tension at the proper temperature of the layer, for the mechanical strain just evaluated. Once known the “new” stresses, by dividing it by the strain, the secant modulus is evaluated. With such modulus the linear system is solved again in order to work out the new curvature and mean elongation. With these new values, the strain profile and the stress profile are calculated. This iterative procedure goes on up to convergence is achieved. Convergence is evaluated in terms of elastic modulus between two following steps. When tensile stress occurs, this function will be called.

Fig.6. 3 and Fig.6. 4 give the plots of constitutive laws in compression s and in tension stress. The post-peak branches are both described by linear interpolation.

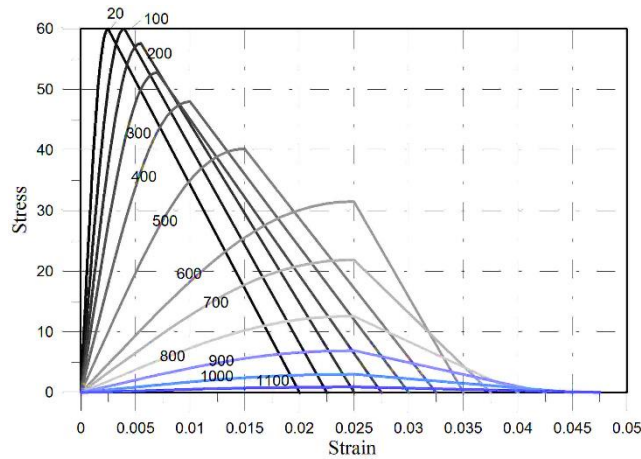


Fig.6. 3 Constitutive law for compression.

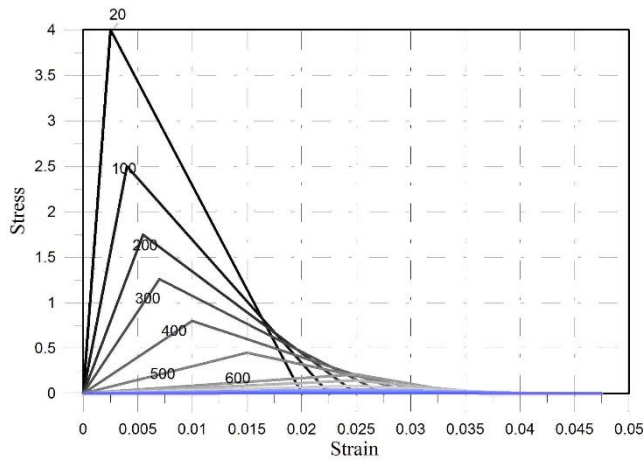


Fig.6. 4 Constitutive law for tension.

The unit of stress is MPA and the small size label on the plots represent the thermal profile and the unit is [°C].

CPT_IP.m is a function for evaluating the elongation, curvature, and stress distribution on the studied section, according to given section geometries, material properties, and thermal profiles.

6.2.3 Main script: Software-A

Generally, the main script is developed as *Software-A* based on the algorithm discussed in Section 6.1. The inputs are the thermal file and the material properties, while the outputs are stress distribution, vertical displacements, and effective elastic modulus distributions in the thickness. The software can significantly reduce the time consuming during numerical simulation, compare with the ABAQUS software.

The main script of the *Software-A* will be added in the appendix.

6.3 Result and Comparison

6.3.1 Compressive Condition

The comparison between the result obtained with ABAQUS and Matlab – Software A is shown in Fig.6. 5 for the external load equal to 10 MPA. The script gives almost the same results of ABAQUS.

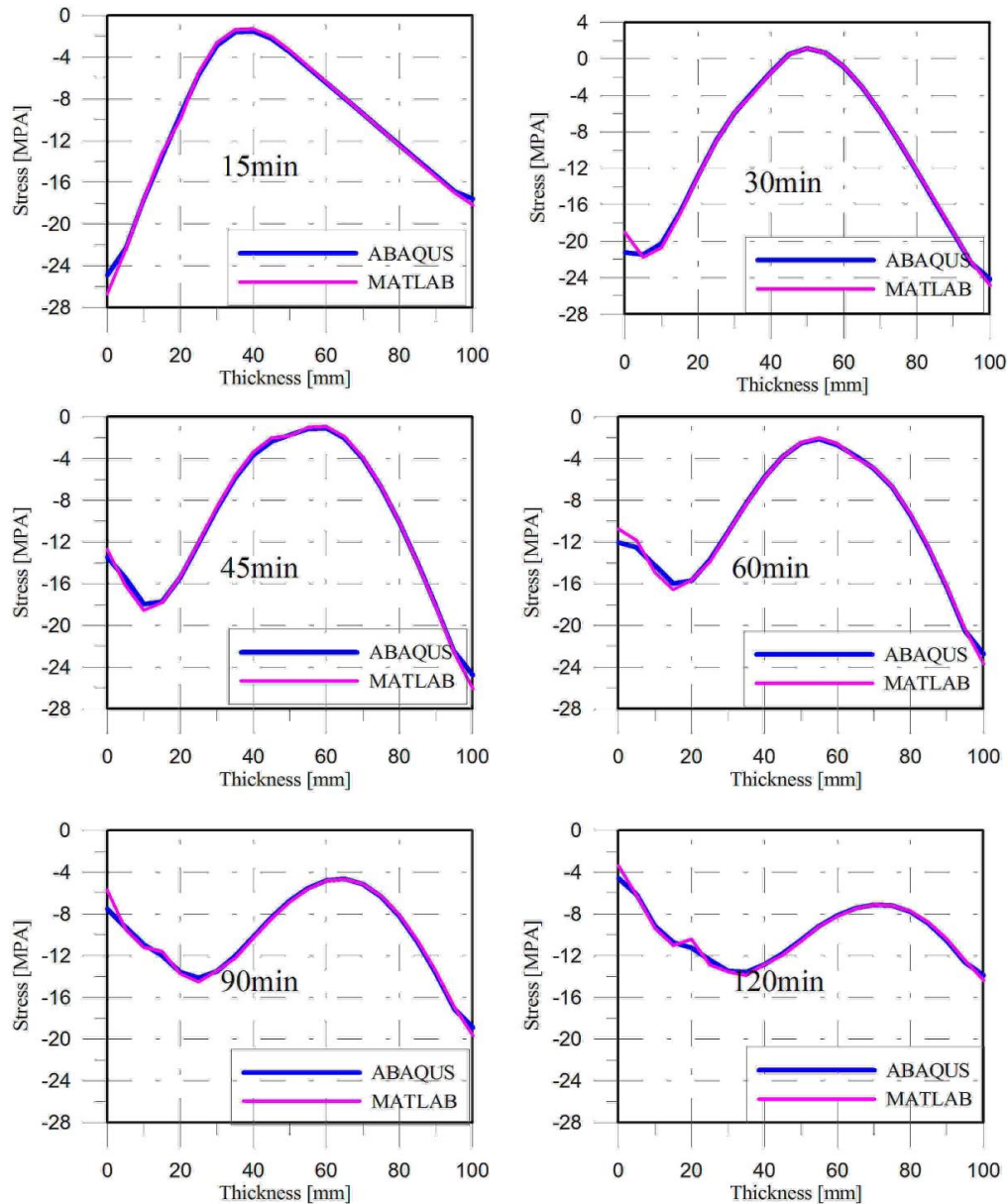


Fig.6. 5 Stress distribution comparison between two methods along the thickness during 120min, with external load equal to 10MPA.

It could be inferred that the algorithm results and the software results matched very well when the tensile limits had not been reached.

The script is also designed to give the output of the effective Elastic modulus at each

fire duration since it shows where cracking occurs (Fig.6. 6).

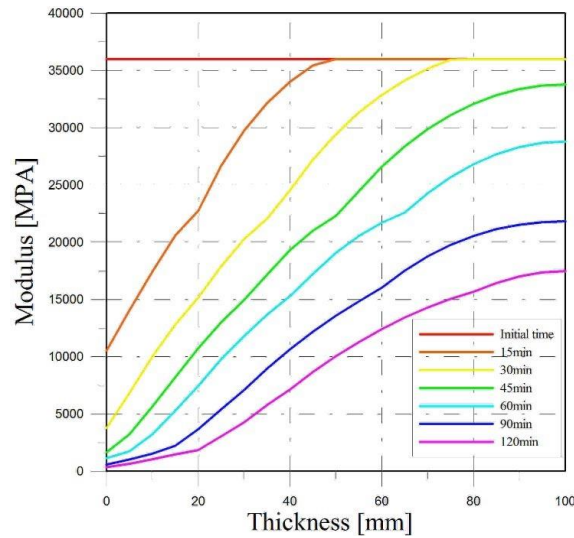


Fig.6. 6Elastic modulus distribution along the thickness during 120min, with external load equal to 10MPa.

The displacement variation with time is simply evaluated once the curvature is known (curvature is constant along the axis). The result from MATLAB and the result from ABAQUS are plotted in Fig.6.8.

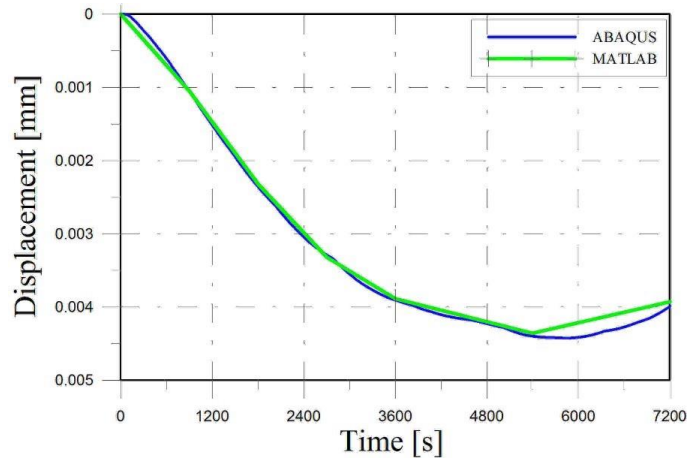


Fig.6. 7 Displacement development during a fire for an external load of 10MPa.

6.3.2 Tensile Condition

In this section, the external load will be reduced or even removed so as to observe the behaviors when cracking occurs.

Fig.6. 8 gives the stress distribution when the external load is equal to 5MPa. The tensile effects appears evidently on the stress distribution. Due to tension, cracking takes place and leads to secant elastic modulus decay with the following stress re-distribution along the section.

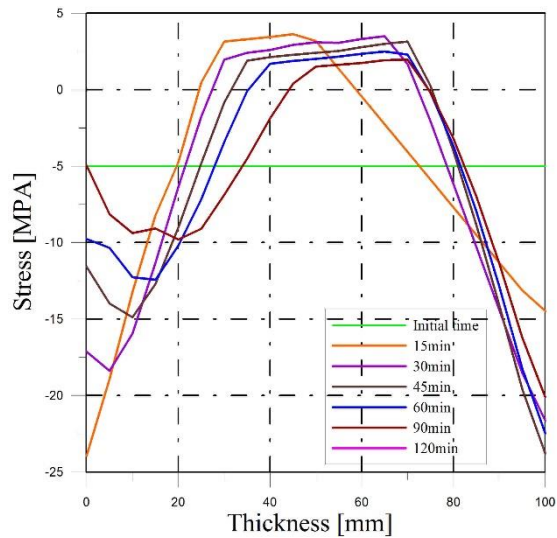


Fig.6. 8 Stress distribution along the thickness during 120min, with external load equal to 5MPA. Analysis via Matlab – Software A

The variation of elastic modulus under tension is evaluated by implementing *Fracture Energy*, about which it will be given a discussion in detail in the following chapter.

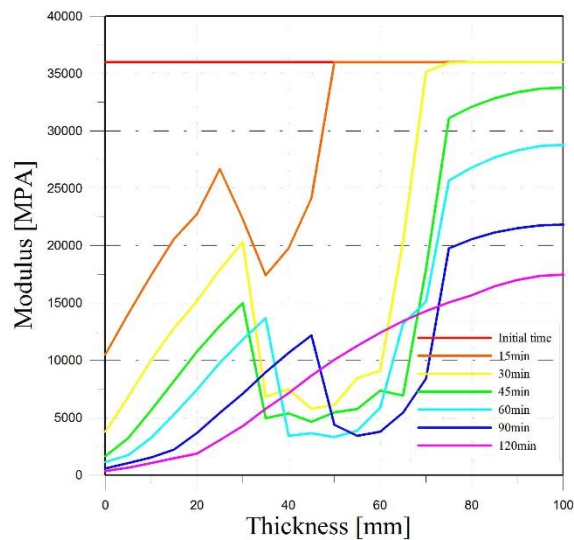


Fig.6. 9 Elastic modulus distribution along the thickness during 120min, with external load equal to 5MPA.

It can be observed in Fig.6. 9 that the elastic modulus is evidently lower compared with the compression condition..

Comparing the result with the ABAQUS product, it shows that under this condition, when external load equals 5 MPA (which means significant tensile stresses) the script still shows good consistency with the commercial software. It still outputs nearly the same result of ABAQUS as shown in Fig.6. 10.

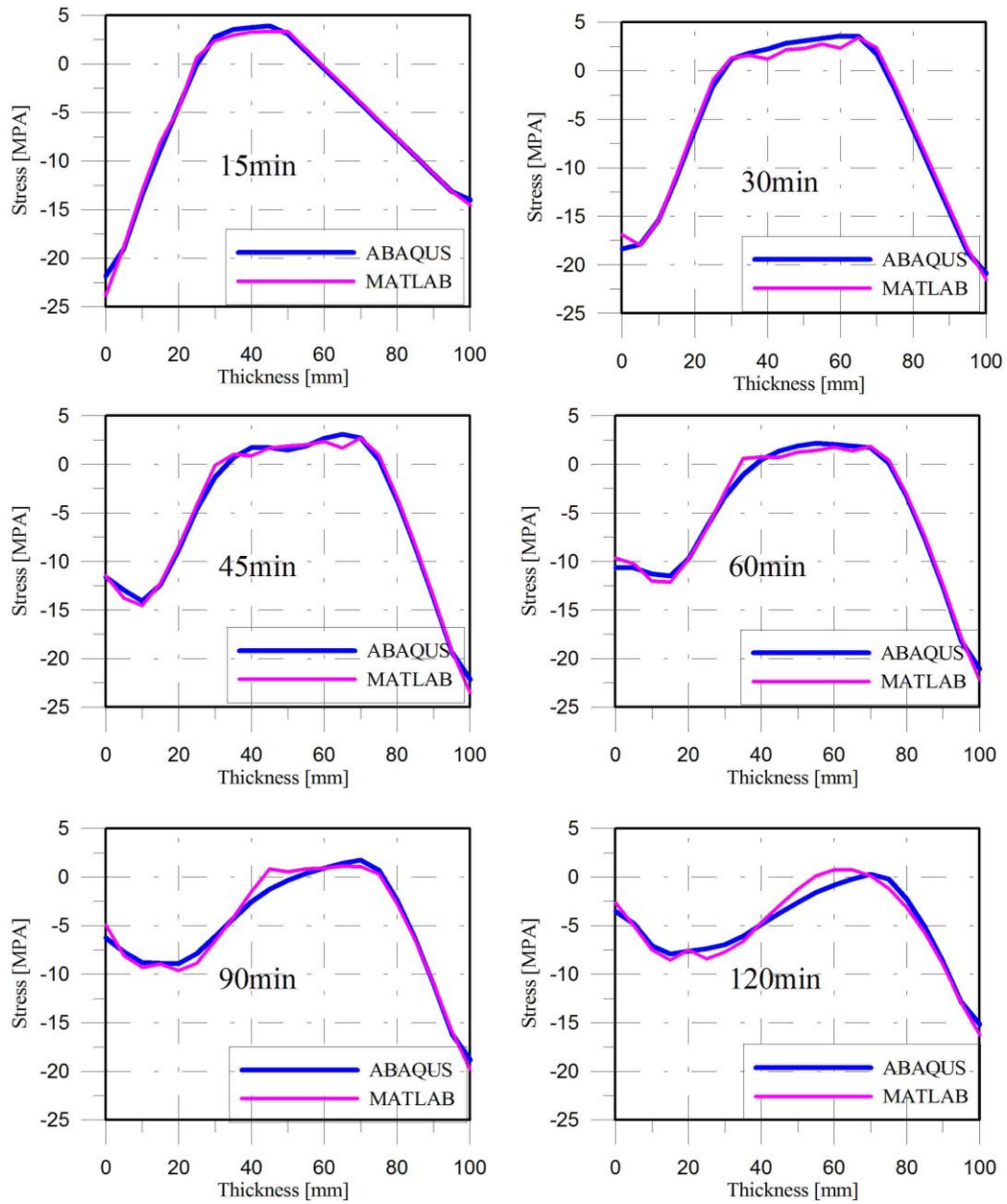


Fig.6. 10 Stress distribution comparison along the thickness during 120min, with external load equal to 5MPA.

In this case, displacement variation with time shows a slight difference between ABAQUS and Matlab simulation. The mismatching begin when significant tension takes place.

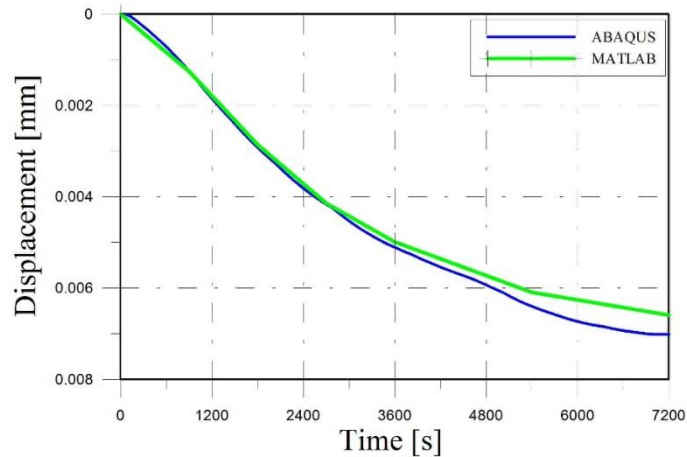


Fig.6. 11 Displacement development according to ABAQUS and MATLAB for the external load of 5MPA.

It has been mentioned in Chapter 5 that, due to the time consuming and complexity of ABAQUS modelling, 0.5 MPA external load was selected instead of zero-external load in order to get the most severe tensile condition result. MATLAB simulation will follow the same idea.

The results are obtained and given in the following graphs.

Fig.6. 12 shows stress distribution with external load equals to 0.5 MPA. In this case, tensile stress became the largest component and formed a very rough plateau (where cracking occurs). The comparison reported in Fig.6. 13 shows that the MATLAB output is even rougher than the ABAQUS output, but the agreement is still more than satisfactory.

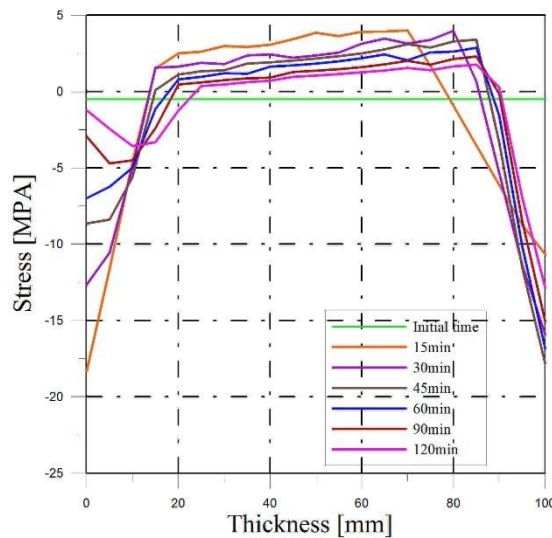


Fig.6. 12 Stress distribution along the thickness during 120min, with external load equals to 0.5MPA,.

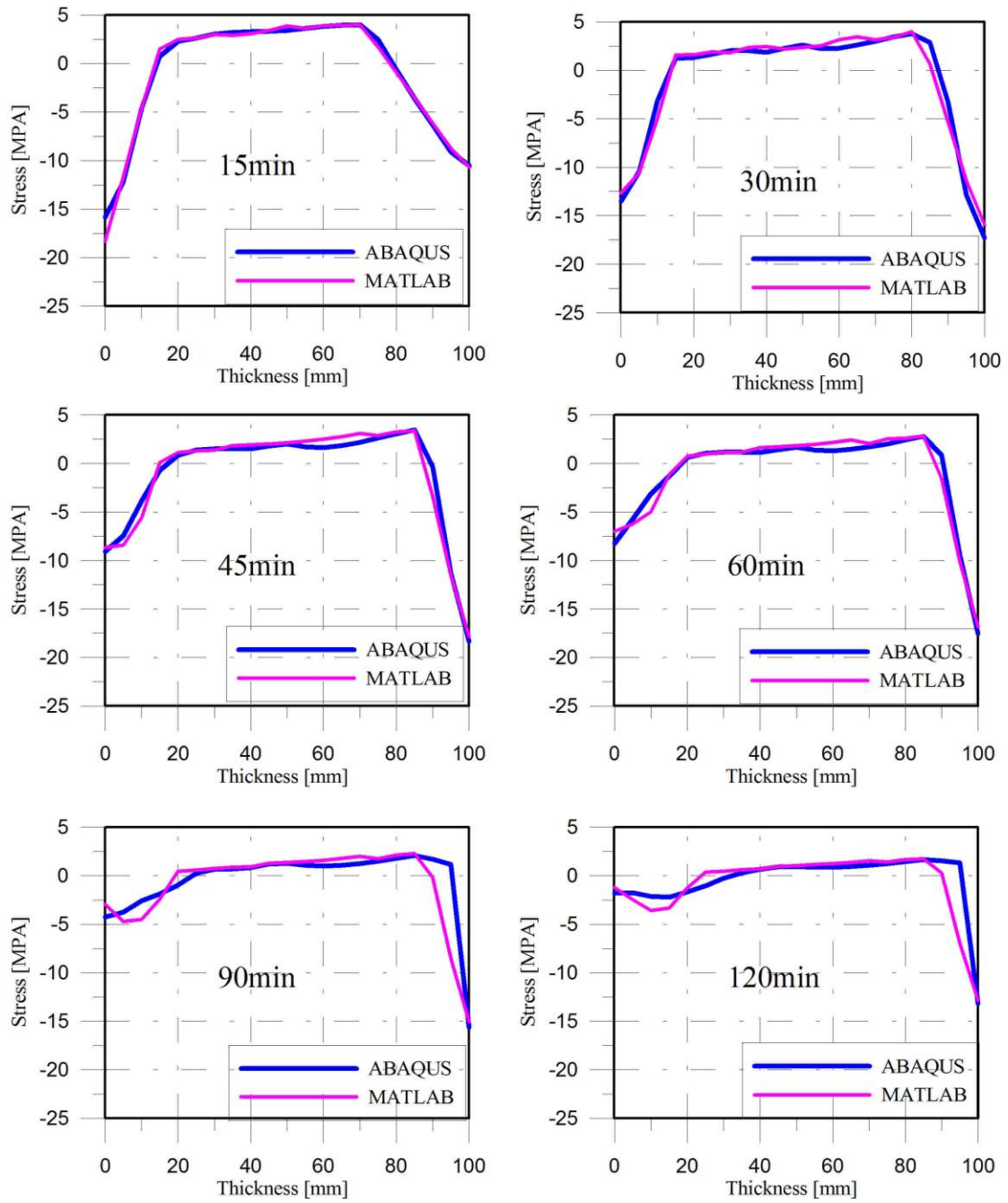


Fig.6. 13 Stress distribution comparison between two methods along the thickness during 120min, with external load equal to 0.5MPa.

The secant elastic modulus distribution is shown in in Fig.6. 14. The displacement is plotted in Fig.6. 15. This time the distance between two lines is a little bit higher.

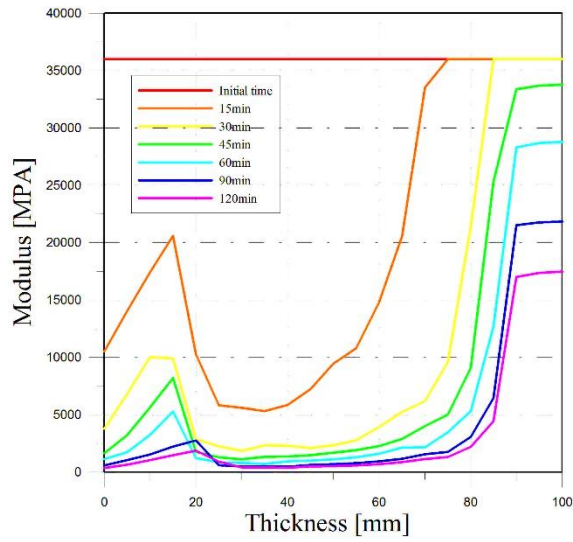


Fig.6. 14 Elastic modulus distribution along the thickness during 120min, with external load equal to 0.5MPa.

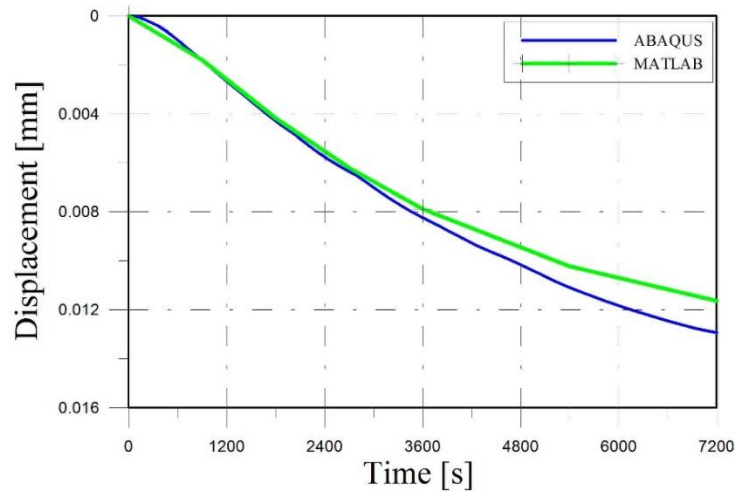


Fig.6. 15 Displacement development according to ABAQUS and MATLAB for the external load of 0.5MPa.

7. A Discussion of Fracture Energy Implementation

When studying post-failure behavior, concrete damage plasticity is introduced, so so to model tension stiffening and the strain-softening in compression. Tension stiffening is required in concrete smeared cracking model and specified by means of a post-failure stress-strain relation or by defining a fracture energy cracking criterion.

According to *CEB-FIP - Model Code 1990*, the *Fracture Energy (GFI)* is given as the energy required to propagate a tensile crack into a unit area. A critical parameter is the characteristic length.

7.1 Fracture Energy

According to *ABAQUS User guide, vol. 3*, specification of strain softening behavior in reinforced concrete generally means specifying the post-failure stress as a function of strain across the crack. Without reinforcements, this specification often introduces mesh sensitivity in the analysis results in the sense that results do not converge to a unique solution as the mesh is refined, because mesh refinement leads to narrower crack bands. This problem typically occurs if only a few discrete cracks form in the structure, and mesh refinement does not result in formation of additional cracks. If cracks are evenly distributed, mesh sensitivity is less of a concern.

As discussed earlier, when there is no reinforcement in significant regions of a concrete model, the strain softening approach for defining tension stiffening may introduce *unreasonable* mesh sensitivity.

Hillerborg's (1976) proposal which is mentioned in *Chapter 4* is adequate to limit such problem for many practical purposes. Hillerborg defines the energy required to open a unit area of crack as a material parameter, using brittle fracture concepts.

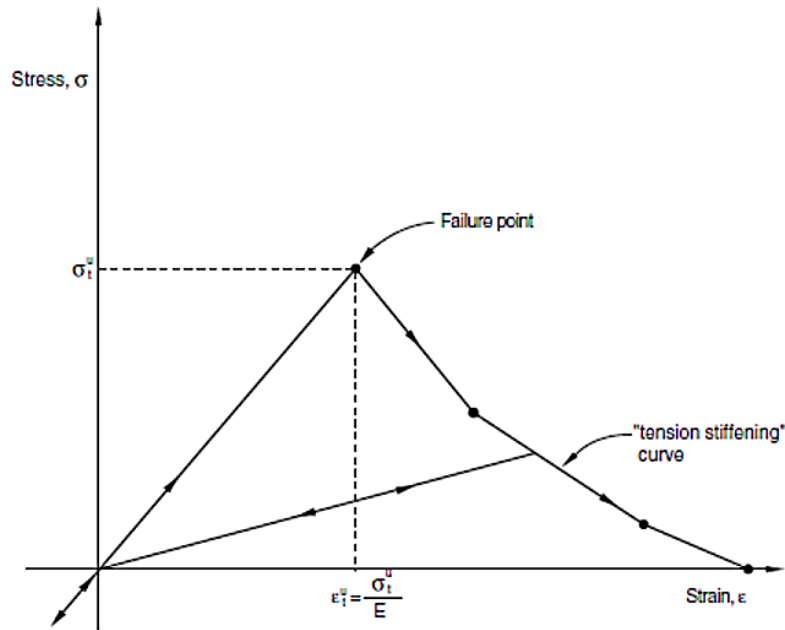


Fig.7. 1 “Tension stiffening” model, ABAQUS User guide, vol. 3.

With this approach the concrete’s brittle behavior is characterized by a stress-displacement response rather than a stress-strain response. Under tension a concrete specimen will crack across some section. After it has been pulled apart sufficiently and most of the stress has been removed (so that the elastic strain is small), its length will be determined primarily by the opening of the crack. The opening does not depend on the specimen length.

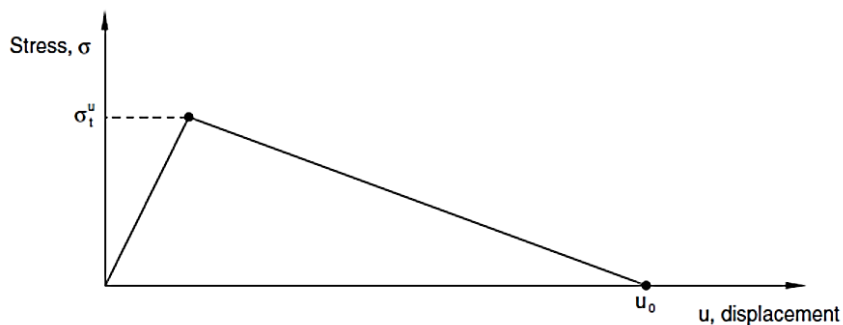


Fig.7. 2 Fracture energy cracking model, ABAQUS User guide, vol. 3.

The implementation of this stress-displacement concept in a finite element model requires the definition of a characteristic length associated with an integration point. The characteristic crack length is based on the element geometry and formulation: it is a typical length of a line across an element for a first-order element. For beams and trusses it is a characteristic length along the element axis. This definition of the characteristic

crack length is used, since the direction in which cracks will occur is not known in advance. Therefore, elements with large aspect ratios will have rather different behavior depending on the direction in which they crack: some mesh sensitivity remains because of this effect, and elements that are *as close to square as possible* are recommended.

This approach to modeling the concrete brittle response requires the specification of the displacement at which a linear approximation to the post-failure strain softening gives zero stress (Fig.7. 2).

The failure stress occurs at a failure strain which is defined by the failure stress divided by the Young's modulus. The implication is that a loaded specimen can remain in static equilibrium after failure only if the specimen is short enough so that the strain at failure is less than the value of the displacement.

$$\varepsilon_i^u < \frac{u_0}{L} \quad (7.1)$$

Where:

ε_i^u : is the strain at failure,

u_0 : is the specified displacement,

L : is the length of specimen.

7.2 Cracking Criterion Implementation

7.2.1 Displacement Implementation

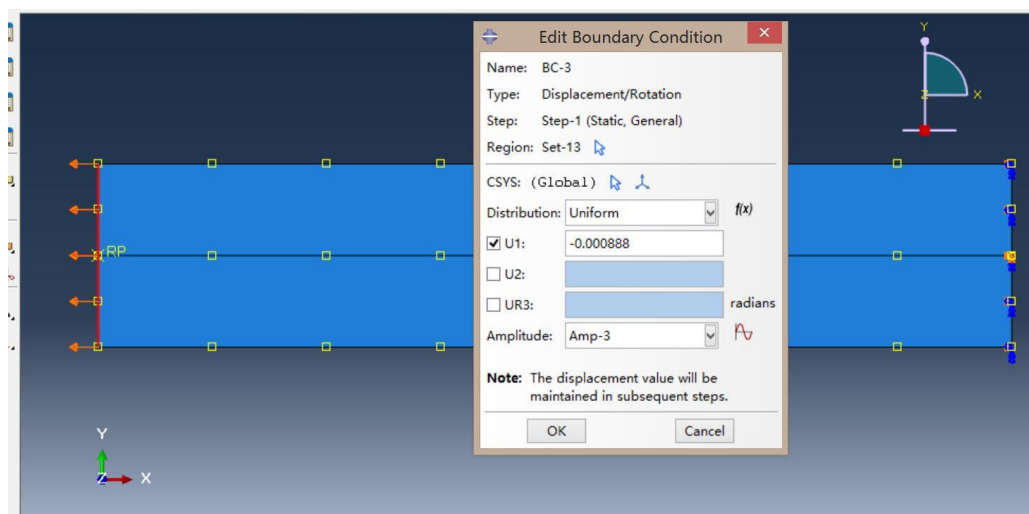


Fig.7. 3 Displacement implementation.

In order to get a direct relation between strain and stress, a numerical simulation in ABAQUS is performed by enforcing a time-dependent displacement to the specimen.

Applying the same geometry and properties given in *Chapter 6*, external load is applied by a time-dependent displacement with the maximum value equal to the one correspond to the ultimate strain condition (no thermal load is introduced).

The variation of displacement can be evaluated according to the constitutive law which has been provided in the earlier chapters.

7.2.2 Fracture Energy Implementation in MATLAB

One purpose of the chapter is to have clear acknowledge of characteristic length. When the simulation of MATLAB is performed, it has to start with reasonable assumption of characteristic length.

In the MATLAB codes, the fracture energy was implemented with characteristic length equal to 7.5 centimeters, which is the observing distance between two cracks according to the ABAQUS output (Fig.7. 4).

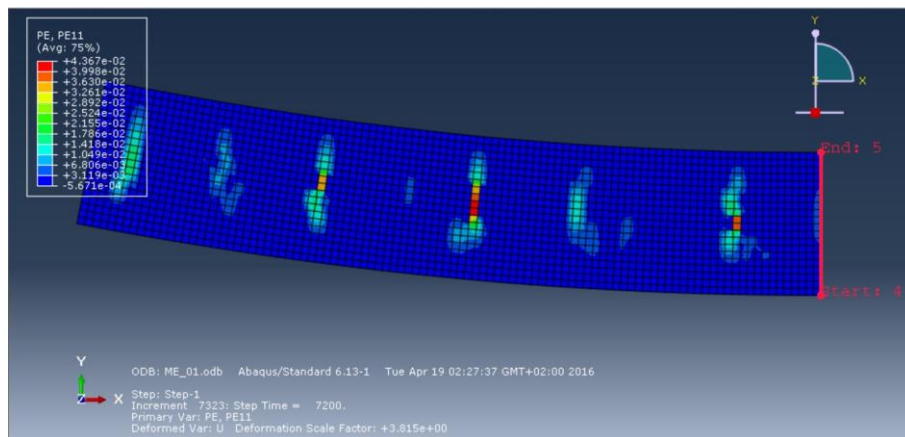


Fig.7. 4 Cracklings after 2 hours performance and selected Section-1.

Fig.7. 5 shows the constitutive law which has been implemented in MATLAB according to *fracture energy cracking criterion (GFI)*. In the following chapter, a comparison will be made between the MATLAB result and the one that is obtained from ABAQUS.

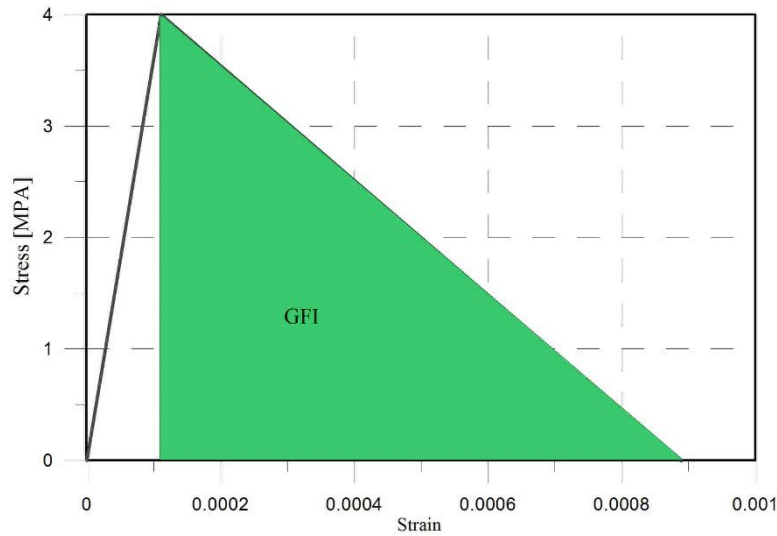


Fig.7. 5 Constitutive law in tensile branch (MATLAB)

7.2.3 Characteristic Length

In previous chapters, several functions have been developed. Among them, the function *E_YgT.m* (Section 6.2.2) was written with the purpose to implement the secant modulus in tension. It follows the constitutive law and uses *fracture energy cracking criterion*. To use the method, it is very important to make clear how ABAQUS software selects characteristic length.

In this section, 4 cases have been carried out and discussed so as to make clear of the determination of characteristic length in ABAQUS..

CASE 1

Case 1 selected characteristic length in MATLAB as 75mm, while the mesh size in ABAQUS is 5mm. The plot of the result in the same chart is given in Fig.7. 6

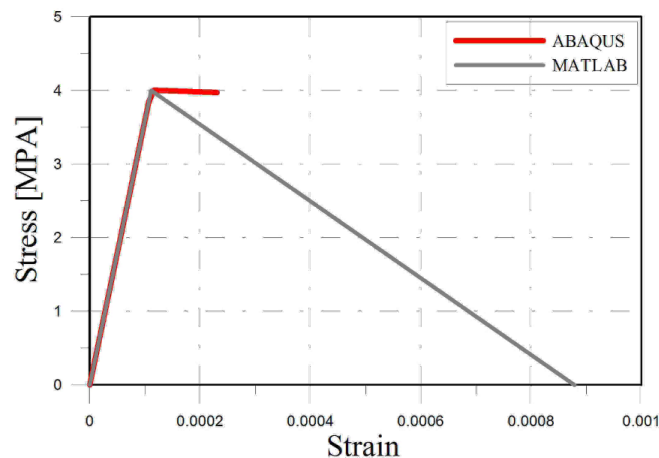


Fig.7. 6 Displacement controlled tensile behavior (Case 1)

It is evidently shown by Fig.7. 6 that the result from the two methods are not in

agreement.

By observing the graph in Fig.7. 6, it is reasonable to try to increase the slope of the non-elastic branch of the constitutive law so that the MATLAB results may simulate the ABAQUS better.

CASE 2

Using *Fracture Energy Cracking Criterion*, using 50 millimeters for both mesh size and characteristic length. Name this case as *Case 2* and the plot is given in Fig.7. 7

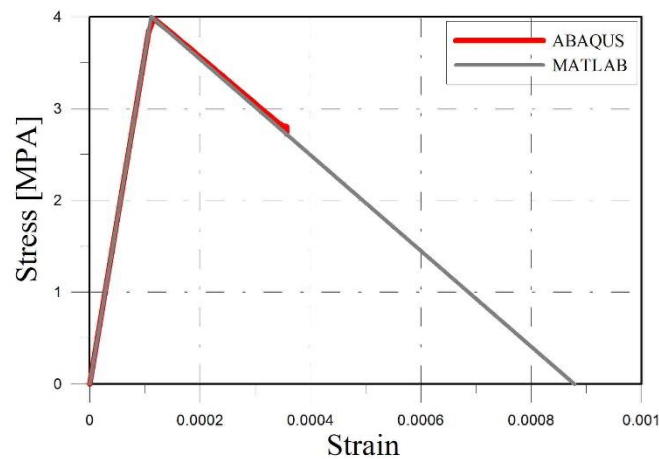


Fig.7. 7Fracture Energy Cracking Criterion (Case 2)

CASE3

MATLAB characteristic length = ABAQUS mesh size = 5 millimeter.

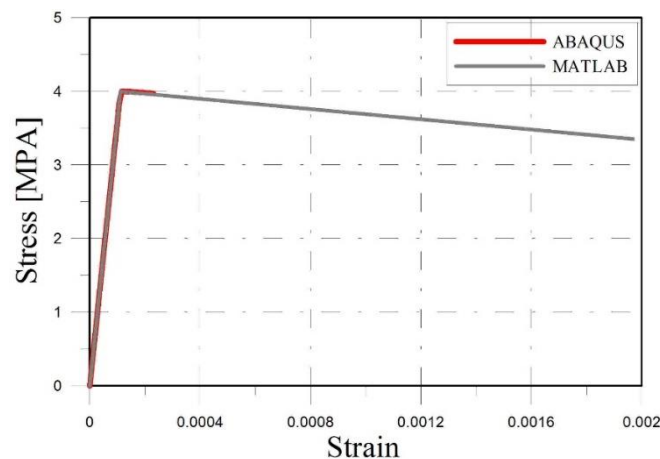


Fig.7. 8Fracture Energy Cracking Criterion (Case 3)

The result shows an unambiguous fact that when the ABAQUS software implement the fracture energy, it used the element mesh size as the characteristic length.

CASE 4:

In this case, the ABAQUS mesh size is chosen as 25 millimeter, as well as the

MATLAB characteristic length.

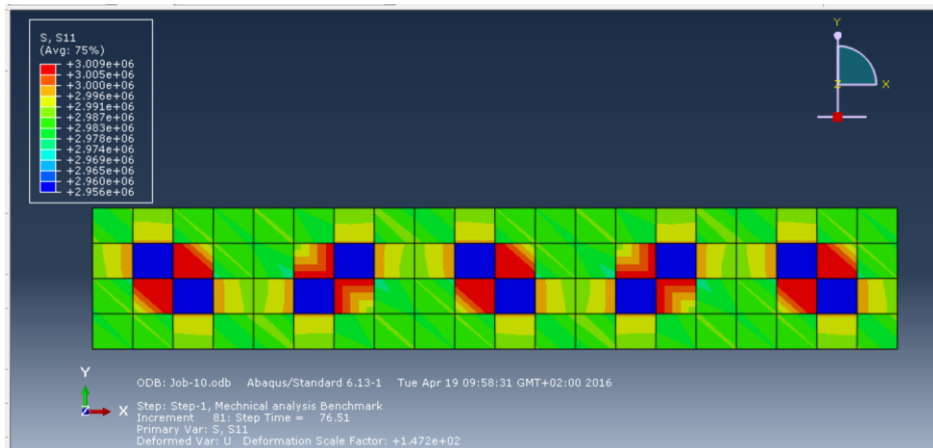


Fig.7. 9 Stress distribution with mesh size equals to 25x25mm (Case 4)

A complete simulation had been accomplished in this case. The result proved a very good agreement in constitutive law between ABAQUS and MATLAB simulations. It also proved the assumption that when implementing Fracture Energy the characteristic length is selected according to the mesh size.

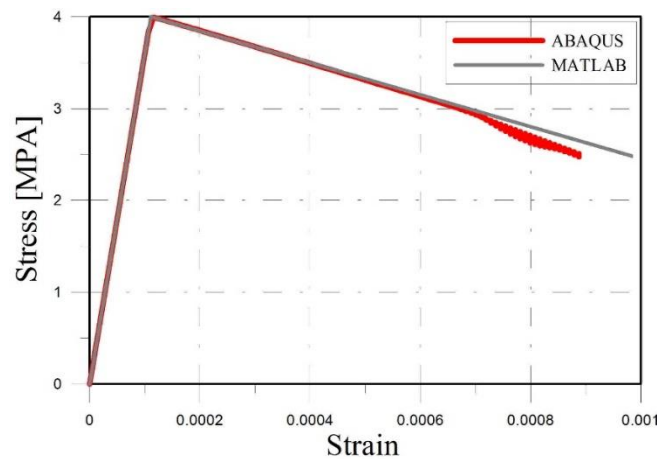


Fig.7. 10Fracture Energy Cracking Criterion (Case 4)

7.3Result and Conclusion

7.3.1 Result

The effect of the characteristic length in the results is now investigated. The characteristic length in function E_YgTm (Section 6.2.2) is defined as 5 millimeter. The stress distribution, elastic modulus and displacement are shown in the following.

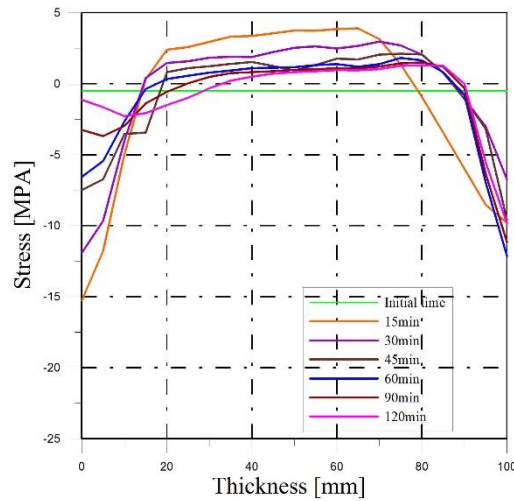


Fig.7. 11 Stress distribution along the thickness during 120min, with external load equal to 0.5MPa and mesh size equal to 5mm.

Now the secant modulus distribution graph shows a better match (Fig.7. 12).

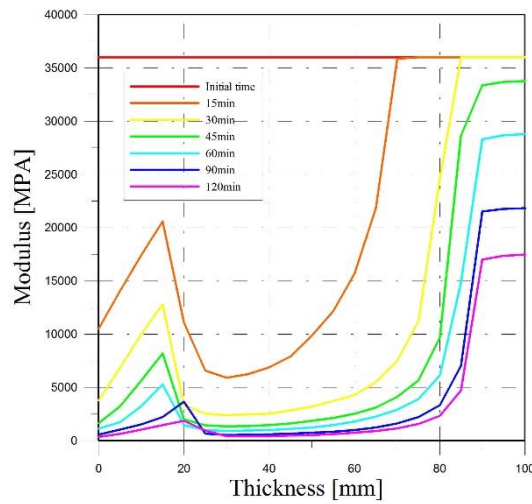


Fig.7. 12 Secant modulus distribution along the thickness during 120min, with external load equal to 0.5MPa and mesh size equal to 5mm.

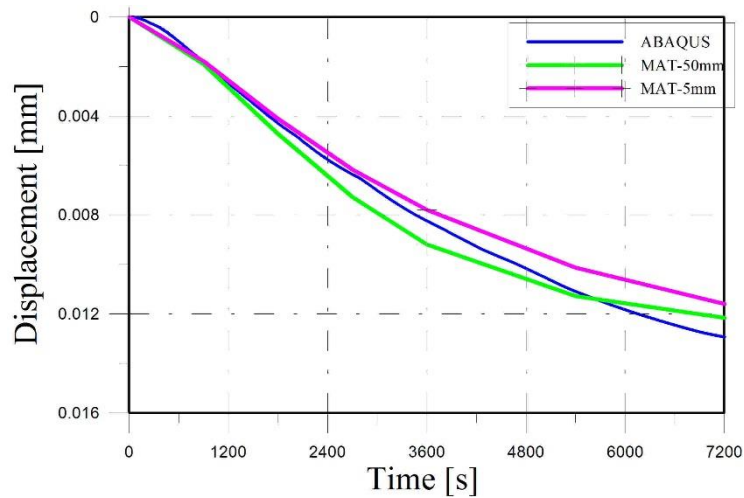


Fig.7. 13 Displacement histogram of ABAQUS (mesh size 5mm) results and MATLAB results (characteristic length 50mm and 5mm), when external load equal to 0.5MPa.

In Fig.7. 13 the displacements obtained with different mesh size by MATLAB script are compared to the ABAQUS output with mesh size equal to 5mm.

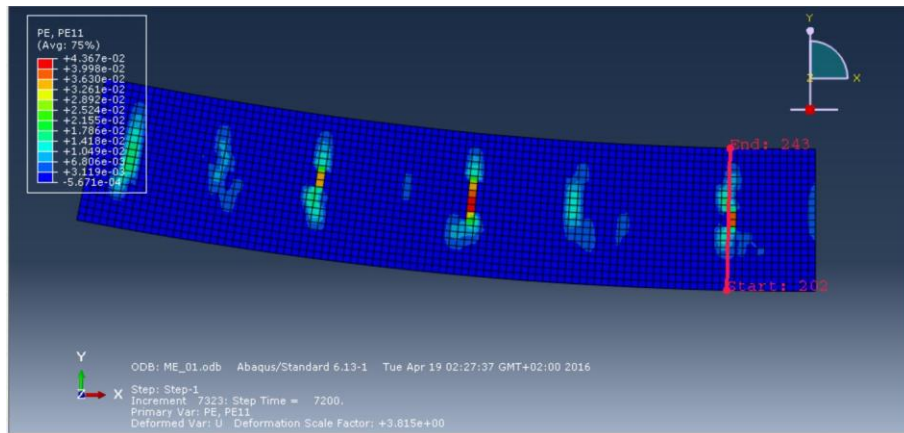


Fig.7. 14 Section 2-crack section

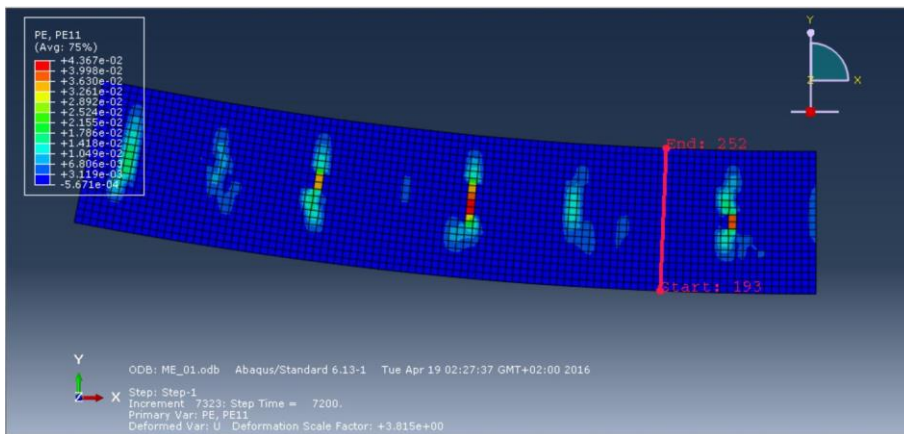


Fig.7. 15 Section 3-un-crack section

For the evaluation of the stresses, two different sections of the specimen are considered in Abaqus: a cracked section (Section 2) and an un-cracked section (Section 3) as shows in Fig.7. 14 and Fig.7. 15.

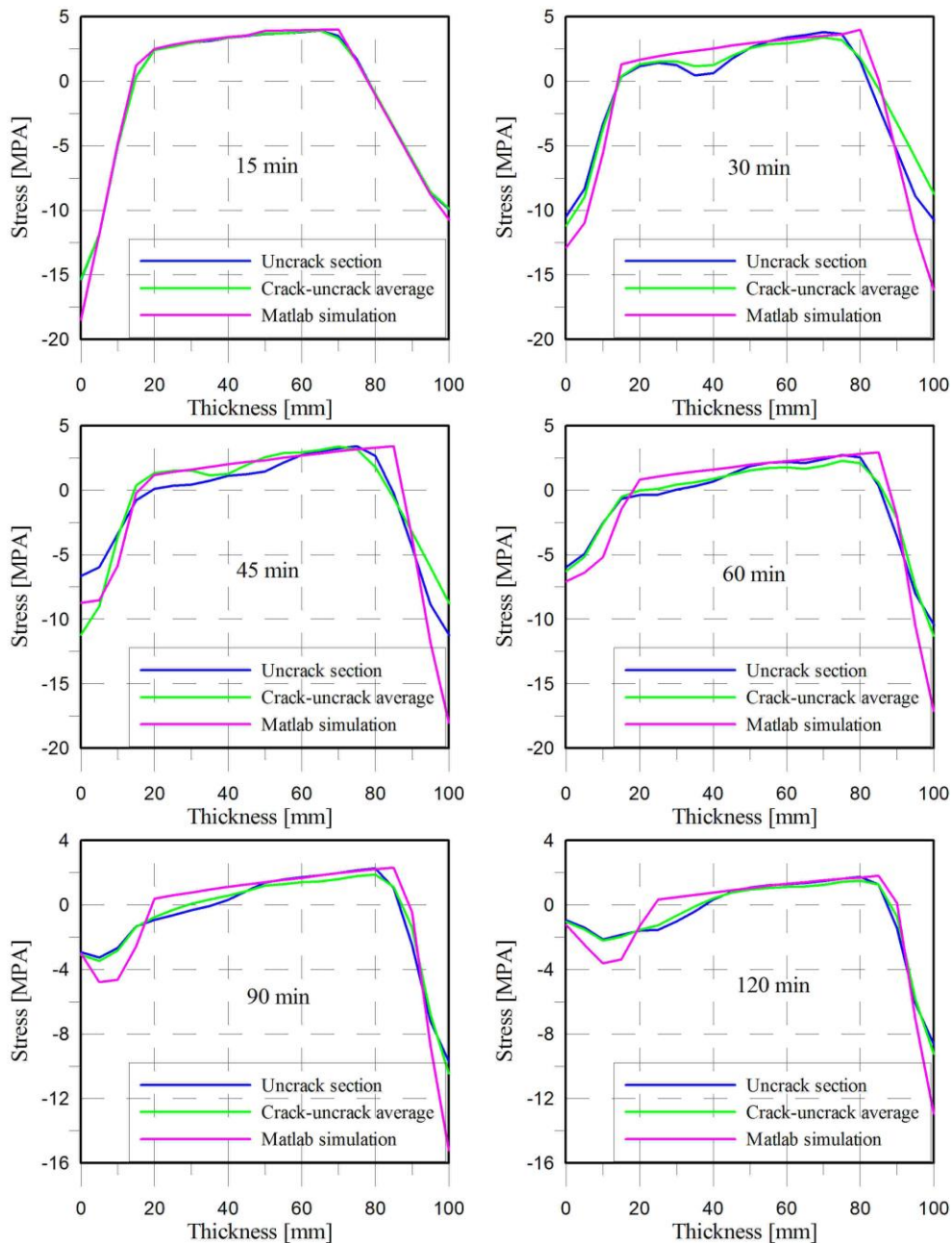


Fig.7. 16 Stress distribution: ABAQUS result section 1, average of section 2 and section 3, and MATLAB, along thickness (120min), external load (0.5MPa).

The average of the two sections is plotted together with the results regarding Section-1 (see Fig.7. 4). The stress distribution comparison between Matlab and Abaqus is shown in Fig.7. 16: the blue line is Abaqus simulation – Section 1, the green line is Abaqus simulation – average between Sections 1 and 2, violet line is Matlab simulation.

7.3.2 Conclusions

In ABAQUS software, the characteristic length is selected according to the mesh

size.

The Matlab algorithm is in perfect agreement with ABAQUS results in totally elastic condition (no cracking).

After cracking starts, the algorithm uses secant modulus instead of tangent modulus to simulate the modulus decay.

8. Material Stiffness Decay

In Chapter 6, a software has been developed in Matlab for simulating the behavior of concrete under thermal loading with given mechanical conditions. In this chapter, another software will be developed. The purpose of the software is to evaluate the secant modulus of the material by inverse analysis, once the thermal profile and the vertical displacements as functions of times are known.

As abovementioned, it is not easy to have direct observation of material modulus behavior in hot temperature conditions. However, if an experiment is performed, the specimen curvature and temperature variation respect to time can be observed directly. In Chapter 6 it was shown as starting from given thermal and mechanical properties, elongation and curvature of specimen can be calculated by solving a linear problem. With the same idea, it should be possible to evaluate modulus decay, once curvature and temperatures are known. This means that, the modulus could be reckon by a given serial of curvature historical profile and the corresponding temperature profile.

Generally, the mechanical behavior of the tests can be split into two classes: non-cracked conditions (when no cracking occurs thanks to high compression load) and cracked conditions. In this chapter, it is provided a detail description of the evaluation of secant modulus decay during non-cracking condition.

8.1 Algorithm Principle

8.1.1 Theoretical fundamental

Now the elastic modulus is the unknown, while the two known data are the thermal profile and the curvature.

If the elastic strain is still represented by: $\varepsilon_{elastic} = \varepsilon_0 + \chi y - \varepsilon_{th}$

And the relevant stress can be written as: $\sigma = E \cdot \varepsilon_{el} = E \cdot (\chi \cdot y + \varepsilon_0 - \varepsilon_{th})$

The average stress at the studied specimen section could be computed by:

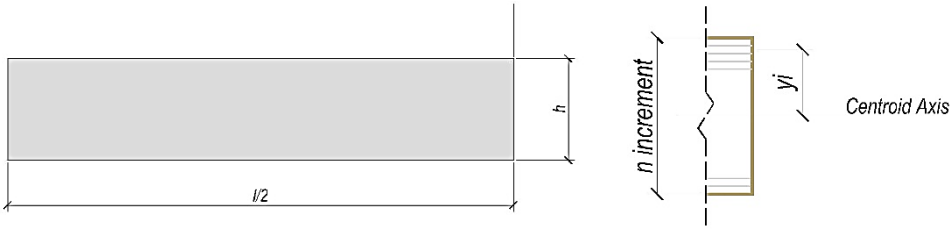
$$\sigma_{average} = \int_{-\frac{h}{2}}^{\frac{h}{2}} E \cdot \chi y dy + \int_{-\frac{h}{2}}^{\frac{h}{2}} E \cdot \varepsilon_0 dy - \int_{-\frac{h}{2}}^{\frac{h}{2}} E \cdot \varepsilon_{th} dy$$


Fig.8. 1 Geometry for studied model

With the purpose to simplify the formulas, it is reasonable to introduce some parameters so that the equations can be express in non-dimensional variables. Defining $\eta = \frac{y}{h}$, where h is the thickness of the simulating specimen, the former function could be written as:

$$\sigma_{average} = \int_{-\frac{1}{2}}^{\frac{1}{2}} E \cdot \chi \eta \cdot h d\eta + \int_{-\frac{1}{2}}^{\frac{1}{2}} E \cdot \varepsilon_0 d\eta - \int_{-\frac{1}{2}}^{\frac{1}{2}} E \cdot \varepsilon_{th} d\eta \quad (8.1)$$

Then the follow function could also be obtained:

$$\sigma_{average} \cdot \frac{e}{h} = \int_{-\frac{1}{2}}^{\frac{1}{2}} E \cdot \chi \eta^2 \cdot h d\eta + \int_{-\frac{1}{2}}^{\frac{1}{2}} E \cdot \varepsilon_0 \cdot \eta d\eta - \int_{-\frac{1}{2}}^{\frac{1}{2}} E \cdot \varepsilon_{th} \cdot \eta d\eta \quad (8.2)$$

The normalized eccentricity can be defined: $\xi = \frac{e}{h}$ (8.3)

Then the relation between stress and strain can still be described according to the following relation:

$$\sigma_{av} = \varepsilon_0 \cdot \tilde{E} + \chi h \cdot \tilde{S} - \tilde{\sigma}_{thav}$$

$$\sigma_{av} \cdot \xi = \varepsilon_0 \cdot \tilde{S} + \chi h \cdot \tilde{I} - m_{th}$$

Where,

$$\tilde{E} = \int_{-\frac{1}{2}}^{\frac{1}{2}} E d\eta ; \tilde{S} = \int_{-\frac{1}{2}}^{\frac{1}{2}} E \eta d\eta ; \tilde{I} = \int_{-\frac{1}{2}}^{\frac{1}{2}} E \eta^2 d\eta$$

And

$$\tilde{\sigma}_{thaverage} = \int_{-\frac{1}{2}}^{\frac{1}{2}} E \cdot \varepsilon_{th} d\eta; \quad m_{th} = \int_{-\frac{1}{2}}^{\frac{1}{2}} E \cdot \varepsilon_{th} \eta d\eta$$

The integrals can be written as the product of vectors:

$$\begin{aligned} \bar{E} &= [E_1 \quad E_2 \quad \dots \quad E_n]^T, \\ \bar{P}_E &= \frac{1}{n} [1 \quad 1 \quad \dots \quad 1]^T, \\ \bar{P}_S &= \frac{1}{n} [\eta_1 \quad \eta_2 \quad \dots \quad \eta_n]^T, \\ \bar{P}_I &= \frac{1}{n} [\eta_1^2 \quad \eta_2^2 \quad \dots \quad \eta_n^2]^T \\ \bar{P}_{th} &= \frac{1}{n} [\varepsilon_{th1} \quad \varepsilon_{th2} \quad \dots \quad \varepsilon_{thn}]^T \\ \bar{P}_{mth} &= \frac{1}{n} [\varepsilon_{th1}\eta_1 \quad \varepsilon_{th2}\eta_2 \quad \dots \quad \varepsilon_{thn}\eta_n]^T \end{aligned} \quad (8.4)$$

Where,

$$\eta_i = \frac{y_i}{h}$$

h : is the thickness of the specimen (Fig.8. 1).

y_i : is the distance from the geometric centroid (Fig.8. 1).

Then, the following expressions can be written:

$$\begin{aligned} \tilde{E} &= \bar{E}^T \cdot \bar{P}_E \\ \tilde{S} &= \bar{E}^T \cdot \bar{P}_S \\ \tilde{I} &= \bar{E}^T \cdot \bar{P}_I \\ \tilde{\sigma}_{thav} &= \bar{E}^T \cdot \bar{P}_{th} \\ \tilde{m}_{th} &= \bar{E}^T \cdot \bar{P}_{mth} \end{aligned} \quad (8.5)$$

It is now convenient to introduce a *new coefficient: the Normalized Distance between the stiffness centroid and the geometric centroid*:

$$\eta_G = \frac{\tilde{S}}{\tilde{E}} \quad (8.6)$$

It follows that:

$$\begin{aligned} \varepsilon_0 &= \frac{1}{\tilde{E}} \cdot (\sigma_{av} + \tilde{\sigma}_{thav} - \chi \cdot h\tilde{S}) \\ \sigma_{av} \cdot \xi &= \chi \cdot h\tilde{I} + \frac{\tilde{S}}{\tilde{E}} \cdot (\sigma_{av} + \tilde{\sigma}_{thav} - \chi \cdot h\tilde{S}) - \tilde{m}_{th} \end{aligned}$$

Simplifying the two equations, it is possible to write:

$$\sigma_{av} \cdot (\xi - \eta_G) = \bar{E}^T \cdot (\chi h \cdot \bar{P}_l + \eta_G \cdot \bar{P}_{th} - \chi h \cdot \eta_G \cdot \bar{P}_s - \bar{P}_{mth}) \quad (8.7)$$

$$\text{Defining } \bar{P}_{eq} = \chi h \cdot \bar{P}_l + \eta_G \cdot \bar{P}_{th} - \chi h \cdot \eta_G \cdot \bar{P}_s - \bar{P}_{mth}$$

The formal equation becomes

$$\sigma_{av} \cdot (\xi - \eta_G) = \bar{E}^T \cdot \bar{P}_{eq} \quad (8.8)$$

8.1.2 Least square method

By assuming the modulus as a function of the temperature:

$$E = a \cdot T^3 + b \cdot T^2 + c \cdot T + d \quad (8.9)$$

The unknown parameters can be collected in one vector:

$$\underline{A} = [a \quad b \quad c \quad d]^T \quad (8.10)$$

Defining the following matrix:

$$\underline{T} = \begin{bmatrix} T_1^3 & T_2^3 & \dots & T_n^3 \\ T_1^2 & T_2^2 & \dots & T_n^2 \\ T_1 & T_2 & \dots & T_n \\ 1 & 1 & \dots & 1 \end{bmatrix} \quad (8.11)$$

Then vector collecting the elastic modulus at any layer of the section for a given fire duration is represented by the following matrix form:

$$\bar{E}^T = \underline{A}^T \cdot \underline{T} \quad (8.12)$$

Hence, the following expression is valid for a given time step:

$$\sigma_{av} \cdot (\xi - \eta_G) = \underline{A}^T \cdot \underline{T} \cdot \bar{P}_{eq} \quad (8.13)$$

$$\text{Defining } \underline{B} = \underline{T} \cdot \bar{P}_{eq} = [\beta_1 \quad \beta_2 \quad \beta_3 \quad \beta_4]^T \quad (8.14)$$

$$\text{It is possible to obtain: } \sigma_{av} \cdot (\xi - \eta_G) = \underline{A}^T \cdot \underline{B} \quad (8.15)$$

When the curvature, the temperature profile and the normalized distance η_G are given with time, the vector of coefficients \underline{A} can be evaluated by using the *Least Square Method*.

The total square error is defined as the sum of the square error at any time step k:

$$Err = \sum_k^f \left[\underline{A}^T \cdot \underline{B}_k - \sigma_{av} \cdot (\xi - \eta_{Gk}) \right]^2 \quad (8.16)$$

The unknowns a, b, c and d are calculated by minimizing the error.

$$Err = \sum_k^f \left[a \cdot \beta_{1k} + b \cdot \beta_{2k} + c \cdot \beta_{3k} + d \cdot \beta_{4k} - \sigma_{av} \cdot (\xi - \eta_{Gk}) \right]^2$$

$$\frac{\partial Err}{\partial a} = 0, \quad \frac{\partial Err}{\partial b} = 0, \quad \frac{\partial Err}{\partial c} = 0, \quad \frac{\partial Err}{\partial d} = 0$$

For example, the expansion of the first equation is:

$$a \cdot \sum_k \beta_{1k}^2 + b \cdot \sum_k \beta_{1k} \beta_{2k} + c \cdot \sum_k \beta_{1k} \beta_{3k} + d \cdot \sum_k \beta_{1k} \beta_{4k} - \sum_k \sigma_{av} \cdot (\xi - \eta_{Gk}) \beta_{1k} = 0$$

Expanding all the equations and writing the result in matrix form:

$$\begin{bmatrix} a \\ b \\ c \\ d \end{bmatrix} \cdot \begin{bmatrix} \sum \beta_1^2 & \sum \beta_1 \beta_2 & \sum \beta_1 \beta_3 & \sum \beta_1 \beta_4 \\ \sum \beta_1 \beta_2 & \sum \beta_2^2 & \sum \beta_2 \beta_3 & \sum \beta_2 \beta_4 \\ \sum \beta_1 \beta_3 & \sum \beta_2 \beta_3 & \sum \beta_3^2 & \sum \beta_3 \beta_4 \\ \sum \beta_1 \beta_4 & \sum \beta_2 \beta_4 & \sum \beta_3 \beta_4 & \sum \beta_4^2 \end{bmatrix} - \begin{bmatrix} \sum_k \sigma_{av} \cdot (\xi - \eta_{Gk}) \beta_{1k} \\ \sum_k \sigma_{av} \cdot (\xi - \eta_{Gk}) \beta_{2k} \\ \sum_k \sigma_{av} \cdot (\xi - \eta_{Gk}) \beta_{3k} \\ \sum_k \sigma_{av} \cdot (\xi - \eta_{Gk}) \beta_{4k} \end{bmatrix} = 0 \quad (8.17)$$

Solving the equation, the results will give $\underline{A} = [a \ b \ c \ d]^T$, which is exactly the target of the algorithm. Since the normalized distance η_G is not known a priori, a first trial assumption is made; afterwards, when a first set of the unknowns a, b, c and d is evaluated a second trial η_G is evaluated and the iterative procedure is continued up to convergence.

8.2 Function Development and Modification

8.2.1 Functions

8.2.1.1 Basic Functions

Before starting to describe the new software, it is better to list the developed functions since the majority of them will be called for the new software.

$[E_Yog, E_Cr, Alf] = E_Yg(T)$ is a function to evaluate some temperature dependent properties according to the Eurocode suggestion. The intermediate values are evaluated by linear interpolation. The output includes:

E_Yog represents the tangent modulus according to *EN 1992-1-2 (2004)* suggestion.

E_Cr represents the “correct” tangent modulus taking into account the slab

kinematic behavior:

$$E' = \frac{E}{(1-\mu)}$$

Where, μ represents for the Poisson's Ratio of the studied material.

Alf represents the thermal expansion coefficient according to *EN 1992-1-2 (2004)* suggestion.

$[E_YgTen,...]=E_YgT(EpsI,T)$ is a function to determine whether to use the secant modulus or to use the tangent modulus. The function will determine the constitutive law according to temperature. Moreover, when tensile stress occurs, it will judge if the input data respects the constitutive law.

$EpsI$ represents the total strain at the evaluated point.

E_YgTen is the effective modulus. For different cases, it can be the tangent modulus or the secant modulus.

$[FiStr,...,Curv] = CPT_IP(E_Cr,Alf,TH,Th_Eps, SZ,BC_STR,thick, h, yi)$ is a function to evaluate the stress and strain distribution along the studied section. The input requirements include effective modulus, thermal expansion coefficient, thermal profile, geometry properties, etc.

$FiStr$ represents the stress distribution on the studied section.

$Curv$ represents the curvature of the studied section.

8.2.1.2 Further functions

Several new functions in this chapter have been written to develop the software. Two among them are worth to be pointed out.

$[...,NG,Curv,FiStr...] = Curve_OB(E_Cr,Alf,TH,SZ,BC_STR,thick, h, yi)$ is a function mainly focused on obtaining the curvature χ and the normalized distance η_G . It determines the stress distribution along the section as well. The function is very similar to *CPT_IP.m*.

$[Peq,Sg_AV,Kesi,...] = Modu_OB(Curv,NG,Alf,TH,SZ,BC_STR,thick, h, yi)$ is a function targeting the evaluation of the vector \mathbf{P}_{eq} , and the other vectors mentioned in Equation(8.4).

The least square method convergence will be find through an iteration method which is represented by the violet lines in the flow chart given by Fig.8. 2.

During the computation, the solution will not come out at the first time. Since usually the normalized distance η_G is an assumption. For each iteration, the new evaluated effective modulus replaces the input elastic modulus and compute the new values of η_G for the next iteration. The convergence should be achieved by comparing the difference between the evaluated modulus in two next steps:

$$err_E = \frac{E_i^{eff}}{E_{i+1}^{eff}} \quad (0.99 < err_E < 1.01)$$

Where, E_i^{eff} represents the result modulus from the i -th iteration.

The software just explained will be referred in the following as Software B.

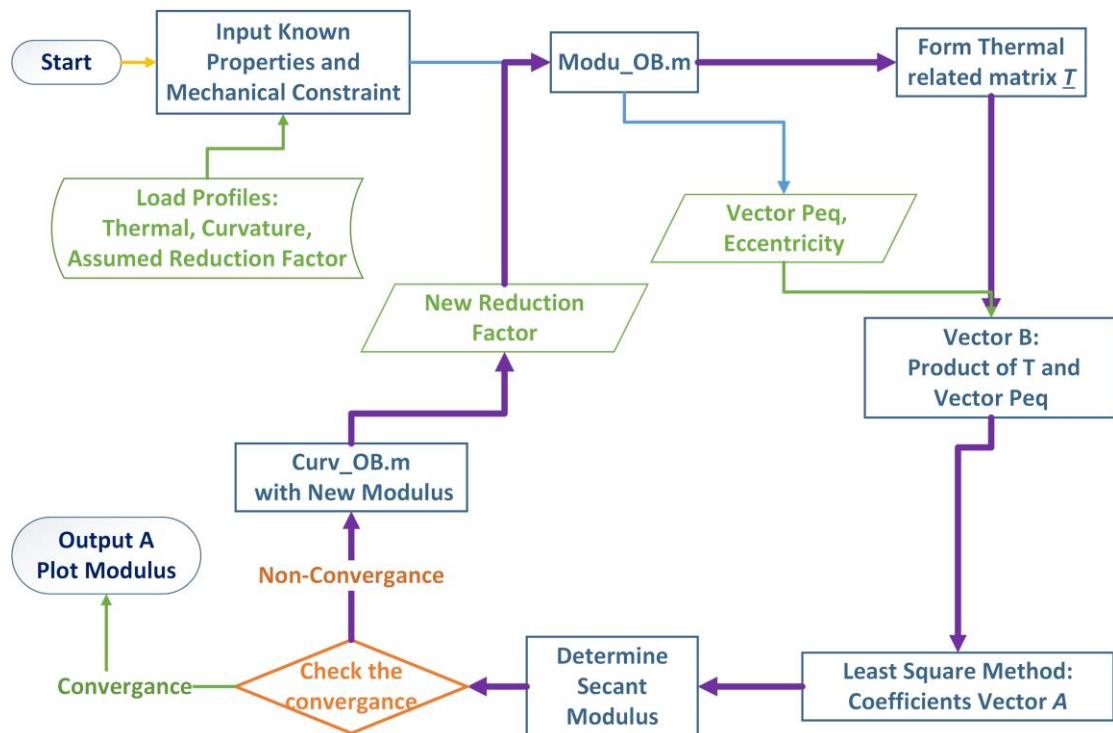


Fig.8. 2 Flow chart of the software

8.2.2 Accuracy of the function

Software B is checked by using the above discussed Software-A.

First of all, it is investigated the influence of interpolation of the tabular data given by EC2 as concerning the young modulus decay. If such data are implemented in the software as tabular data or interpolated via a cubic curve, some difference is expected. In

the following, this difference is shown.

The comparison is reported for three cases: external load equal to 10MPa, 5MPa and 0.5MPa.

From Fig.8. 3 till Fig.8. 5, the purple lines in the graph represents the result by using linear interpolation, while the green ones are the results by using three order interpolation..

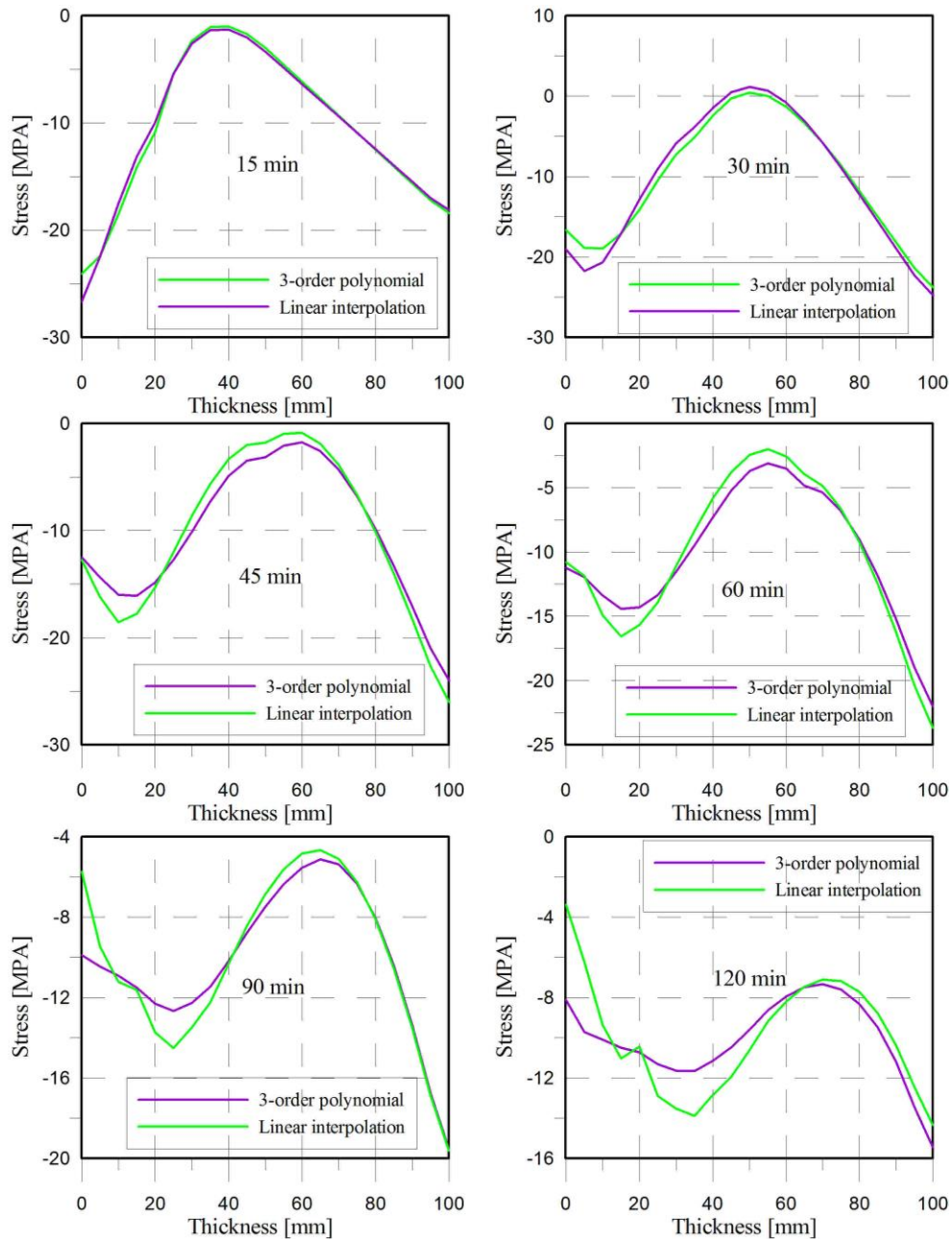


Fig.8. 3 Stress distribution comparison, elastic modulus implement by linear interpolation and 3 order polynomial, (external load=10mpa)

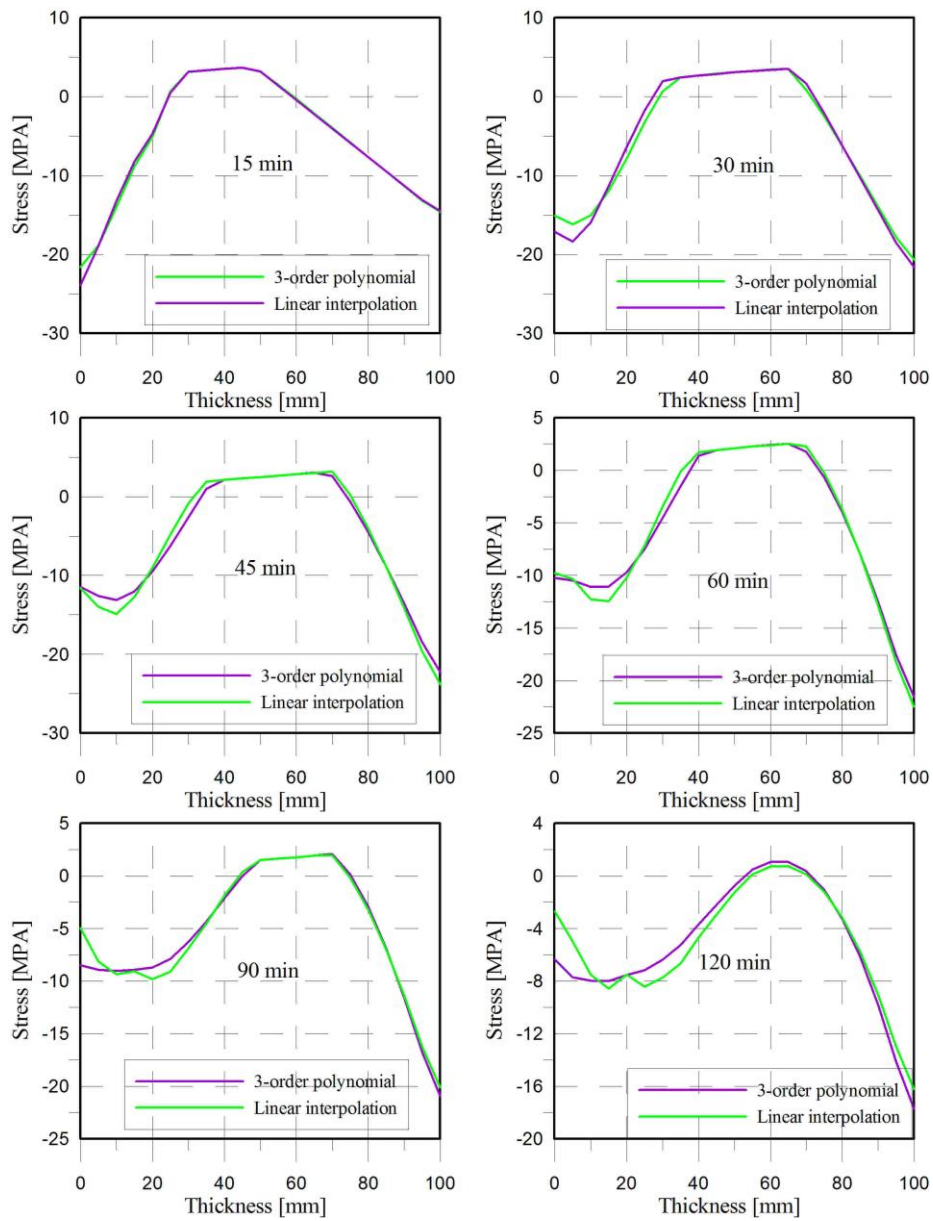


Fig.8. 4 Stress distribution comparison, elastic modulus implement by linear interpolation and 3 order polynomial, (external load=5mpa)

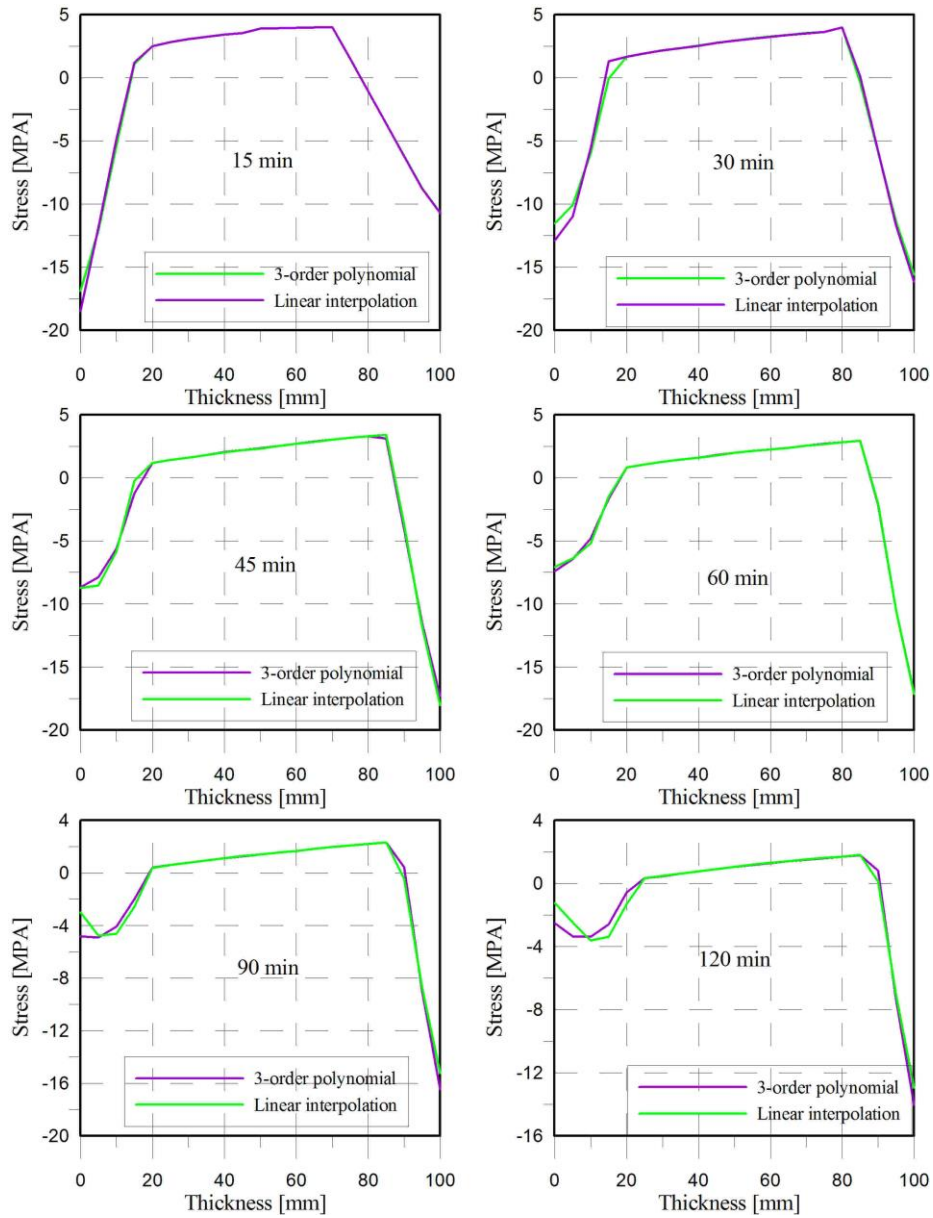


Fig.8. 5 Stress distribution comparison, elastic modulus implement by linear interpolation and 3 order polynomial, (external load=0.5mpa)

According to the abovementioned cases, the accuracy of the function *Curve_OB.m* is proved. The function *Modu_OB.m* is also verified because it is written exactly in same method except it has the purpose of obtain equivalent vector \bar{P}_{eq} . Meanwhile, it also proved that is reasonable to use the three order polynomial to describe the elastic modulus.

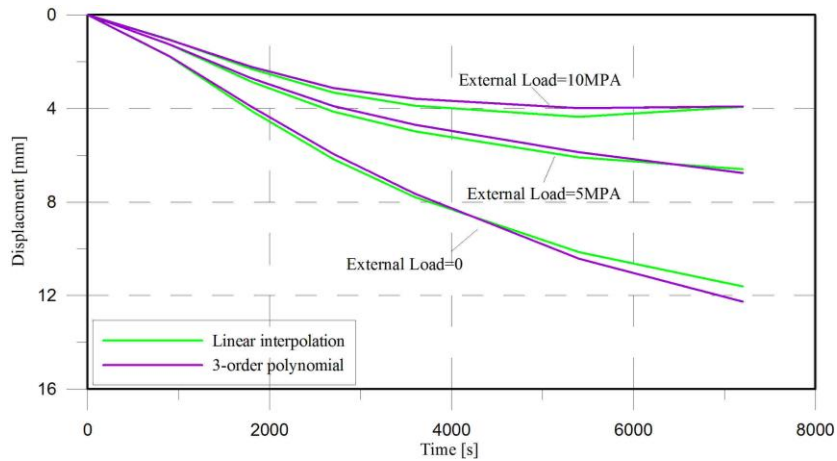


Fig.8. 6 Displacement comparison, (elastic modulus implement by linear interpolation and 3 order polynomial), among external load equal to 10MPa, 5MPa, 0.5MPa, respectively.

8.3 Software Development

8.3.1 Normalized Distance η_G

To implement the algorithm in the software, an important assumption is required: the normalized distance η_G . The factor is the bridge that convert the non-linear problem into a linear problem. So it starts with making the assumption on the normalized distance and verifying the normalized distance, hence, verifying the new software: **Software-B**.

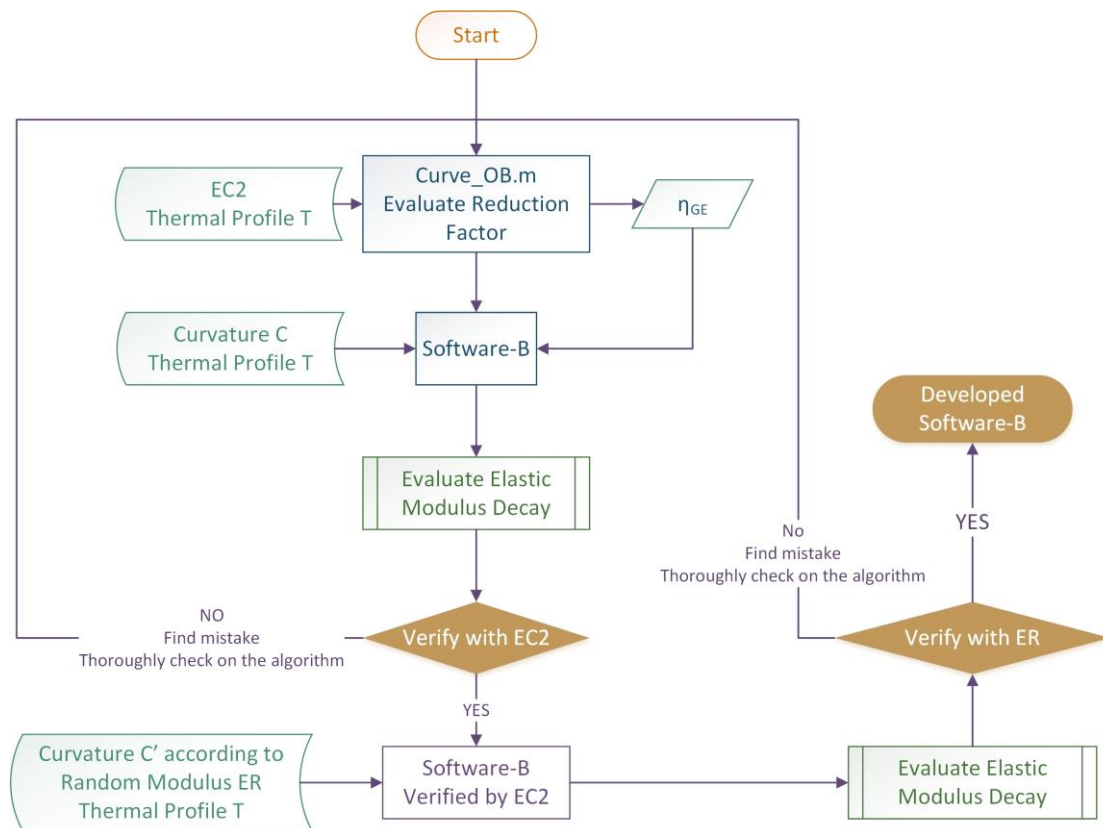


Fig.8. 7 Flow chart for assumption of normalized distance and Software-B development

In the following an input young modulus decay as a function of temperature is chosen for software A (Fig.8. 8, temperature unit is degree centigrade), together with a thermal profile (“experimental profile”).

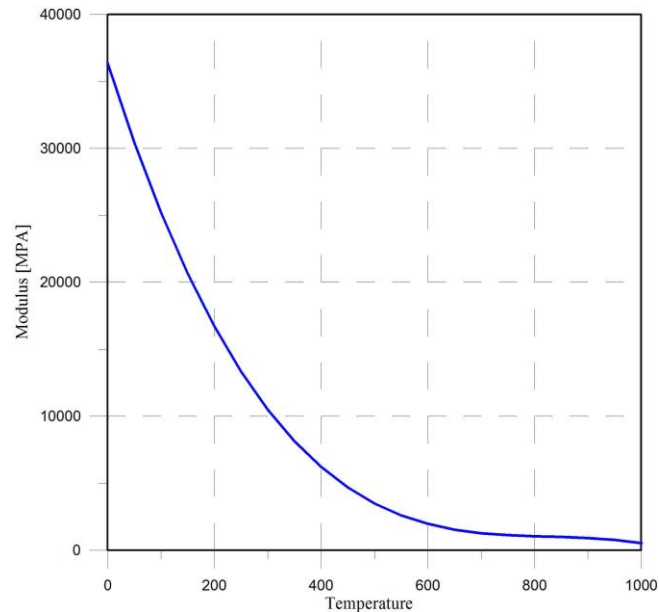


Fig.8. 8 Input modulus decay for Software A, as function of temperature (EC2 , 3 order polynomial interpolation)

Via Software A, the curvature as a function of time is worked out. Such curvature is used as “experimental” curvature for Software B together with the “experimental” thermal profiles.

Software B should give as output the young modulus decay used as input in Software A.

Comparing the plots (Fig.8. 9), the Software-B output returned exactly the input of Software A. But it should be paid attention that, when temperature is equal to 20°C, the 3 order polynomial did not fix the modulus on 36000Mpa, but shows slight in-accuracy.

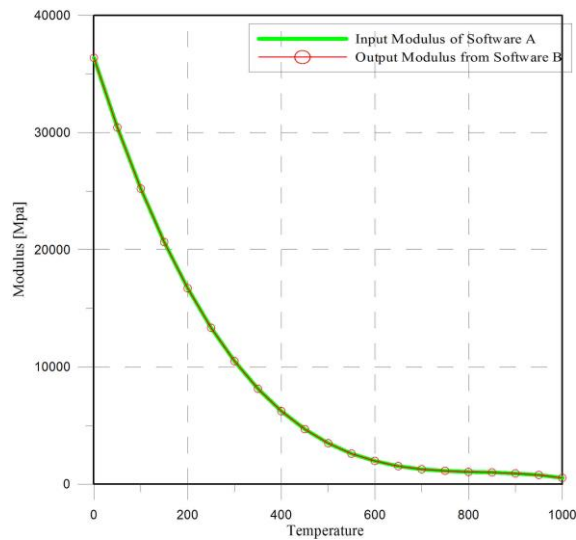


Fig.8. 9 Input modulus decay of Software A, and output modulus decay from Software B, as function of temperature.

The second step is to select a random modulus decay (Fig.8. 10) and evaluate a curvature profile by using Software A, and then to implement this curvature as input into Software-B. With the assumption that the modulus does not decay during the first trial in Software-B (η_G equals to 0, namely the stiffness centroid coincide with the geometry centroid), the software is expected to give same modulus decay as the input in Software A.

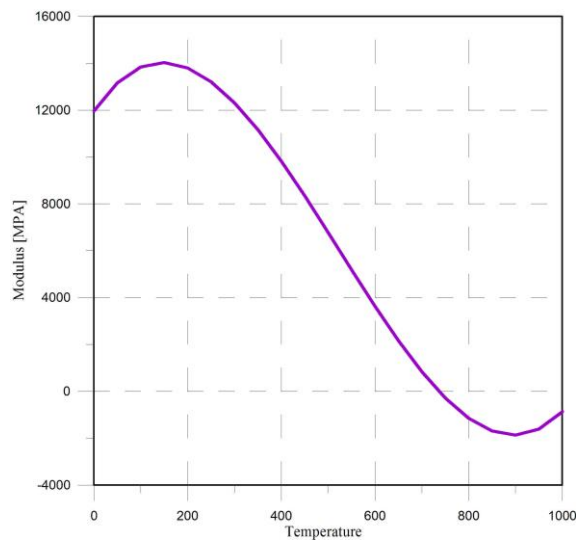


Fig.8. 10 Input modulus decay of Software A (Random selected), as function of temperature in fire duration.

The Fig.8. 11 shows the output. The horizontal axial represents the temperature and the unit is degree centigrade. The vertical axial represents the Young modulus and the unit is MPA. The graph shows that the output perfect matches the input, so it proves the availability and accuracy of Software-B.

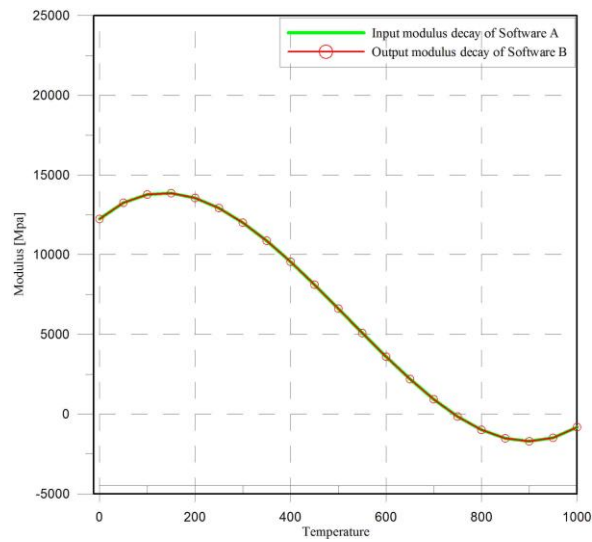


Fig.8. 11 Input modulus decay of Software A (Random selected), and output modulus decay from Software B, as function of temperature.

8.3.2 Algorithm Sensitivity

Since young modulus at 20 °C is usually, known, it could be convenient to define an algorithm where such information is used. In this way the number of unknowns is decreased.

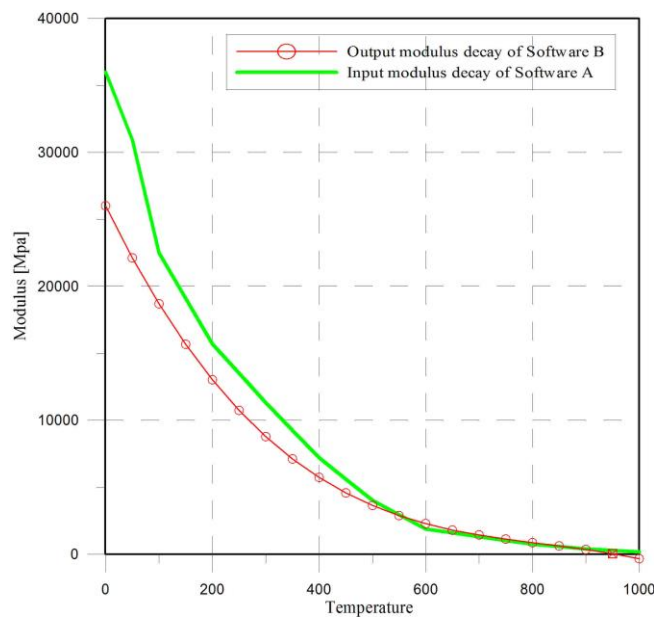


Fig.8. 12 Input modulus decay of Software A (implement by tabular data with intermediate value interpolated by linear interpolation), and output modulus decay of Software-B, as function of temperature.

8.4 Software Improvement

8.4.1 Algorithm modification

To improve the robustness of the algorithm a slightly different approach is used. The young modulus decay is expressed as a function of temperature via a three-order polynomial function, in which, the young modulus decay at ambient temperature is fixed

$$E = a \cdot (T - T_{amb})^3 + b \cdot (T - T_{amb})^2 + c \cdot (T - T_{amb}) + E_{amb} \quad (8.18)$$

In this way, the number of unknowns is three.

Equation (8.11) will be written as:

$$\underline{\underline{T}}^* = \begin{bmatrix} (T_1 - T_{amb})^3 & (T_2 - T_{amb})^3 & \dots & (T_n - T_{amb})^3 \\ (T_1 - T_{amb})^2 & (T_2 - T_{amb})^2 & \dots & (T_n - T_{amb})^2 \\ (T_1 - T_{amb}) & (T_2 - T_{amb}) & \dots & (T_n - T_{amb}) \end{bmatrix} \quad (8.19)$$

And the modulus can be expressed in the following metrical form:

$$\underline{\underline{E}} = \underline{\underline{A}}^T \begin{bmatrix} (T_1 - T_{amb})^3 & (T_2 - T_{amb})^3 & \dots & (T_n - T_{amb})^3 \\ (T_1 - T_{amb})^2 & (T_2 - T_{amb})^2 & \dots & (T_n - T_{amb})^2 \\ (T_1 - T_{amb}) & (T_2 - T_{amb}) & \dots & (T_n - T_{amb}) \end{bmatrix} + E_{amb} \cdot [1 \quad 1 \quad \dots \quad 1]_n \quad (8.20)$$

By repeating the procedure in the Section 8.1.2, then:

$$\sigma_{av} \cdot (\xi - \eta_G) = [\underline{\underline{A}}^T \cdot \underline{\underline{T}} + E_{amb} \cdot I_n] \cdot \bar{P}_{eq} \quad (8.21)$$

Where I_n represents for unit row vector with size n .

$$\text{Defining } \underline{\underline{B}} = \underline{\underline{T}} \cdot \bar{P}_{eq} = [\beta_1 \quad \beta_2 \quad \beta_3]^T \quad (8.22)$$

$$\text{It is possible to obtain: } \sigma_{av} \cdot (\xi - \eta_G) = \underline{\underline{A}}^T \cdot \underline{\underline{B}} + E_{amb} I_n \bar{P}_{eq} \quad (8.23)$$

If implementing *Least Square Method* the total square error is defined as the sum of the square error at any time step k :

$$Err = \sum_1^f \left[\underline{\underline{A}}^T \cdot \underline{\underline{B}} + E_{amb} I_n \bar{P}_{eq} - \sigma_{av} \cdot (\xi - \eta_{Gk}) \right]^2 \quad (8.24)$$

The unknowns a , b , and c are calculated by minimizing the error.

$$Err = \sum_1^f \left[a \cdot \beta_{1k} + b \cdot \beta_{2k} + c \cdot \beta_{3k} - \sigma_{av} \cdot (\xi - \eta_{Gk}) - E_{amb} I_n \bar{P}_{eq} \right]^2$$

$$\frac{\partial Err}{a} = 0, \quad \frac{\partial Err}{b} = 0, \quad \frac{\partial Err}{c} = 0$$

For example, expanding the first equation, it can be obtained:

$$a \cdot \sum_k \beta_{1k}^2 + b \cdot \sum_k \beta_{1k} \beta_{2k} + c \cdot \sum_k \beta_{1k} \beta_{3k} - \sum_k \left(\sigma_{av} \cdot (\xi - \eta_{Gk}) - E_{amb} I_n \bar{P}_{eq} \right) \beta_{1k} = 0$$

Expanding all the equations and writing the result in matrix form:

$$\begin{bmatrix} a \\ b \\ c \end{bmatrix} \cdot \begin{bmatrix} \sum \beta_1^2 & \sum \beta_1 \beta_2 & \sum \beta_1 \beta_3 \\ \sum \beta_1 \beta_2 & \sum \beta_2^2 & \sum \beta_2 \beta_3 \\ \sum \beta_1 \beta_3 & \sum \beta_2 \beta_3 & \sum \beta_3^2 \end{bmatrix} - \begin{bmatrix} \sum_k \left(\sigma_{av} \cdot (\xi - \eta_{Gk}) - E_{amb} I_n \bar{P}_{eq} \right) \beta_{1k} \\ \sum_k \left(\sigma_{av} \cdot (\xi - \eta_{Gk}) - E_{amb} I_n \bar{P}_{eq} \right) \beta_{2k} \\ \sum_k \left(\sigma_{av} \cdot (\xi - \eta_{Gk}) - E_{amb} I_n \bar{P}_{eq} \right) \beta_{3k} \end{bmatrix} = 0 \quad (8.25)$$

Solving the equation, the results will give $\underline{A} = [a \quad b \quad c]^T$, which is exactly the target of the algorithm. The rest procedure remains as before.

8.4.2 Software Modification

Since the stiffness implementing assumption function is changed into Equation(8.18), the Matlab functions *E_Yg.m* need to be modified according to this change. Software B is also modified according to Equation(8.24) and Equation(8.25).

The improved Software B will be taken into further implementation.

8.5 Experimental Data Implementation

8.5.1 Experimental Data

So far, several experiments had been carried out by the laboratory and they provide amount of estimated data. For an experimental specimen, the vertical displacement and the thermal profile can be obtain directly. If vertical displacement is known, curvature can be evaluated according to Mechanical principles.

Two concrete mixes with different type of fiber have been investigated. The mixes fibers are: Monofilament fiber and Fibrillate fiber. And three specimens have been implemented into experiment: *Monofilament B*, *Fibrillate A*, and *Fibrillate B*.

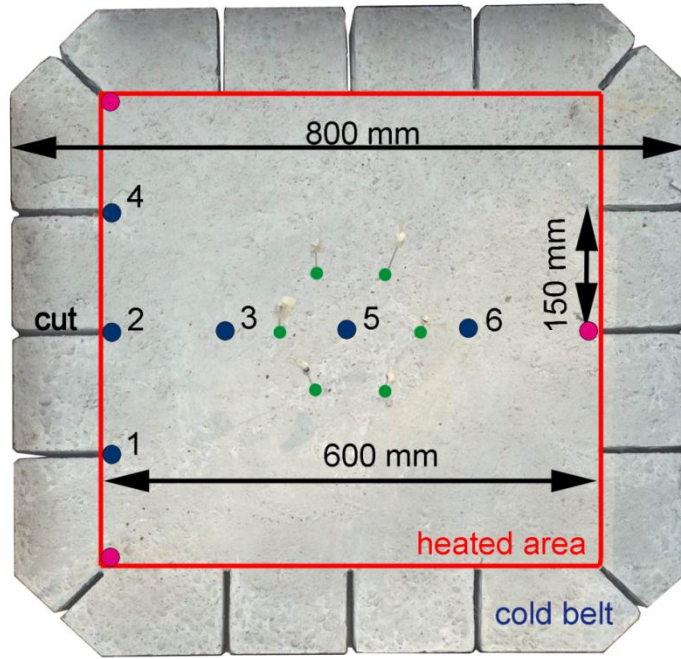


Fig.8. 13 Specimen investigated in experiment.

Fig.8. 13 shows a picture of the specimen. It is a concrete slab (800x800x100 mm) subjected to Standard Fire (ISO 834) at the intrados under biaxial membrane loading. The experiment of specimen Monofilament B and Fibrillate A are performed with external load equals 10MPa, while the experiment of Fibrillate B is performed with external load equals 5MPa.

During the test, temperature was monitored through the thickness via embedded sensors placed at the distances of 10, 20, 30, 40, 50 and 60 mm from the exposed face (Fig.8. 15). The flexural behavior was monitored through 6 *Linear Voltage Displacement Transducers* (LVDTs) measuring the vertical displacements at the extrados.

Fig.8. 14 shows the location of the LVDTs. The curvature can be evaluated through vertical displacements and the vertical displacement at specimen centroid can be evaluated by Equation(8.26).

$$D_{cen} = \frac{(LVDT2 + LVDT5^*)}{2} \quad (8.26)$$

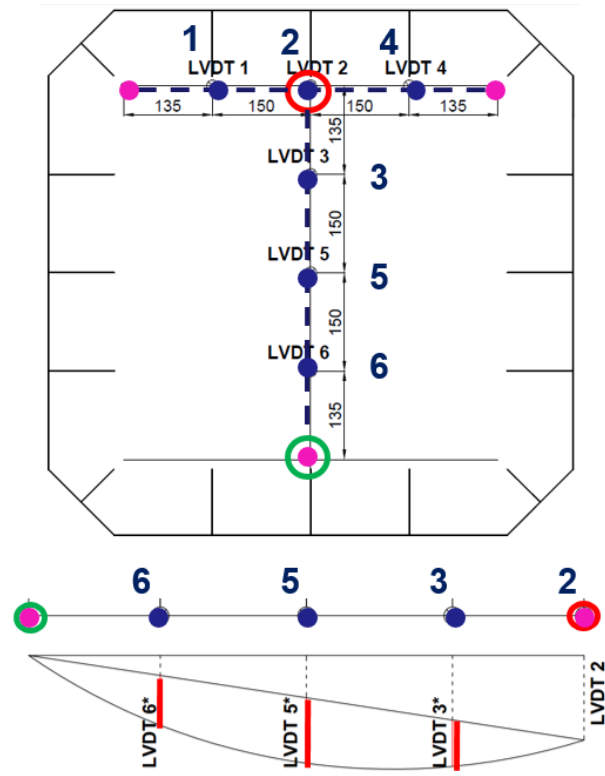


Fig.8. 14 Locations of LVDTs and evaluation method.

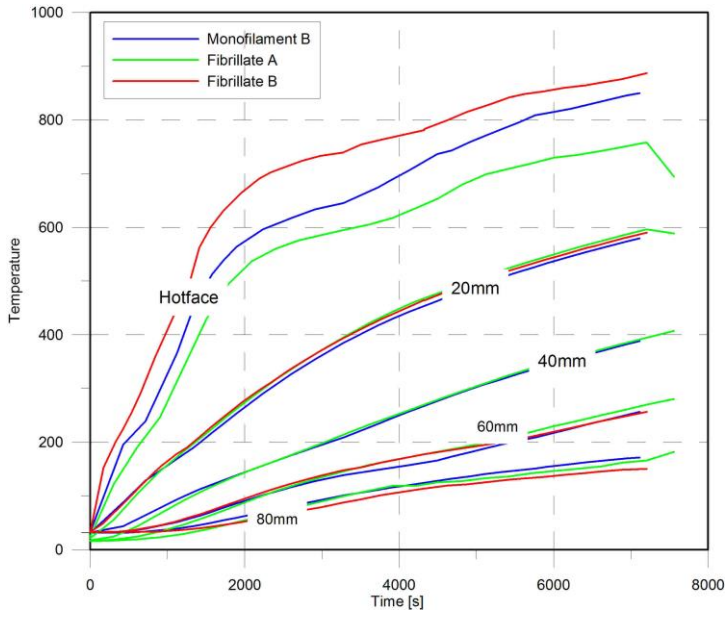


Fig.8. 15 Evaluated thermal profile according to experimental temperatures, regarding different thickness, for specimens Monofilament B, Fibrillate A, and Fibrillate B.

The experimental displacements of each specimen are evaluated and plotted in Fig.8.

16.

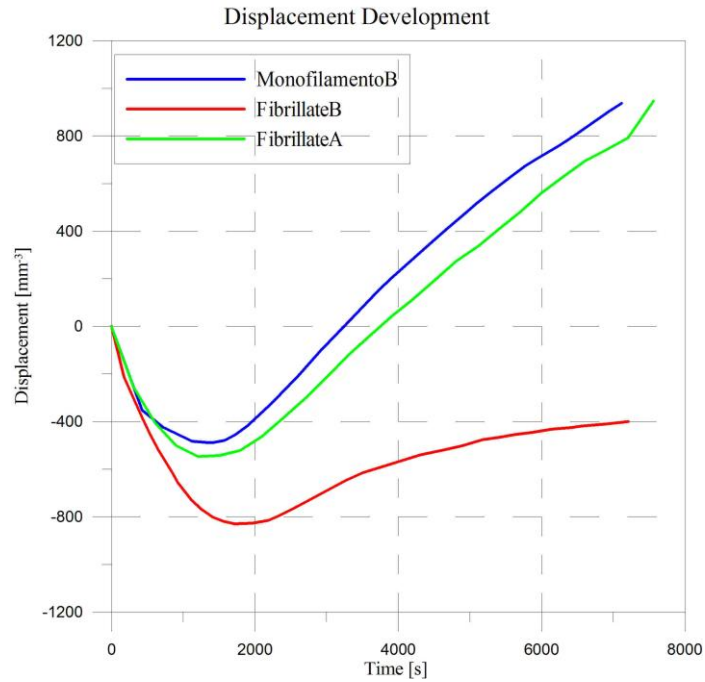


Fig.8. 16 Experiment obtained specimen vertical displacement profile, for specimen Monofilament B, Fibrillate A, and Fibrillate B.

8.5.2 Evaluation of Stiffness Decay

The given data (Fig.8. 15 and Fig.8. 16) are implemented into Software B. The material secant modulus at ambient temperature (20°C) is fixed at 30GPa (Lo Monte, 2013), and the stiffness decay according to EC2 suggestion is given by Fig.8. 17

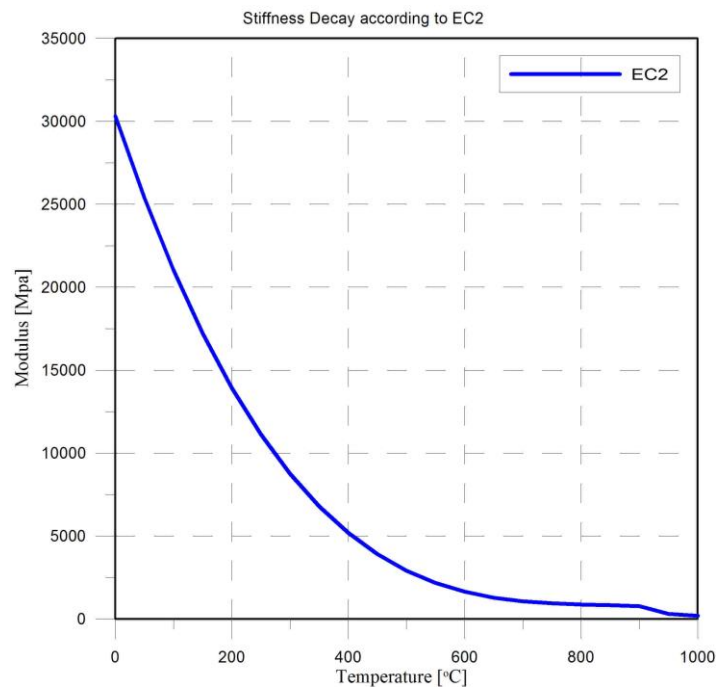


Fig.8. 17 Stiffness decay suggested by EC2, as a function of temperature.

Fig.8. 18 shows the material stiffness decay evaluated by inverse analysis. The vertical axial represents evaluated secant modulus with unit as Mpa, and the horizontal axial represents temperature with unit is degree centigrade.

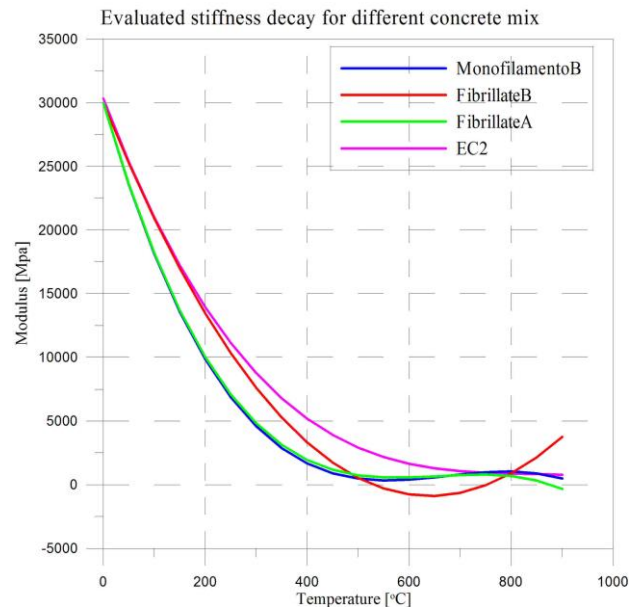


Fig.8. 18 Modulus decay for 4 specimen evaluated by numerical simulation, as function of temperature.

The modulus decay obtained from specimen Monofilament B and Fibrillate A show rather close results. This result is reasonable since for the two specimens, the curvature and temperature profile, which are the only defined parameters according to the algorithm and the software input, are almost the same. The external load implemented on the mentioned 2 specimens was 10MPA which means total elastic behavior of the specimen (no cracking).

Fig.8. 19 compares the experimental displacements with the one obtained according to the stiffness decay given by Fig.8. 18, and the one evaluated according to EC2 stiffness decay. Looking at specimens Monofilament B and Fibrillate A, during the early stage the displacement curve according to Evaluated and EC2 suggestion stiffness decay are generally in agreement with the experiment results. However, after the early stage, the EC2 curve does not stay with the other two anymore. Observing the total fire duration, the displacement curve according to evaluated stiffness is nearly in agreement with the experimental results.

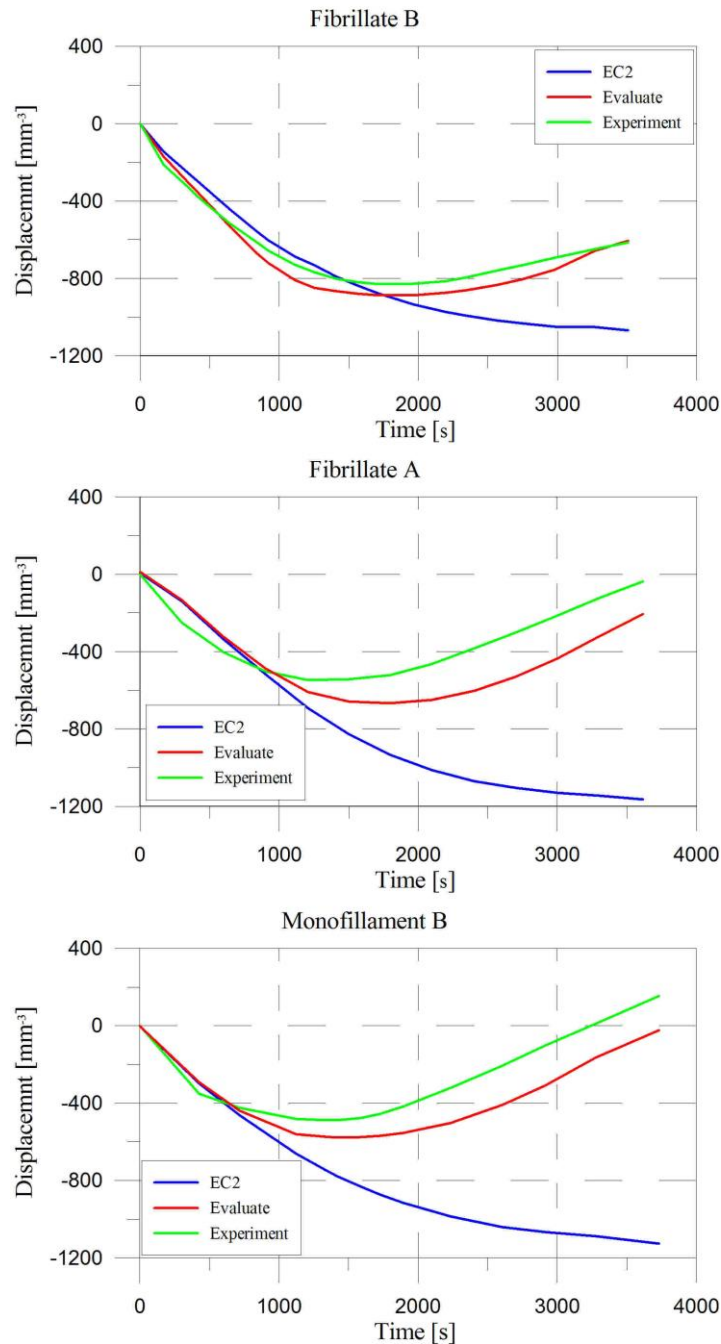


Fig.8. 19 Comparison of displacements obtained according to EC2 stiffness decay, software evaluated stiffness decay, and experiment results, as function of temperature, for different specimens.

On Fibrillate B case, it is interesting to see the software also works well during the elastic stage. Since the external confined load is 5MPa, which means cracking may occur inside the specimen during the test. Unfortunately, so far the improved Software B has not been designed to deal with cracking condition and the method to deal with cracking condition is still under investigating.

9. Conclusion

The object of present work is to study concrete cracking behavior and stiffness decay in hot conditions. Cracking behavior was investigated by performing numerical simulation in the commercial software Abaqus, and by comparing the results with a script developed in Matlab (Software A), considering cracking through the definition of the secant elastic modulus. The decay of concrete stiffness with temperature was studied by performing the inverse analysis of experimental data; back analysis was carried out through an algorithm developed in the present work and implemented in Matlab (Software B).

The results obtained allow to draw the following concluding remarks.

Cracking Behavior

Software A is developed to work out the mechanical behavior of concrete members by means of sectional analysis, taking into account cracking through the definition of the secant elastic modulus when tensile strength is overcome. Concrete is considered elastic in compression.

Software A, which is based on algorithm, is developed mainly focus on studying the concrete cracking behavior under high temperature. The results are compared with those obtained via the commercial software Abaqus.

Such comparison allowed to understand how Abaqus deals with cracking fracture energy mainly regarding the characteristic length. The study high lighted the mesh dependency of the results obtained from abaqus which is caused by the dependency of the characteristic length on the mesh size. This result was partly expected because in un-reinforced concrete, the brittle material behavior leads to strain localization and therefore to a crack pattern depending on the mesh size.

In reinforced concrete tensile behavior is mainly driven by steel, the ductile behavior of which brings in a more even distribution of cracks and a much less mesh dependency.

In the work at hand characteristic length for un-reinforced concrete is considered by Abaqus as equal as the mesh size.

Evaluation of Material Stiffness Decay

Starting from the usual assumption of Navier-Bernoulli the section mechanics of concrete members can be defined also in the conditions if elastic behavior is considered. Such hypothesis can be considered if cracking does not occur since compressive stresses are usually lower than the compressive strength. Based on these assumptions an algorithm for performing inverse analysis aimed at evaluating the decay of elastic modulus with the temperature was developed in Matlab starting from experimental data.

This approach was applied to experimental test carried out at Politecnico di Milano on concrete slabs (800x800x100mm²) subjected to heating at the bottom while an external membrane load of compression was applied. Thanks to the external load no cracking occurred this making possible to assume elastic behavior of the material. Since during the test thermal profile and out of plane displacements were monitored, the curvature of the slab and the temperature in the thickness are defined as a function of fire duration.

By defining the decay of the concrete stiffness via a third order polynomial function its expression is known if four parameter are calculated. In the present work, however, the young modulus at 20 °C was considered as known, this decreasing the unknown parameters from 4 to 3.

The parameters are defined implementing the least square error method defining the error as the difference between the experimental and the numerical curvatures.

After checking the reliability of the algorithm by generating benchmarks through software A, the approach was applied to 3 experimental tests. The tests were performed on 3 slabs:

Monofilament B: Concrete with monofilament polypropylene fiber and external load of 10Mpa

Fibrillated A: Concrete with fibrillated polypropylene fiber and external load of 10Mpa

Fibrillated B: Concrete with fibrillated polypropylene fiber and external load of 5 Mpa

The results showed as iterative procedure implemented in the software allowed to

obtain the results with a low computational cost.

By increasing the load from 5 to 10 Mpa, a steeper decay of the young modulus was observed for lower temperatue mainly due to the higher compressive stresses in the hot layers. For higher temperatures the decay of the stiffness with 10 Mpa was lower probobaly because such compression allowed to avoid cracking in the concrete core.

Reference

- ACI 216-1.07, (2007), *Code requirements for determining fire resistance of concrete and masonry construction assemblies*, Report by Joint ACI/TMS Committee 216, 32 pp.
- Bamonte P. and Gambarova P. G., (2010), “Thermal and Mechanical Properties at High Temperature of a Very High-Strength Durable Concrete”, *Journal of Materials in Civil Engineering - ASCE*, pp. 545-555.
- Bayasi Z. and McIntyre M., (2002), “Application of Fibrillated Polypropylene Fibers for Restraint of Plastic Shrinkage Cracking in Silica Fume Concrete”, *Materials Journal*, 99 (4), pp. 337-344.
- Bazant Z. P. and Kaplan M. F., (1996), *Concrete at High Temperature: Material Properties and Mathematical Models*, Longman, London (United Kingdom).
- Blundell R., Diamond C. and Browne R. G., (1976), “The Properties of Concrete Subjected to Elevated Temperatures”, Report No. 9, Construction Industry Research and Information Association - CIRIA, Underwater Engineering Group, London (United Kingdom).
- Buchanan A. H., (2001), *Structural design for fire safety*, John Wiley & Sons, Chichester, New York (USA), 448 pp.
- Cruz C. R. and Gillen M., (1980), “Thermal Expansion of Portland Cement Paste, Mortar, and Concrete at High Temperature,” *Fire and Material*, 4 (2), p. 66-70.
- Cruz C. R., (1966), “Elastic Properties of Concrete at High Temperatures”, Department Bulletin 191, Journal of the Portland Cement Association Research and Development Laboratories, 8 (1), pp. 37-45.
- Da ãn J. F., (2001), “Evaluation des proprietes de transfert dans les materiaux cimentaires”, *Reveu Francaise de Genie Civil, Union*, pp. 179-202.
- Diederichs U., Jumppanen U-M., Schneider U., (1995), “High temperature properties and spalling behaviour of high strength concrete”, *Proceedings of the Fourth Weimar Workshop on High Performance Concrete: Material Properties and Design*, held at Hochschule fur Architektur und Bauwesen (HAB), Weimar, Germany, October 4th and 5th, 1995, pp. 219-236.
- Ehm C., (1985), “Experimental Investigations of the Biaxial Strength and Deformation of Concrete at High Temperatures”, Thesis, Technical University of Braunschweig

(Germany).

EN 12390-2:2009, *Testing fresh concrete – Slump test*, European Committee For Standardization, Brussels (Belgium).

EN 12390-3:2009, *Testing hardened concrete – Compressive strength of test specimen*, European Committee For Standardization, Brussels (Belgium).

EN 12390-6:2009, *Testing hardened concrete, Part 6: Tensile splitting strength of test specimens*, European Committee For Standardization, Brussels (Belgium).

EN 1991-1-2:2004, *Eurocode 1: Actions on structures Part 1-2: General actions - Actions on structures exposed to fire*, European Committee for Standardization (CEN), Brussels, 2004.

EN 1992-1-2:2004. *Eurocode 2: Design of concrete structures Part 1-2: General rules - Structural fire design*, European Committee for Standardization (CEN), Brussels (Belgium).

Feldman R. F. and Sereda P. J. (1968), “A Model for Hydrated Portland Cement Paste as Deduced from sorption-length Change and Mechanical Properties”, *Materiaux et Construction*, 1 (6), pp. 509-520.

Felicetti R. and Gambarova P. G., (1998), “On the Residual Tensile Properties of High Performance Siliceous Concrete Exposed to High Temperature”, Special Volume in honour of Z. P. Bazant’s 60th Anniversary, Prague, March 27-28, Ed. Hermes (Paris), pp. 167-186.

Felicetti R., Gambarova P. G., Rosati G. P., et al., (1996), “Residual mechanical properties of high-strength concretes subjected to high-temperature cycles”, *Proceedings, 4th International Symposium on Utilization of High-Strength/High-Performance Concrete*, Paris, France, 1996, pp. 579-588.

fib Bulletin 38 (2007), *Fire Design of Concrete Structures - Materials, Structures and Modelling*, International Federation for Structural Concrete (*fib*), Lausanne (Switzerland), April 2007.

Fu Y. F. and Li L. C., (2011), “Study on mechanism of thermal spalling in concrete exposed to elevated temperatures”, *Materials and Structures*, 44, pp. 361-376.

Gao D. Y., Yan D. M. and Li X. Y., (2012), “Splitting strength of GGBFS concrete in incorporating with steel fiber and polypropylene fiber after exposure to elevated temperatures”, *Fire Safety Journal*, 54, pp. 67-73.

-
- G éard B., Breyse D., Ammouche A., Houdusse O. and Dirdry O., (1996), “Cracking and permeability of concrete under tension”, *Materials and Structures*, 29, pp. 141-151.
- Giuliani L, Crosti C and Gentili F. (2012), “Vulnerability of bridges to fire”, *proc. of the 6th International Conference on Bridge Maintenance, Safety And Management – IABMAS, Stresa (Italy)*, p. 313.
- Guo Y. C., Qian J. S. and Wang X., (2013), “Pore Structure and Influence of Recycled Aggregate”, *Mathematical Problems in Engineering, Research Article*, pp. 1-7.
- Hammer T. A., “HIGH-STRENGTH CONCRETE PHASE 3, Compressive strength and E-modulus at elevated temperatures,” SP6 Fire Resistance, Report 6.1, SINTEF Structures and Concrete, STF70 A95023, February, 1995.
- Harmathy T. Z. and Allen L. W., (1973), “Thermal Properties of Selected Masonry Unit Concretes”, *American Concrete Institute – ACI Journal*, 70, pp. 132-142.
- Harmathy T. Z., (1970), “Thermal properties of concrete at elevated temperatures”, *Journal of Materials*, 5 (1), pp. 47-74.
- Heinfling G., Stabler J., Baker G. and Reynouard J.M., (1998), “ Effects of high temperatures on the fracture energy of concrete”, *Proceedings of the 3rd International Conference on Fracture Mechanics of Concrete Structures – FRAMCOS 3*.
- Kalifa P. and Tsimbrovska M., (1998), *Comportement des BHP a hautes temperatures: etat de la question et resultats experimentaux*, Cahiers du Centre Scientifique et Technique du Batiment – CSTB, Paris (France), 16 pp.
- Kalifa P., Ghene G. and Galle C., (2001), “High-Temperature Behaviour of HPC with Polypropylene Fibres: From Spalling to Microstructure”, *Cement and Concrete Research* 31, pp. 1487-1499.
- Kalifa P., Menneteau F. D. and Quenard D. (2000), “Spalling and Pore Pressure in HPC at High Temperatures”, *Cement and Concrete Research*, 30, pp. 1915-1927.
- Khaliq W., Kodur V., (2011), “Thermal and mechanical properties of fibre reinforced high performance self-consolidating concrete at elevated temperatures”, *Cement and Concrete Research*, 41(11), pp. 1112-1122.
- Khoury G. A. (2000) “Effect of fire on concrete and concrete structures”, *Progress in Structural Engineering and Materials*, 2, pp. 429-447.
- Khoury G. A., (2008), “Polypropylene Fibres in Heated Concrete. Part 2: Pressure Relief

-
- Mechanisms and Modelling Criteria”, Magazine of Concrete Research, 60 (3), pp. 189-204.
- Kılıç A., Atış C. D., Teymen A., et al., (2008), “The influence of aggregate type on the strength and abrasion resistance of high strength concrete”, Cement & Concrete Composites, 30, pp. 290-296.
- Kodur V. K. R., Cheng Fu-Ping, Wang Tien-Chih and Sultan M. A., (2003), “Effect of Strength and Fiber Reinforcement on Fire Resistance of High-Strength Concrete Columns”, Journal of Structural Engineering, 129(2), pp.253-259.
- Lie T. T., Kodur V. K. R., (1996), “Thermal and mechanical properties of steel-fibre-reinforced concrete at elevated temperatures”[J], Canadian Journal of Civil Engineering, 23(2), pp. 511-517.
- Lo Monte F., (2014), *Reinforce Concrete in Fire: from Materials Behaviour to Spalling Sensitivity and Structural Modelling*, (Supervisors: P. G. Gambarova and R. Felicetti).
- Lo Monte F., Chiara Rossino, and Roberto Felicetti., (2015), “Spalling Test on Concrete Slabs under Biaxial Membrane Loading”, 4th Workshop on Concrete Spalling due to Fire Exposure, Leipzig-Germany
- Marechal J. C., (1972), “Variations in the Modulus of Elasticity and Poisson’s Ratio with Temperature”, Paper SP 34-27 in Concrete for Nuclear Reactors, American Concrete Institute - ACI, Farmington Hills (Michigan), pp. 495-503.
- Meftah F., (2005), *Comportement des bétons en température*, Master course of the Ecole Nationale des Ponts et Chaussées, Champs sur Marne (France), 68 pp.
- Miah J. MD. and Shamima A., (2013), *The Influence of Pore Pressure on the Apparent Tensile Strength of High-Performance Concrete with and without Polypropylene Fibres*, (Supervisors: R. Felicetti and F. Lo Monte).
- Mindeguia J. C., Pimienta P., Carrè H., and Borderie C. L., (2013), “Experimental Analysis of Concrete Spalling due to Fire Exposure”, European Journal of Environmental and Civil Engineering, 17 (6), pp. 453-466.
- Nanstad R. K., (1976), “A Review of Concrete Properties for Prestressed Concrete Pressure Vessels”, ORNL/TM-5497, Oak Ridge National Laboratory, Oak Ridge (Tennessee, USA).
- Niry R. R., Beaucour A.-L., Hebert R., et al., (2013), “Thermal stability of different siliceous and calcareous aggregates subjected to high temperature”, Proceedings of

-
- the 3rd International Workshop: Concrete Spalling due to Fire Exposure, September 25th to 27th, Paris (France).
- Noumowe A. N., Clastres P., Debicki G. and Costaz J. L., (1996), “Thermal Stresses and Water Vapor Pressure of High Performance Concrete at High Temperature”, Proceedings of the 4th International Symposium on Utilization of High-Strength/High-Performance Concrete, Paris (France).
- Picandet V., Khelidj A. and Bastian G., (2001), “Effect of axial compressive damage on gas permeability of ordinary and high-performance concrete”, Cement and Concrete Research, 31, pp. 1525-1532.
- Pistol K., Weise F., Meng B. and Schneider U., (2011), “The Mode of Action of Polypropylene Fibres in High Performance Concrete at High Temperatures”, Proceedings of the 2nd International Workshop Concrete Spalling due to Fire Exposure, E.A.B. Koenderss and F. Dehn (Eds), RILEM, Delft, October 5-7, 2011, pp. 289-296.
- Reinhard Hinkelmann, (2004), *Efficient Numerical Methods and Information –Processing Techniques for Modeling Hydro – and Environmental Systems*, Springer, Berlin (Germany), 320 pp.
- Schrefler B. A. and Pesavento F. (2004), “Multiphase flow in deforming porous material”, Computers and Geotechnics, 31, pp. 237-250.
- Shin K. Y., Kim S. B., Kim J.H., Chung M. and Jung P. S., (2002), “Thermo-Physical Properties and Transient Heat Transfer of Concrete at Elevated Temperatures”, Nuclear Engineering and Design 212, pp. 233-241.
- Tan K. H. and Yao Y., (2003), “Fire resistance of four-face heated reinforced concrete columns”, Journal of Structural Engineering - ASCE, 129 (9), pp. 1220-1229.
- Torrenti J. M., Didry O., Ollivier J. P. and Plas F., (1999), *La dégradation des bétons*, Hermés (Eds.), Paris (France).
- Tsimbrovska M., Kalifa P., Quenard D. and Da ãn, J. F., (1997) “High performance concrete at elevated temperature: permeability and microstructure”, Transactions of the 14th International Conference on Structural Mechanics in Reactor Technology, M. Livolant (Ed.), Lyon, France, pp. 475-482.
- Uysal M., (2012), “The influence of coarse aggregate type on mechanical properties of fly ash additive self-compacting concrete”, Construction and Building Materials, 37, pp.

533-540.

Wang K., Jansen D. C. and Shah S. P., (1997), "Permeability study of cracked concrete", *Cement and Concrete Research*, 27 (3), pp. 381-393.

Xing Z., Beaucour A.-L., Heber R. et al., (2011), "Influence of the nature of aggregates on the behaviour of concrete subjected to elevated temperature", *Cement and Concrete Research*, 41, pp. 392-402.

Zhang B. and Bicanic N., (2001), "Fracture energy of high performance concrete at temperatures up to 450°C", *Proceedings of the 4th International Conference on Fracture Mechanics of Concrete and Concrete Structures - FRAMCOS 4*, 28th May-1st June, 2001, Cachan (France).